THEORETICAL AND OBSERVATIONAL STUDIES OF THE CENTRAL ENGINES OF AGN

by

Ran Sivron

A thesis submitted in partial fulfillment

of the requirement for the degree

of

Doctor of Philosophy

in

Physics

MONTANA STATE UNIVERSITY

Bozeman, Montana

March 1995

APPROVAL

of a thesis submitted by

Ran Sivron

This thesis has been read by each member of the thesis committee and has been found to be satisfactory regarding content, English usage, format, citations, bibliographic style, and consistency, and is ready for submission to the College of Graduate Studies.

Date _____ Chairperson, Graduate Committee

Approved for the Major Department

Date _____ Head, Major Department

Approved for the College of Graduate Studies

Date _____ Graduate Dean

ABSTRACT

In Active Galactic Nuclei (AGN) the luminosity is so intense that the effect of radiation pressure on a particle may exceed the gravitational attraction. It was shown that when such luminosities are reached, relatively cold (not completely ionized) thermal matter clouds may form in the central engines of AGN, where most of the luminosity originates.

We show that the spectrum of emission from cold clouds embedded in hot relativistic matter is similar to the observed spectrum. We also show that within the hot relativistic matter, cold matter moves faster than the speed of sound or the Alfven speed, and shocks form. The shocks provide a mechanism by which a localized perturbation can propagate throughout the central engine. The shocked matter can emit the observed luminosity, and can explain the flux and spectral variability. It may also provide an efficient mechanism for the outward transfer of angular momentum and the outward flow of winds.

With observations from X-ray satellites, emission features from the cold and hot matter may be revealed. Our analysis of X-ray data from the Seyfert 1 galaxy MCG -6-30-15 over five years using detectors on the Ginga and Rosat satellites, revealed some interesting variable features. A source with hot matter emits non-thermal radiation which is Compton reflected from cold matter and then absorbed by warm (partially ionized) absorbing matter in the first model, which can be fit to the data if both the cold and warm absorbers are near the central engine. An alternative model in which the emission from the hot matter is partially covered by very warm matter (in which all elements except Iron are mostly ionized) is also successful. In this model the cold and warm matter may be at distances of up to 100 times the size of the central engine, well within the region where broad optical lines are produced. The flux variability is more naturally explained by the second model. Our results support the existence of cold matter in, or near, the central engine of MCG -6-30-15. Cold matter in the central engine, and evidence of the effects of shocks, is probably forthcoming with future X-ray satellites.

STATEMENT OF PERMISSION TO USE

In presenting this thesis in partial fulfillment of the requirements for a doctoral degree at Montana State University, I agree that the Library shall make it available to borrowers under rules of the Library. I further agree that copying of this thesis is allowable only for scholarly purposes, consistent with "fair use" as prescribed in the U.S. Copyright Law. Requests for extensive copying or reproduction of this thesis should be referred to University Microfilms International, 300 North Zeeb Road, Ann Arbor, Michigan 48106, to whom I have granted "the exclusive right to reproduce and distribute my dissertation in and from microform, analog with the non-exclusive right to reproduce and distribute my abstract in any format in whole or in part."

Signature

Date

ACKNOWLEDGMENTS

Many good friends helped me in completing this thesis. I would firstly like to thank my advisor, professor Sachiko Tsuruta, for numerous discussions, corrections, suggestions and support throughout the course of my graduate studies. Many thanks to my mentors in matters of data analysis, Professor Hideyo Kunieda from Nagoya University, and Dr. Karen M. Leighly, currently with the RIKEN astrophysics group in Japan. I would also like to thank Professor J. Carlsten and Professor W. Hiscock for the careful review of this thesis.

Next I would like to thank Nava Rabiner Sivron, for all the love and care, the tough — but always helpful — criticism, and, of course, for our light, Carmel. I would also like to thank my good friends that helped me by being my think tank, 'computer bugs doctors' and English editors, Dr. Adli Saleh, Mr. Tsunefumi Tanaka, Mr. Michael J. Kellen, Mrs. Letao Qin, Dr. Todd Grigereit, Dr. Greg Mendell, Dr. David Caditz and Dr. Bennet Link.

TABLE OF CONTENTS

TABLE OF CONTENTS — Continued

TABLE OF CONTENTS — Continued

LIST OF TABLES

Table Page

LIST OF FIGURES

Figure Page

LIST OF FIGURES — Continued

LIST OF FIGURES — Continued

Chapter 1

INTRODUCTION

In this chapter we introduce the current theories and observations of the central engines of AGN. In the first section partially successful models of the central engines of AGN are presented. The second section is devoted to observations of AGN in the X-ray waveband, in which most of the radiation from the central engines is probably emitted. In the third section some of the problems in theoretically modeling the central engines of AGN are presented, possible solutions suggested in this thesis are outlined and our analysis of X-ray data from an AGN is discussed.

1.1 INTRODUCTION TO THEORY OF AGN

1.1.1 What are AGN?

Active galactic nuclei (AGN), which are the extraordinarily luminous centers of some galaxies, are among the most enigmatic phenomena in astrophysics. AGN may

be as small as the solar system, but have energy outputs which, in some cases, rival the luminosity of the entire host galaxy. Approximately 10% of all galaxies are AGN, and at least 50% of galaxies show some evidence of activity in their nucleus. As of this date there is no one cohesive explanation to the source of this phenomenon that can be directly corroborated by observations. AGN are therefore characterized by observations.

In table 1 some of the observable properties of AGN are presented. Only properties related to the galactic nucleus are included. Other basic properties can be found in Woltjer 1990, Netzer 1990, Mushotzky, Done and Pounds 1993 and references therein. A partial list of AGN and host galaxies types is presented in the first two columns: Seyferts are optically resolved spiral galaxies with an AGN. Seyferts of type 1 have both broad and narrow emission lines in the infra-red (IR) - ultraviolet (UV) wavebands, and Seyfert 2s have only narrow emission lines. Seyferts comprise about 5% of all galaxies. AGN which could not be optically resolved when they were first observed are usually referred to as quasars. (In the past few years some quasars were optically resolved and shown to be AGN.) The radio quiet quasars are called quasi-stellar objects (QSO). In optically resolved elliptical galaxies AGN are usually radio galaxies and BL LAC objects (whose spectrum resembles the spectrum

of strong radio galaxies, but lack emission lines and are highly variable). The radio loud quasars are quasi stellar radio sources (QSR) and quasars which exhibit strong optical variability are called optically violent variables (OVV, mostly a subgroup of QSR). Increased activity in the nuclear region may also be in the form of increased rate of star formation (in star burst galaxies), strong emission lines (in LINERS and nuclear H II regions) and increased IR emission (strong IRAS galaxies).

AGN morphology is based primarily on luminosity and spectrum, although the property which distinguishes AGN from most other astrophysical objects is their high luminosity per volume. We therefore included in the next four columns of table 1 some information on observed properties which are directly related to the luminosity and size. The estimated total luminosity in column 3, L_{tot}, includes emission in all wavelengths, whereas in column 4 we only include L_X, the emission in the dominant x-ray waveband. In column 5 the estimated doubling time scale Δt (the minimum time the X-ray flux takes to double in magnitude) is presented. Using columns 4 and 5 the compactness of the source can be defined as $l = L_X \sigma_T / (\Delta t m_e c^4)$ (Guilbert Fabian and Rees 1983), where σ_T is the Thompson cross section, m_e is the electron mass and $R = c\Delta t$ is usually referred to as the size of the central engine (see sections §1.3 for a more precise physical definition of the central engine). The compactness

parameter is only appropriate for the first three categories of AGN. In Seyfert 2s the nucleus is most probably obscured, and the compactness parameter is meaningless.

Table 1. AGN: Observations That Can be Related to Central Engines

AGN type	Host Galaxy[a]	L_{tot}[b]	L_X[c]	Δt[d]	l[e]
Seyfert 1s	spiral	10^{42-45}	10^{41-44}	10^{3-5}	$10^{-2} - 10^{3}$
Seyfert 2s	spiral	10^{42-45}	10^{40-42}	$\sim 10^{7}$[f]	?
QSO	spiral(?)	10^{44-47}	10^{43-46}	10^{5-7}	$10^{-2} - 10^{3}$
Radio	elliptical	$\sim 10^{42-45}$[g]	[g]	10^{4-7}?	?
Strong Radio	elliptical	$\sim 10^{42-44}$[g]	[g]	?	?
QSR	elliptical(?)	$\sim 10^{43-47}$[g]	[g]	?	?
BL Lac	elliptical	[h]	[h]	$\sim 10^{4}$	?
OVV	all?	[h]	[h]	10^{4}	?
LINER	spiral	[i]	[i]	?	?
HII regions	spiral[i]	[i]	?	?	
IRAS		$\sim 10^{45}$[j]	?	?	?

[a]QSO and QSR are mostly unresolved.

[b]in erg sec^{-1}, estimated for the galactic nuclei.

[c]in erg sec^{-1} in the $2 - 10$Kev range, estimated for the galactic nuclei.

[d]in seconds. Upper limit is an estimate.

[e]Compactness of central engine, lower limit: $l \sim L_x \sigma_T / R m_e c^3$.

[f]Some evidence for variability between x-ray observations

[g]Most of the observed flux is not from the central engine

[h]Most of the observed flux is probably from an observer oriented jet.

[i]Galactic nuclei emission can only be estimated in LINER and HII regions.

[j]Most emission in IR.

1.1.2 The Importance of AGN

Better understanding of AGN may help answer a number of questions. Among them:

1. Galactic morphology: AGN may help us understand how galaxies form and evolve. A large fraction of all galaxies have at least some AGN features, which implies that most galaxies may have had AGN in their centers at some point in their history (Blandford 1990, and references therein). Emission from highly red shifted quasars imply the existence of nuclear galactic activity at an epoch in which galaxies were not even supposed to have formed, according to many scenarios of galaxy formation. Understanding AGN will therefore help in understanding galactic evolution.

2. Cosmology: If we can understand AGN, quasars may become the perfect 'standard candles', which can be used to determine the geometry of the universe . Using a standard candle of known luminosity L_Q at a 'luminosity distance' $d_L = (L_Q/4\pi F)^{1/2}$, the cosmological parameters can be determined by observations using $H_0 d_L = z + 0.5(1 - q_0)z^2 + ...$, the approximate solution of Einstein equations for an expanding matter dominated universe. Here F and z are the observed flux and redshift, respectively. The Hubble constant H_0 and deceleration parameter q_0 may be found by using quasars, the highest redshift objects in the universe. These

parameters, if determined, may reveal the geometry of the universe (Woltjer 1990, Schutz 1985).

3. High energy physics: AGN may serve as high energy labs with which one can enhance our understanding of high energy phenomena. There are reasons to believe that very efficient particle acceleration mechanisms are present in AGN centers, and that plasmas with temperatures unaccessible in labs are present near their centers (Blandford 1990, Blandford and Eichler 1987).

4. General relativity: Understanding AGN may allow us a look into the very nature of the general theory of relativity. Some effects that may be observed in the future are the Lense-Thirring precession, energy extracted from a rotating black hole or, possibly, gravitational radiation from binary black holes in the central engine of an AGN (Blandford 1990 and references therein). These effects, when observed, will consolidate our understanding of general relativity.

5. The large scale structure of the universe: The spectrum and isotropy of the X-ray background are probably the signature of a period less than a billion years after the big bang. In that period more galaxies had active nuclei. It was shown that AGN may account for most of the X-ray background. An early evidence of the large scale structure may therefore be available (Fabian and Barcons 1992, and references

therein).

In order to advance towards a solution to these questions better understanding of AGN must be developed. In particular, emission of light and particles from the vicinity of the AGN center must be understood. These processes can only be explained in the context of a model for the central driving force of an AGN, the central engine.

1.1.3 Possible Candidates for the Central Engines of AGN

It is now generally accepted that super massive compact objects lurk at the centers of AGN (see Blandford 1990, appendix 1). Gravitational potential energy of matter which falls onto these objects is released in the form of radiation. Although the gravitational behavior of the massive objects is yet unknown, and the mechanisms by which these objects generate the incredible observed phenomena are not yet fully explained, the matter accreting super massive compact object model is the most successful in describing the phenomena.

Traditional candidates for the AGN central engines, such as dense clusters of normal luminous stars and clusters of neutron stars are probably rejected by the recent observations with the Hubble Space Telescope (HST) of a single central super massive object (see Ford et al. 1994). The Chandrasekar limit on masses of stars makes it impossible to construct a super massive compact object made of baryonic

matter. Another alternative model is the star-burst model (Terlevich et al. 1992, and references therein), in which the energy is generated by violent star formation activity in the innermost regions of AGN. Although the spectra of AGN may be explained in this manner the variability is almost impossible to explain (Green 1993, and references therein). Its also hard to reconcile star-burst models with HST observations.

The compact objects are assumed to be super massive black holes (SMBH) in the so called 'best bet' model for AGN (Salpeter 1964, Lynden-Bell 1969, Rees 1984, Blandford 1990). We hereafter refer to the central compact objects as SMBH, as is often done in the professional literature. SMBH are the central objects in the models described in the following sections. (But note the quote from Blandford 1990: "...various observational discoveries are increasingly hard to interpret in terms of alternative models... however... the evidence [for black holes] is weaker than for stellar mass black holes in X-ray binaries...)

Black holes are vacuum solutions of Einstein equations with an event horizon, from which light and particle can not escape (Wald 1984). Schwarzschild and Kerr family of solutions span all possible solutions for vacuum stationary axisymmetric spacetimes with a regular event horizon (Misner, Thorne and Wheeler 1972, Robinson 1975, Mazur 1982). The spherically symmetric Schwarzschild solution is a special case of

the axisymmetric Kerr solution. A positive change in the mass of the central compact object, $\Delta M > 0$, is required in both of the Schwarzschild and Kerr solutions, if the efficiency of the accretion process is less than 100 %.

Black holes are more efficient in conversion of the mass to energy than other astrophysical processes. For example, nuclear fusion of hydrogen to helium can convert up to 0.7% of the rest mass to energy. Near Kerr SMBH up to 40% of the rest mass of the gas accreted onto the black hole can be converted into energy.

The release of gravitational energy from matter that falls onto the SMBH is via viscous processes in either accretion disks or semi-spherically accreted matter (see Frank, King and Raine 1992; Guilbert and Rees 1987; chapters §2 and §5 of this thesis). In accretion onto black holes most of the gravitational energy is released within the inner $10R_g$ where $R_g = GM/c^2$ and M is the mass of the SMBH. This can easily be seen if the Newtonian potential energy becomes kinetic energy which is radiated away, such that $GMm_H/(6R_g) - GMm_H/(10R_g) \sim 0.06m_Hc^2$, or 6% of the rest mass is converted into energy, where m_H is the mass of hydrogen. The inner boundary is chosen to be the last stable orbit in a Schwarzschild geometry. Accurate calculations of the total energy which can be radiated by an accreted particle yield a similar number. The efficiency of the accretion process is not only higher than that

of hydrogen fusion, for example, but is also more stable than fusion when limited to a size $10R_g$. We hereafter refer to the inner $10R_g$ as the 'the central engine' as is often done in the professional literature. Accretion processes are assumed to be the main source of the energy emitted from the central engine.

The limited supply of mass to be accreted onto the SMBH in the center of AGN poses some problems for the best bet model. For a thorough discussion of this problem the reader is referred to Rees 1990.

Direct emission from the central engine may give us evidence of a SMBH. However, the spatial resolution of present day telescopes can not tell us whether most of the radiation originates in the central engine or elsewhere, even in the nearest AGN. Redshifted emission lines may indicate emission from the vicinity of a SMBH, if observed. Variability may be observed which could be explained by gravitational lensing modification of emission from matter that follows geodesics in the central engine (Rauch and Blandford 1994).

A combination of observations of the spectrum, flux variability and spectral variability can be used for reconstruction of the possible geometrical configuration of the central engine. The results of such observations are described in the next three sections. A way to distinguish the central engine radiation from competing emissions

regions may be found in the near future.

1.1.4 Spectra of Emission from the Central Engines of AGN

The overall continuum spectra of most AGN can be characterized as power-law with bumps super-imposed in the IR and UV, or extreme UV (EUV) and X-ray wavebands. (The IR bump probably does not originate in the central engines of AGN. See Blandford 1990.) Emission and absorption features are also present at photon energies of up to $\sim$ 10keV.

In figure 1-1 we show the spectrum in wavebands from radio to γ rays of the quasar 3C273. The abscissa has units of ν and the ordinate has units of $\log \nu F_\nu$, where ν is the photon frequency and F_ν is the flux per frequency. The reason for this choice of coordinates is that for a power-law spectrum, of the form $F_\nu \propto \nu^{-\Gamma}$, the integrated flux between two frequencies, ν_1 and ν_2, is $F = C \log(\nu_2/\nu_1)$ when $\Gamma = 1$, where C is a constant. The total emission in each photon frequency decade is therefore the same, and a 'flat' curve appears on a graph of the above format. It is evident that the AGN flux in figure 1-1 has an almost flat spectrum. Black body stellar emission of a galaxy appears as a reference for comparison.

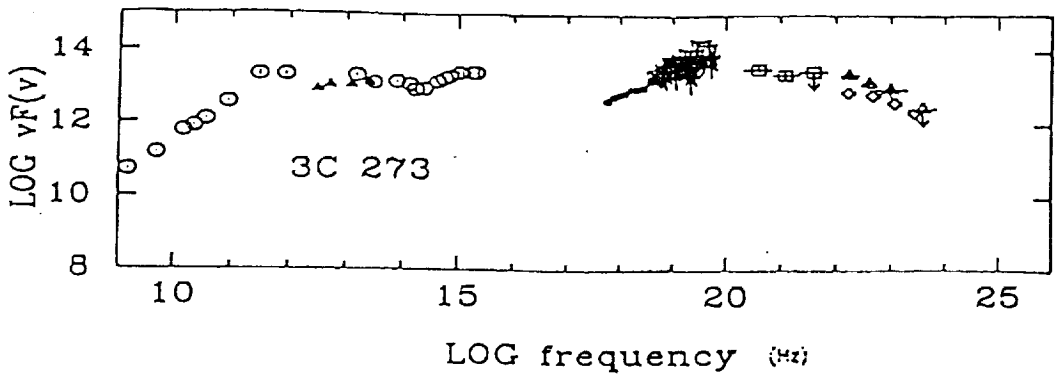

Figure 1.1: The spectrum quasar 3C273. AGN emit similar integrated power in the IR γ-ray wavebands (see text). (Adapted from Green 1993.)

If a SMBH is at the center of the AGN then most of the radiation originates in the central engine, as demonstrated in section 3 and chapter 2. The radiative processes responsible for the radiation that emerges from the central engine probably include synchrotron radiation, Compton scattering, radiative reprocessing in pair plasmas, and may includes atomic radiative transitions and black body emission.

Synchrotron radiation emitted from relativistic electrons in magnetic fields should affect the spectrum if the synchrotron cooling time is shorter than the typical accretion time. Synchrotron emission, which should result in radio polarization, was proven to be important in most AGN by measurements of polarization. Measurements of magnetic fields in galactic centers yield values which require that synchrotron radiation be an important radiation mechanism on all scales. These magnetic fields which probably originate in stars which are being disrupted by the SMBH are increased as the accreting plasma becomes denser. Near the central engine the magnetic fields are strong enough to result in cooling time scales which are much shorter than the accretion time scales.

Synchrotron radiation in astrophysics usually result in an almost flat power law spectrum, similar to the underlying spectrum of most AGN. The synchrotron radiation in astrophysics usually comes from a power-law distribution of electrons veloci-

ties, which may result from acceleration mechanisms such as the Fermi-shock process in shocks. The resultant spectrum is an almost flat power-law spectrum, which almost with a low frequency cutoff due to synchrotron self absorption. This self absorption may be associated with the radio-quietness of some compact AGN.

The effects of Compton scattering on the spectrum are noticeable when the cooling time of photons of energies comparable to $m_e c^2$ is shorter than the time in which a photon is crossing the emission region, $t_x = R/c$. The spectrum may also be affected by Compton scattering of low energy photons by relativistic electrons when the time scale for that process is shorter than t_x. Compton heating and cooling are important if the overall Thompson (or Klein Nishina) optical depth is large, which happens when the source is sufficiently compact ($l > 1$, see table 1). Compton cooling, usually referred to as 'reflection', is important if the Thompson optical depth of cold matter in the photon's path is larger than 1. The result of Compton cooling on a power-law spectrum is a decrease of the γ-ray photon flux and an increase in hard X-ray photon flux. Compton processes may, therefore, be responsible for the high energy cutoff and hard X-ray bump in the spectra of radio quiet AGN (Mushotzky, Done and Pounds 1993).

Pair processes affect the spectrum when the compactness parameter l is larger

than $\sim$ 10 (Lightman 1982, Svennson 1987). When this condition is met pair creation usually exceeds annihilation. Pairs lose most of their energy through Coulombic collisions. In some cases pair cascades, in which the relativistic pairs collide with the ubiquitous photons creating more pairs with less energy in the process and depleting the radiation field. If pair annihilation becomes important the 511keV pair annihilation line may be present in the spectrum. The effects of pairs on the spectrum are a decrease of the (negative) spectral slope in the UV waveband due to loss of soft photons, and an increase in the hard X-ray - *gamma*-ray wavebands, due to the loss of pair producing hard photons. Pair production is traditionally calculated in the presence of relativistic electrons and UV photons of relative compactness l_h for the electrons and l_s for the photons. It should be noted that although pair production can happen without synchrotron or Compton processes, an input power-law spectrum is generally assumed for the electrons, mainly because most processes that produce enough highly relativistic electrons also result in a power-law photon spectrum.

The atomic radiative free-free, bound-free, bound-bound and black body processes usually take place in 'cold'(not completely ionized) plasmas. The features superimposed on the continuum spectrum as a result are lines, edges and bumps in the IR through medium X-ray wavebands. The feature with highest photon energy is the

iron line-edge system near 7keV, which may have an absorption effect at up to 10keV. (Absorption and emission features in the optical and UV regime are believed to be coming from regions which are far beyond the central engine. See Netzer 1990 and section 1.5.)

Matter in local thermal equilibrium (LTE) may be present in the central engine of AGN, and may be responsible for the UV bump superimposed on the flat spectrum. This UV bump is thought to be black body emission from optically thick LTE plasmas with different temperatures.

We shall limit our discussion to radio quiet AGN throughout the rest of the chapter. In radio quiet AGN most of the radiation is emitted in the EUV – X-ray wavebands, and the X-ray emission is believed to originate in the central engine (see the following section). Radio loud quasars may emit significant amounts of radiation from their jets due to relativistic beaming effects (see appendix 1). As a result it is very hard to distinguish central engine emission from jet emission. x

1.1.5 Variability of Emission from the Central Engines of AGN

More than 50% of radio quiet AGN exhibit large amplitude flux variability in the X-ray waveband. Spectral variability is also present in many of these AGN

(Mushotzky, Done and Pounds 1993). Long term variability (years) is present in most sources, whereas at least half of the sources exhibit short term large amplitude variability (Green 1993, McHardy 1988).

The flux variability (generally referred to as the light curve) is shown in figure 1-2 for three AGN. In the upper panel (1-2a) the light curve of NGC 4051 is shown. In the middle panel (1-2b) the light curve of NGC 5506. The light curve of MCG -6-30-15, a Seyfert galaxy which is extensively discussed in chapter 6, is shown in the lower panel (1-2c). It is evident that, in the first and last cases, the total flux doubles on timescales of thousands of seconds. This change in flux is believed to originate in the central engine.

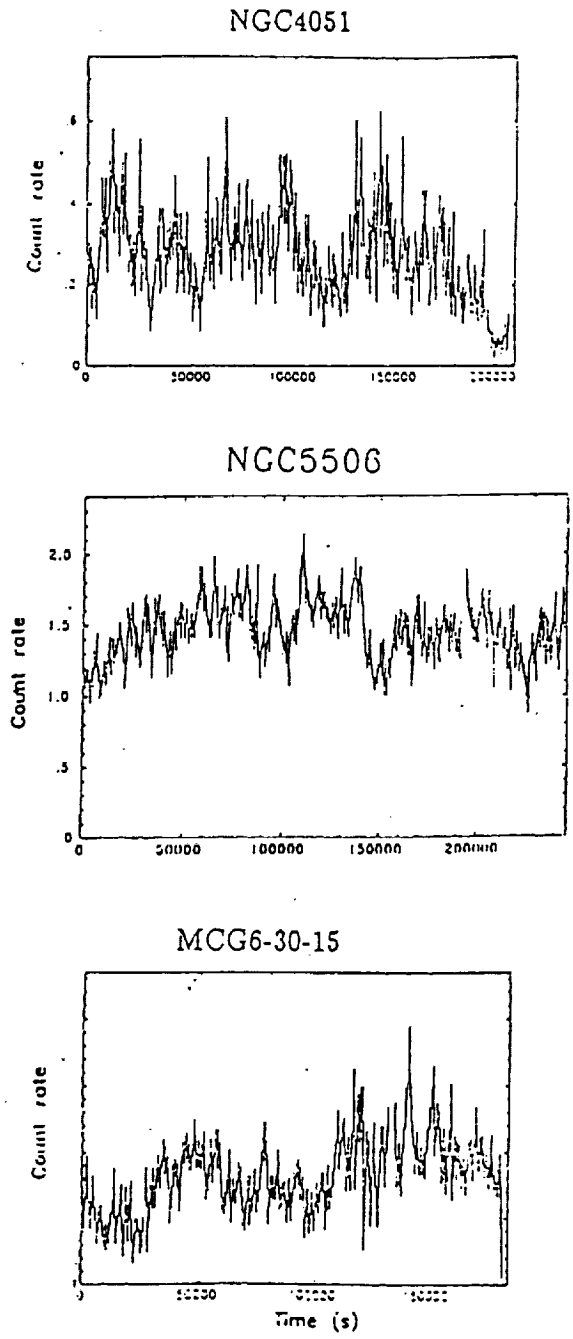

Figure 1.2: Typical flux for two types of variability: a. NGC 4051 exhibits large amplitude 'shot-noise' time variability ; b. NGC 5506 exhibits an almost 'chaotic' time variability. c. MCG -6-30-15 has time variability which is in between a. and b. (see text). Most AGN have time variability which is similar to a. or c. (Adapted from McHardy 1988.)

The size of the emitting region is usually assumed to be smaller than $R_e = \Delta tc$, where Δt is time in which the source is observed to double in flux. For incoherent radiation this condition is necessitated by causality. Events in a region of size R_e cannot be be correlated by perturbations that move faster than light. Since most of the energy is emitted in the variable part of the spectrum R_e is the maximum possible size of the central engine. Since the shortest observed doubling timescale goes to hours in Seyfert 1 galaxies (see table 1) the emission region can be assumed to be of order 10^{13}cm in radius. The emission from this region is larger than $\sim 10^{42}$erg sec^{-1}. As a result models that try to explain the light curve need to account for the enormous production of energy per volume, which is quantified by the compactness parameter in table 1.

The Fourier transform of the light curves $P = \sqrt{1/2\pi} \int_0^\infty exp(i\omega t) f(t) dt$ (usually referred to as the power spectrum) can be used to categorize the different types of variabilities. In the upper panel of figure 1-3 the power spectrum of NGC 4051 is shown, the power spectrum of NGC 5506 is shown in the middle panel and the power spectrum of MCG -6-30-15 is shown in the lower panel. Unlike many sources inside our galaxy, there are no periodic components, which would appear as prominent spikes, in the power spectrum of AGN. The logarithm of the Fourier transform of a light curve

with random flux level (white noise) can be fit by a constant. The Fourier transform of flux from regions of random sizes and random flux levels is usually referred to as a 'random shot noise'. In this case the power spectrum $\log L(f) \propto \log(-1/(f^2))$, where f is the frequency of variability, and the slope is -2. The flux of NGC 4051 is nearly a random shot noise. An almost chaotic intermediate $\log L(f) \propto \log(-1/(f))$ power spectrum slope fits the Fourier transform of the light curve of NGC 5506. MCG -6-30-15 has an intermediate power spectrum slope of ~ -1.4.

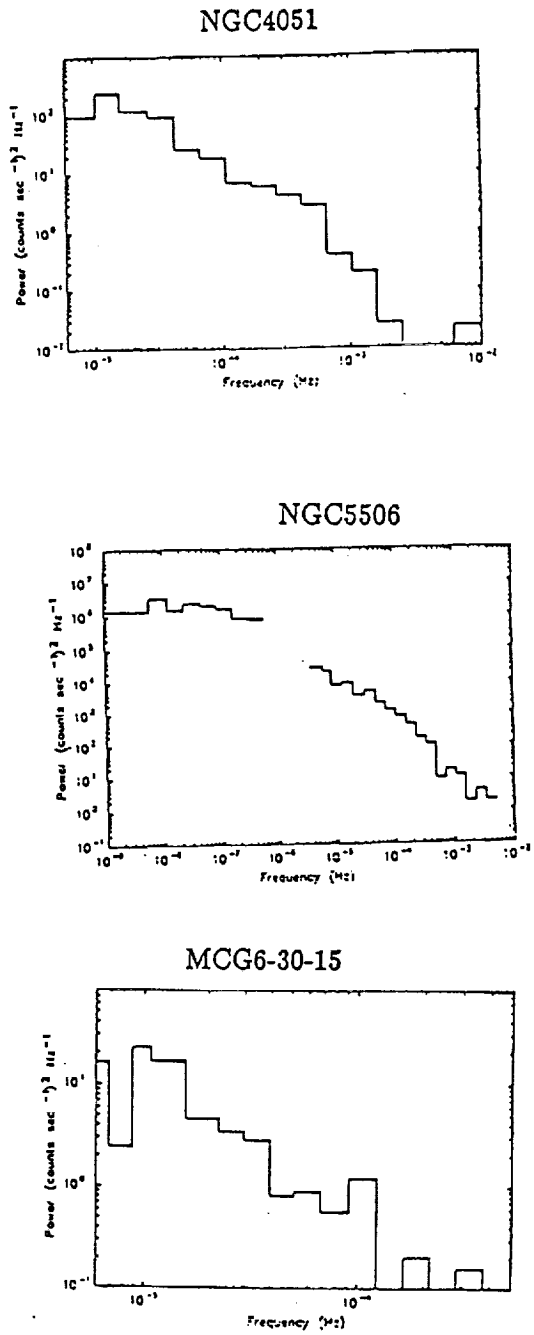

Figure 1.3: The Power spectrum of the AGN in figure 1-2: a. NGC 4051 b. NGC 5506 c. MCG -6-30-15 (adapted from McHardy 1988)

Some models of the variability assume white noise which is filtered by matter in the line of sight. For example, when variable white noise flux is incident on matter with moderate optical depth the higher frequencies are filtered out. Spherical extended regions of size R_e yield random shot noise from the original flat power spectrum (Sunyaev and Titarchuk 1980). This spectrum may be modified if pairs are present, as is expected in high luminosity to size ratio sources (Done and Fabian 1989, Lightman and Zdziarski 1987). Chaotic processes may also explain the observed power spectrum (Vio et al 1991), but no physical mechanism is yet known that may explain such processes.

1.1.6 Geometrical Models of the Central Engines of AGN

The most successful models of AGN include an accretion disk which channels accreted matter from the surrounding gas and stars onto a central super massive compact object in the central engine. In order to understand the observational success of this model one must look at models of the 'outer regions' (regions outside the central engine) of AGN.

In figure 1-4 we see a simplistic, schematic description of the current geometrical model of the outer regions of radio quiet AGN.

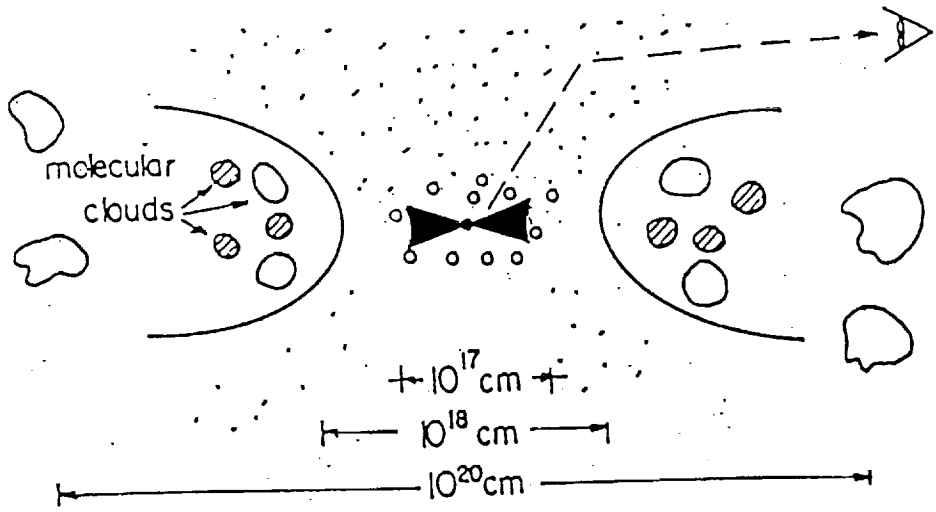

Figure 1.4: This picture of AGN has an axial symmetry about the vertical center of the page. Radio quiet AGN are presumed to have molecular clouds in a torus configuration, electron scattering region, broad line region (the small open circles) and an inner accretion disk (the X shape in the middle). The observed emission therefore depends on the orientation of the observer with respect to the AGN axis. (Adapted from Mushotzky, Done and Fabian 1993.)

Our current picture of the outer regions of radio quiet AGN is: In the outermost regions lies the source of matter to be accreted onto the SMBH. This matter may originate in a rich stellar clusters, the inter stellar medium (ISM), or may be the result of cooling flows in clusters of galaxies (Blandford 1990, Rees 1990). We hereafter assume this matter to contain the usual cosmic abundance. Strong narrow lines are emitted by an unknown geometrical configuration of material with atomic number density $10^5 - 10^7 \mathrm{cm}^{-3}$, slightly more dense than the ISM, at distances of order 1 Kpc from the central engine. This material is usually referred to as the narrow line region (NLR, see Netzer 1990). A little closer to the central engine molecular clouds form an axisymmetric 'molecular torus'. The molecular torus may be responsible for the obscuring of parts of the more energetic parts of the spectrum, and is probably responsible for most IR emission. Closer to the center is the Broad Line Region (BLR), the geometry of which is uncertain. The broad line region clouds are the open circles near the center of figure 1-4. From the observed width of the optical lines we know that the BLR matter is moving fast. Other observations reveal the filling factor is small, and the number density of matter is $10^8 - 10^{10} \mathrm{cm}^{-3}$ in the BLR (Netzer 1990). Evidences for a super massive compact object and a superluminous central engine are mostly found from observations of NLR and BLR emission lines

(Netzer 1990).

Closer to the central engine a geometrically thin accretion disk, which is optically thick, is usually considered to be present. In figure 1-4 the disk is represented by the central dark bow-tie shaped region. Matter in this disk is accreted onto the SMBH. This disk is generally considered to emit a significant portion of the total luminosity emitted by AGN in the UV band (the so called 'UV bump'), and may also be responsible for the ionization of clouds in the BLR. The disk configuration is most efficient in the outwards transfer of angular momentum, which allows for high accretion rates. Angular momentum is viscously transferred from accreted matter to outflowing particles and radiation.

Since the model for the outer regions cannot explain the X-ray emission and variability a different, more elaborate, model is needed for the central engine. The model of the central engine must take the accretion disk into account.

Calculations show that the thin accretion disk is thermally unstable near the central engine because the heating due to viscosity exceeds the radiative cooling (see Lightman and Eardley 1974, Thorne and Price 1975). As a result, a geometrically thick disk which can be optically thick (if supported by radiation pressure) or optically thin (if supported by ion pressure in a two-temperature plasma, see Shapiro, Lightman

and Eardley 1976; Rees et al. 1982) may form. The central engines of AGN are considered to be the inner part of such disks. The electron temperatures of these disks, which may exceed 10^9K, and the magnetic fields which are of order 10^3 gauss, can account for the synchrotron and Compton processes that can produce the observed spectrum. When pair-cooling is important the central regions of the geometrically thick disk may collapse into an assembly of clouds, an annulus, or thin disk. The effect of pair plasmas on optically thin and optically thick disks is discussed in several papers (Begelman Sikura and Rees 1987, Tritz and Tsuruta 1989, Kusunose and Takahara 1989).

In figure 1-5 we show the schematic description of the central engine, which assumes a disk configuration. Spectra for the disk corona model were calculated by Lightman and White 1989, George and Fabian 1990, Tritz 1990, Tsuruta and Kellen 1994.

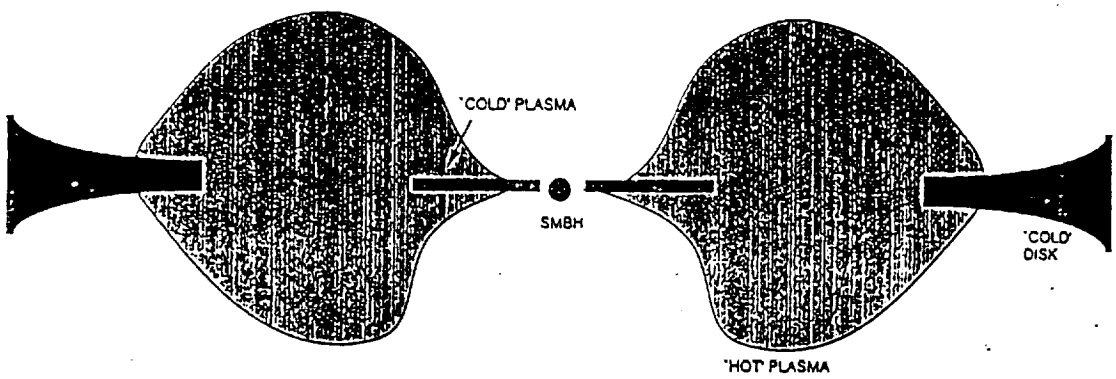

Figure 1.5: The disk model for the central engine of AGN includes an outer cold disk which flares up to form a thick torus of very hot plasmas (10^9-10^{12}K) in its inner regions, and collapses back to a thin disk configuration near the SMBH.

An alternative model of the central engine is the 'disk corona' model (Svennson and Zdziarski 1994). In this model the disk is not disrupted because of pressure from the corona in which most of the radiation is produced. The radiation in this model is mainly through Comptonization of the UV disk emission.

Many models attempt to reproduce the various AGN light curves while assuming the existence of an accretion disk in the central engine. One model which suggests that the magnetic field reconnection at the surface of an accretion disk may result in an acceptable power spectrum (Pudritz and Fahlman 1982, De Vries and Kuipers 1989, see also remarks in chapter §7). Another disk model include randomly appearing uniformly distributed hot spots, which are related to magnetic flux tubes and may appear on the surface of Keplerian accretion disks with different apparent intensities due to the Doppler effect (Abramowicz 1991).

An alternative model for the central engine which does not include an accretion disk is presented in section 3 of this chapter.

1.2 INTRODUCTION TO X-RAY OBSERVATIONS OF AGN

1.2.1 Why X-rays?

The central engines of radio quiet AGN are most readily observed in the X-ray

waveband. Radio quiet AGN are observed throughout the electromagnetic spectrum, but most of their energy is emitted in the UV, X-ray and γ-ray wavebands. Recent observations by the OSSE and COMPTEL instruments on board the Compton gamma ray observation satellite have shown a high energy end cutoff in the hard X-ray - soft γ wavebands of most radio quiet AGN, above a few hundred keV (Ghiselini et al. 1994 and references therein). The IR observations of the same sources reveal a cutoff at 10^{-3}eV. The dominant parts of the spectrum are therefore in the UV - soft γ-ray wavebands. Unluckily the EUV part of the spectrum is heavily obscured by ISM in our galaxy, thus making observations extremely difficult. The X-ray waveband is therefore the most dominant part of the spectrum that can be observed with present technology.

Evidence that most of the EUV and X-ray emission originate in the central engine mount. Studies of the BLR show that an internal 'hard' (photon energy higher than few tens eV) source is irradiating the BLR matter. It is generally accepted that in radio quiet AGN there is no strong 'contamination' of the X-ray spectrum from the central engine with emission from strong relativistic jets (although faint small scale jets are observed in Seyfert galaxies, Wilson 1985, Mushotzky, Done and pounds 1993). The IR spectrum of these sources, which is generally thought to originate

in dust from the molecular torus, is not variable (Done et al. 1991). The optical continuum, which may originate in the thin accretion disk, cannot dominate because it covers less than a decade of frequencies (see figure 1-1).

The best evidence that most of the X-ray flux originate in the central engine comes from an argument about large amplitude flux variability. Timing studies show that the size of the X-ray emitting region is much smaller than the BLR region (see sections 1.4, 1.5). Whereas in other wavebands the variability of radio quiet AGN, if existing, is on timescales of years and with very small amplitude (see Mushotzky Done and Pounds 1993, for example), the large amplitude variability of X-ray emission is rapid (doubling the flux in hours. see for example section 1-4 figure 1-2). X-rays are, therefore, the window through which we are able to collect most data about the central engine.

In the observational part of this thesis we concentrate our attention on Seyfert 1s nuclei, a large subgroup of radio quiet AGN. Seyfert 1s show significant variability amplitude over a short time scale in the X-ray waveband and may therefore provide us with more information than QSO. Since the time scale of variability of QSO is years long term observations from X-ray satellites are not practical. Seyfert 2 galaxies are excluded because there is evidence of large absorption columns in the line of sight

(probably due to the molecular torus, see Antonucci 1993). These large absorption columns are probably responsible for the reprocessing of the original central engine radiation.

1.2.2 Large Area Counters, X-ray Telescopes and Other Technologies

X-rays cannot be observed through Earth's atmosphere. Balloons, rockets and satellites are therefore used in order to go above the atmosphere. Observing from very high altitudes may not be advantageous for several reasons. One reason is the increased cost of the observation. Another is that Earth's upper atmosphere actually operates as a shield against energetic cosmic rays which may excite nuclei and high Z atoms in the satellite, resulting in internal background due to atomic and nuclear decay. Most X-ray missions are therefore launched into the so called low-Earth orbit, a few hundred kilometers above Earth's surface.

Very few X-ray photons from extra galactic sources are collected by the detectors on board X-ray satellites. The internal background may therefore be much larger than the signal, requiring a sophisticated array of photon rejection techniques. The X-ray background radiation, which is poorly understood, should also be rejected when pointed observations are performed. Large area counters, which collect the largest

number of photons, are the most sensitive to these types of noise.

In X-ray telescopes, on the other hand, the detector volume is small, and the internal background is therefore subdued. Photon statistics, on the other hand, are very poor in these detectors, and the sensitivity to flux variability is limited.

1.3 AGN IN THIS THESIS

1.3.1 Theoretical Treatment of AGN in This Thesis

In the first part of the thesis we explicitly calculate the effects on the spectrum of the 'two component cloud model' of the central engine, which under certain conditions is a viable alternative to the disk and disk corona models. The two component cloud model was first suggested by Guilbert and Rees (1988). Guilbert and Rees and Celotti Fabian and Rees (1992) noted that moderate compactness values may result in high optical depth $\tau = n\sigma R$, where n is the number density of the accreted matter, σ is its cross section for absorption and R is the size of the central engine. Density perturbations thus grow as a result of radiation or magnetic pressures. When the density is increased cooling in the dense regions is increased. The cooler matter has even higher optical depth, and the added radiative (or magnetic) pressure increases the density even further. The process terminates when the denser regions become

thermalized and self pressurized. These 'cold' denser regions, which may be in the form of plasma sheets and filaments, are referred to as 'clouds' in this thesis. Typical temperatures are $10^9 - 10^{12}$K for the hot component and $10^5 - 10^7$K for the cold component clouds. It is not at all clear that these clouds can form an accretion disk. Since the clouds are embedded in a hot plasma this model is referred to as the two component cloud model, or 'the cloud model', in this thesis.

In figure 1-6 the general picture of the cloud model is presented.

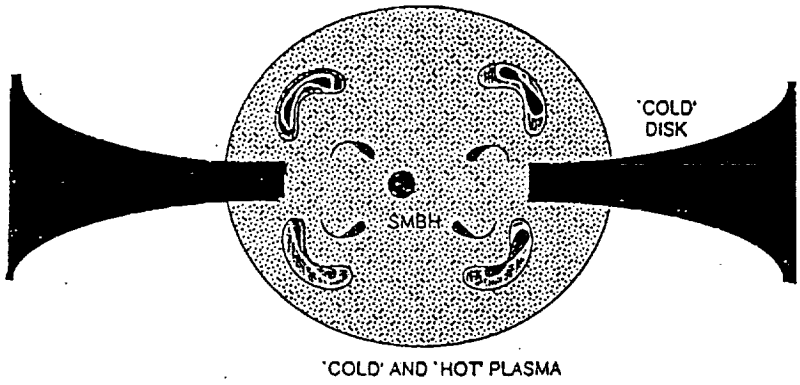

Figure 1.6: The cloud model (or: 'two component cloud model') for the central engine may include an outer cold disk which flares up to form a thick torus with two phases: very hot plasmas (10^9-10^{12}K) in one phase, and a colder dense plasmas (10^5-10^7K) in the other phase.

The clouds may manifest themselves in emission, absorption and reprocessing spectral features which characterize cold matter. Recently such features were discovered in X-ray observations of AGN (e.g. Mushotzky, Done and Pounds 1993). These clouds may also be responsible for the UV bump which is frequently observed in the spectrum.

In chapter 2 we present an equation of state for the cloud model. The radiative transfer equations for clouds in chapter 3, which utilize the equation of state, results in spectra which are shown to generally fit the observed spectra of radio quiet AGN. In chapter 3 we also describe the conditions under which the two component cloud model is viable.

In the second part of the thesis we present an alternative model for the variability of the central engine. A problem with the disk and disk-corona models is the a posteriori nature of the explanation of variability. We develop an alternative, self consistent, model for the variability of the central engine in chapter 4. We investigate the dynamical properties of the central engine, and we also consider the possibility of shocks. We show that shocks, which readily form in the central engine, may be responsible for the observed light curve and spectral variability. Shocks are also considered to be efficient in transferring angular momentum, accelerating particles

and the creation of the cold and hot components of the cloud model. The importance of shocks in the calculations of the stability of optically thin disks is discussed.

1.3.2 X-ray Observations in this Thesis

In the third part of the thesis we present results of the analysis of X-ray data from several one day observations of the Seyfert 1 galaxy MCG -6-30-15 over a period of five years. This extensive analysis was designed to reveal the possible structure of the central engine in this source. These results are particularly interesting in the context of the theoretical part of this thesis.

The observational part of our work is discussed in chapters §5 and §6. In chapter §5 we describe physics of proportional counters which are used in the detection of X-rays. The detectors on board the Ginga and ROSAT satellites, with which the data analyzed in this thesis was collected, are also described. In the last part of chapter §5 we describe the methods by which background is subtracted and the method by which the spectra are selected and sorted. The analysis of data from the Seyfert 1 galaxy MCG -6-30-15 is described in chapter §6. The analysis of spectral and flux variability and the possible explanations in term of simplified models are also presented in that chapter. Implications of the observations, and other X-ray observations of Seyferts, are discussed in chapter §7, the last chapter.

Chapter 2

EQUATION OF STATE FOR THE CLOUD MODEL

In this chapter the equations of state for clouds in the central engines of AGN are presented. In the first section we present the theoretical and observational arguments for a two component configuration. In the second section we develop the equations for a simplified spherically symmetric case. In the third section we solve the equations for a stationary case in which the physical parameters are distance dependent, and compare the results with other solutions for the central engines.

2.1 REASONS FOR THE TWO COMPONENT CLOUD MODEL

2.1.1 Theoretical Reasons for the Cloud Model

The approximate radiation density and matter density in the central engines of

AGN can be found from observations. For radio-quiet AGN the observations indicate that the densities, and the resultant compactness (see table 1), may induce strong coupling of matter and radiation. This coupling results in rapid local cooling, and the creation of two components: the radiative 'hot' component ($k_B T \sim mc^2$) is dispersed throughout the central engine, and the denser 'cold' (not completely ionized) component, which reprocesses the radiation, form clouds.

The radiation and matter densities, pressure and temperature of the central engines of AGN can be determined by using three observed quantities: the luminosity, the doubling timescale and the absorption column, which is the number per cm^2 of atoms in the line of sight to the inner parts of the central engine.

We shall limit our discussion to a large sub-group of AGN, radio quiet quasars (QSO) and Seyfert nuclei, in which the central engine is most readily observed. Seyferts and QSO may be the 'cleanest' example of AGN as far as exploring the central engine is concerned, and are also the most abundant (Woltjer 1990, appendix I). Another advantage of limiting consideration to this subgroup is that some QSO, which were identified as point sources when first observed, have already been resolved and found to be galaxies which harbor an active center. A large range of observational parameters is therefore available for comparison with our model.

The AGN flux from QSO and Seyfert 1 nuclei is observed to double (in X-rays) in hours (some Seyferts) or days (quasars), which implies that their size is much smaller than that of the host galaxy. If the variability amplitude is large, the size of the source is determined by the doubling time scale

$$R_X = c\Delta t, \tag{2.1}$$

where R_X is the size of the X-ray source, c is the speed of light and Δt is the observed shortest time scale of large amplitude variability. In AGN this time scale is usually taken to be the minimum interval in which the source doubles its output. For the observed variability timescales the size which is found to be $R_X = 10^{12-15}$cm is of order of the size of the solar system at the large end. The size of the SMBH must be smaller than the size of the X-ray source but cannot be much smaller, or else matter will not be efficiently captured and accreted. Assuming that a SMBH is responsible for the accretion of the emitting matter and that the emission comes from $\sim 10R_g$, where $R_g = GM/c^2$, and the mass of the SMBH is found to be of order $10^{6-9}M_\odot$, where $M_\odot = 2 \times 10^{33}$gr is the mass of the sun (Blandford 1990). The efficiency of accretion onto black holes varies from ~ 0.06 for accretion onto a Schwarzschild black hole to ~ 0.4 when the accretion is onto a fast rotating Kerr black hole. Most of the energy is released near the horizon of the black hole, at $\sim 10R_g$ (Blandford 1990).

Radio and optical observations have found the central source to be smaller than $\sim$ 0.1pc, which, however, is still more than three orders of magnitude larger than the suggested X-ray region. This is an upper limit on the size. The smaller sizes are also inferred from the mechanisms for the production of jets, where these are observed in other types of AGN (using certain unification of schemes of AGN). Future observations by missions such as the COSTAR on the HST and the advanced X-ray facility (AXAF) will determine weather the smaller size is valid for these sources.

Observed values for the total luminosity vary from 10^{41-44} ergs sec^{-1} for Seyferts to 10^{44-47}ergs sec^{-1} for QSO, requiring an extremely efficient radiation mechanism. There is an inherent uncertainty in the above numbers, due to lack of observations in EUV regime in which the emission is generally expected to be the strongest. However, recent observations by the European ROSAT satellite in the soft X-ray waveband, and by the international UV explorer (IUE) in the near UV band, have confirmed the existence of excess of radiation in the EUV band in many cases (see also section §2.1.2).

The supply of matter to the central engine must exceed

$$\dot{M} = \frac{L}{\eta c^2}, \tag{2.2}$$

where η is the fraction of accreting matter turned into energy and L is the observed

luminosity. The rate of accretion is therefore $\dot{M} \sim (10^{20-23}/\eta)$gr sec^{-1} for Seyferts.

A primary reason for a two component medium is the physical availability of pressure that enhances perturbations. For example, when the source radiation pressure exceeds the gravitational pull the overly dense regions are compressed by radiation pressure. These compressed regions emit synchrotron and Compton radiation and may cool. The cooler regions have higher cross-section for Compton scatterings, and are therefore compressed and cooled even more. When the matter is sufficiently cool the bremsstrahlung and recombination radiation, which depend on the square of the gas density, dominate. Further cooling and density increase stop when the matter reaches local thermal equilibrium (Guilbert and Rees 1988, Ferland and Rees 1988). Although radiation pressure is easily understood, the main reason for this local density increase may be twisted magnetic fields, probably in a configuration similar to that observed in quiescent solar prominences (such as in Priest, Hood and Azner 1989), which channel cold matter into low field high gradient regions.

Observations imply that cold matter is close to the center, or within the central engine. The above theoretical argument for the existence of cold plasmas in the central engine comes from measuring source compactness. Sources which are near their Eddington limit are optically thick if the accretion is locally homogeneous and

isotropic. When the Eddington luminosity is reached matter is accelerated outward, because the radiative force on each particle equals the gravitational force

$$\frac{L_{Edd}\sigma_T}{4\pi R^2 c} = \frac{GM\mu m_H}{R^2}, \tag{2.3}$$

where L_{Edd} is the Eddington luminosity, σ_T is the Thompson cross section and μm_H is the mass of an average cosmic abundance atom. Accretion may continue if it is not isotropic, depending on the configuration.

This result may indicate that a thin accretion disk is the preferable geometrical configuration for the central engine. However, it has long been known that the spectrum and light curve of radio quiet AGN cannot be explained by the standard thin disk model alone, and that an optically thin hot relativistic plasma in the vicinity of the compact object may be responsible for a large portion of the continuum X-ray emission (Price & Thorne 1975, Shapiro Lightman & Eardley 1976). This region may form when the inner regions of a thin disk inflate due to thermal instability (Lightman & Eardley 1974). Models with thin cold disk and hot corona are discussed in chapter 7. We show that high compactness sources must have an optically thick component somewhere in the hot relativistic plasma (Guilbert and Rees 1988, Lightman and White 1988, Sivron and Tsuruta 1993). The location in which the cold component forms is arbitrary, and it is therefore imperative that we shall start our study of the

central engine with a general form of cold matter distribution, not only an a priori disk configuration.

2.1.2 Observational Reasons for the Cloud Model

There are three types of observations that imply the existence of cold matter in the central engines of AGN: The spectrum of AGN continuum radiation may be described as a combination of of hot and cold components spectra; The temporal variability may be described as a typical hot component variability which is filtered by the cold component; Multi-frequency observations of short term variability may provide evidence for the existence of cold matter inside the central engine.

The spectrum of a typical radio quiet AGN is almost 'flat' (see figure 1-1), which is typical of hot, optically thin, matter. This property was the reason for the variety of theories that explained the spectrum as one power-law from one region. One such theory is the synchrotron self-Compton model (SSC, see Blandford 1990), in which a power-law spectrum from the synchrotron self absorption edge at $\nu \sim 10^{12}$ sec^{-1} to the pair-plasma 'break' at $\nu \sim 10^{20}$ sec^{-1} (see Ghisellini and Haardt 1994 and references therein) gives rise to features such as a possible hard x-ray tail, by self Comptonization of the same synchrotron radiation. In this model the source of emission is an almost optically thin relativistic plasma of temperature 10^{9-12}K,

which is located in, or near, the central engines of AGN. In another mechanism, usually referred to as the Compton mechanism, pairs and electrons in a hot plasma component in the central engine scatter photons from a 'cold' (not completely ionized) component, which results in the creation of a power law spectrum.

Recent observations in the UV and soft x-ray parts of the spectrum have revealed that a large portion of the luminosity in these wavebands is better characterized as thermal spectrum, typical of a cold, optically thick, matter. The overall portion of the total luminosity that can be characterized as thermal UV bump is:

$$0.3 \leq \frac{L_T}{L_{NT}} \leq 3, \tag{2.4}$$

where L_T is the thermal luminosity and L_{NT} is the power-law non-thermal luminosity (Lightman and White 1988).

Another reason for considering a two components cloud model comes from studies of the random shot noise and chaotic variability which is typically observed in AGN (see section 1-5 in chapter 1). The power spectrum can be best fit with a $1/f$ slope in some strong AGN, or with $1/f^2$ for some very weak AGN and galactic black-hole candidates (McHardy 1988; Green 1993, and references therein). The variability in high luminosity sources can be accounted for if there is an increase in cold matter which reprocesses the original random shot noise in these sources. The slope of the

power spectrum can also be flattened because of pairs, which are more copious if the luminosity to size ratio is large, and may increase the rate of cold component matter production (see also chapter 4).

Multi-frequency observations have not yet revealed the existence of cold matter in the central engine. In the recent multi-frequency observation campaign, organized by Prof. S. Tsuruta of Montana State University, it was found that at least in one example less than 5% of the luminosity in the IR and optical parts of the spectrum vary simultaneously with the mostly power-law X-ray emission (Done et al 1991). This observation may rule out the SSC model, or imply the filtering out by clouds of the optical - IR components of the spectrum (Celotti, Fabian and Rees 1992). Future observations with better statistics and improved spectral techniques may reveal better evidence for cold matter in the central engine.

2.2 THE EQUATION OF STATE

In deriving the equations of this section the general approaches of Guilbert and Rees 1988, Lightman and White 1988 and Celotti Fabian and Rees 1992 are followed. The observables used in our framework are the X-ray luminosity L_X, the mass of the SMBH M and the total number of cold absorbing atoms in a cm^2 column in

the line of sight N_H (the absorption column density). In the computer code we used the fraction of the total 4π solid angle available for light to freely escape the central engine, $0 < f(N_H, M, L_X) < 1$ (the covering factor) as a variable. In this chapter our attention is confined to accretion-powered AGN radiating close to the Eddington limit.

We first describe the isotropically accreting matter. The total luminosity in equation (2.2) determines the isotropical accretion rate and local density

$$\dot{M} \sim 4\pi R^2 n_{avg} m_H v_{acc} \tag{2.5}$$

where v_{acc} is the velocity at which matter is accreted onto the SMBH. The accretion rate can be also written as

$$\dot{M} = 4\pi R^2 n_{avg} m_H \, (v_{acc}/v_{ff}) \, \sqrt{2GM/R} \tag{2.6}$$

where $n_{avg}(R) \sim \rho_{avg}/m_H$ is the average number density of the infalling matter. Since the cosmic abundance presumed is mainly made of hydrogen with mass m_H we assume this to be the mass of all infalling particles. (The abundance can easily be changed by replacing M_H with an arbitrary μm_H. We choose $\mu = 1$ to be consistent with Guilbert and Rees 1988 and Celotti Fabian and Rees 1992.) The free fall velocity v_{ff} is assumed to be Newtonian. As a first order approximation the accretion rate,

which is the solution of the spherically symmetric continuity equation, is assumed to be independent of R, the distance from the SMBH. This approach renders our treatment stationary. Dynamical considerations are discussed in chapter 4.

The minimal optical depth of isotropically infalling matter is determined by

$$\tau \geq \int \kappa_{es} n_{avg}(R) m_H dR, \tag{2.7}$$

where k_{es} is the opacity for electron scattering. Substituting equation (2.6) in equation (2.7) and integrating over the central engine we get:

$$\tau \geq 0.4 \frac{R}{4\pi R^2} \frac{L}{\eta c^3} \left(\frac{v_{ff}}{v_{acc}}\right) \sqrt{\frac{R}{2R_g}}, \tag{2.8}$$

where R here is the size of the central engine. Equation (2.8) can be written in a more convenient form,

$$\tau \geq 10 \left(\frac{\eta}{0.1}\right)^{-1} \left(\frac{L}{L_{edd}}\right) r^{-1/2} \left(\frac{t_{acc}}{t_{ff}}\right), \tag{2.9}$$

where t_{acc}, the accretion timescale, is assumed to be proportional to t_{ff}, the free fall timescale. This dependence shows that geometrically extended central engines, such as those expected in the case of extended two temperature ion torus (Rees et al. 1982), may survive without transition to two components. The optical depth τ would exceed 1 near the center when the source is radiating close to L_{edd} (Guilbert

and Rees 1988). Thus the original power-law emission, which is probably emitted from the inner $10R_g$ (Blandford 1990), will inevitably be shrouded and reprocessed by the infalling matter. Consequently the final spectrum deviates significantly from a simple power-law even if the luminosity is an order of magnitude smaller than the Eddington luminosity (Guilbert and Rees 1988, Lightman and White 1988). The slight inverse dependence on the distance is the result of the crude approximation adapted, and is especially inaccurate for large optical depths which include processes other than electron scattering.

Using the same arguments as the ones in equation (2.7) (where we use (2.15) for the density) and integrating radially over one cloud, the optical depth of a cloud in the two component configuration is calculated. Each of the cold plasma clouds has optical depth

$$\tau_{1cld} = \int_{\nu_{min}}^{\nu_{max}} d\nu \frac{(\kappa_\nu + \kappa_{KN}) 3\, L_\nu \xi}{16\pi^2 \eta n_{cld} l_{cld}^3 (v_{acc}/v_{ff}) \sqrt{2GM}} \left(\frac{1}{\sqrt{R}} - \frac{1}{\sqrt{R + l_{cld}}} \right), \qquad (2.10)$$

where κ_{KN} and κ_ν, the Klein Nishina and bound-free opacity, respectively, replace the electron scattering opacity. The radius of one cloud is l_{cld}, n_{cld} is the number density of clouds at the particular radius, and ν is the frequency. From radiative transfer (see chapter 3) one can see that the total high energy flux coming out of this region is roughly $L(out) = Lexp(-\tau_{1cld} R/l_{cld})$. A more accurate optical depth,such

as the one presented by Ferland and Rees 1989 and Netzer 1993, includes the atomic properties and the Einstein Coefficients.

Because of fast Compton and faster bremsstrahlung and bound free cooling most of the shrouding infalling material should be relatively cold. The minimum temperature can be derived for thermal matter which emits as much energy as it radiates: $4\pi l_{cld}^2 \sigma_B T^4 = (1-A)L(1-exp(-\tau_{1cld}))exp(-f(R))/(4\pi R^2)$ from which we get

$$T_{cld} = \left((1-A) \frac{L}{16\sigma\pi R^2} \left(1 - e^{-\tau_{1cld}}\right) e^{-f(R)} \right)^{1/4}, \qquad (2.11)$$

where A is the flux averaged albedo (per cloud) and $f(R)$ is the covering factor at R (see equation 3-12 for $f(R)$ and 3-10 for the albedo). An equality is reached if n_{th}, the cold cloud's number density, is high enough so that the cooling time $t_{bound-free} << t_{brems} << t_{synchro-Compton}$ or t_{pairs}, where $t_{bound-free}$ is the timescale for cooling due to matter that is not completely ionized.

Such densities can result from a confining pressure supplied by an equipartition magnetic fields, $P_{magnetic} = B^2/16\pi \sim GM/R$, as in Rees 1987, (or, in a disk configuration, from the differential gravitational pull of the black hole). A two phase structure with dense cold clouds and hot relativistic component forms when the cooling time in the dense phase is shorter than the infall time scale by a factor which

accounts for the ratio of photon energy to particle energy

$$t_{brems}(T) < (GM/R^3)^{-1/2}(kT_{cld}/\eta m_p c^2), \tag{2.12}$$

where $t_{brems} = \alpha_f^{-1}(kT_{cld}/m_e c^2)^{1/2} 1/(n_e \sigma_T c)$. This cooling argument may also be explained as follows: since in a typical infall time scale a particle in the hot phase gains energy of order GMm_p/R and since at the same time the cold phase is cooling via bremsstrahlung in which every collision releases a photon of energy which exceeds kT_{BB}, there must be at least enough such photons released such that no energy is gained. The above relation will result in a very high density.

By equating the thermal pressure with the confining magnetic virial pressure we get (Guilbert and Rees 1988, Lightman and White 1988):

$$\frac{n_{th}}{n_{avg}} = m_p c^2 \left(\frac{R}{2R_g}\right)^{-1} \frac{1}{kT_{cld}}. \tag{2.13}$$

Note that the inverse of this ratio is approximately the filling factor. Also note that the radiation pressure is proportional to the virial magnetic pressure, but that dynamical motions are than required. (Equation (2.13) presumes the gas equation for the hot component. This assumption is valid for the stationary equations. In cases where the total energy of the hot component doubles in seconds this assumption may not be valid. See also chapter 4.)

Combining equation (2.12) with (2.13) , and using (2.4) and (2.6) for the average density and the Eddington luminosity, we get that when the inequality

$$\alpha_f^{-1}\eta^2\left(\frac{kT_{cld}}{m_e c^2}\right)^{1/2}\left(\frac{L}{L_{Edd}}\right)^{-1}\left(\frac{R}{2R_g}\right)\left(\frac{t_a}{t_f}\right)^{-2} < 1 \qquad (2.14)$$

is fulfilled a dense phase will stay cold. It is evident that this inequality holds for near Eddington luminosities.

Using the same arguments that lead to equation (2.5), the isotropic accretion of cold component clouds should obey:

$$\frac{dM_{cld}}{dt} = \frac{4\pi R^2\, n_{cld}\, 4\pi l_{cld}^3\, n_{th} m_H\, v_{cld\,acc}}{3}, \qquad (2.15)$$

where $v_{cld\,acc}$ is the accretion velocity of clouds.

If the requirement that the clouds hold a significant fraction of the infalling mass is fulfilled a condition on the size of the clouds can be found. We rewrite equation (2.16) as

$$\frac{dM}{dt} = \frac{L\xi}{\eta c^2} = \frac{4\pi R^2\, n_{cld}\, 4\pi l_{cld}^3\, n_{th} m_H\, v_{acc}}{3}, \qquad (2.16)$$

where ξ is the fraction of the mass in the clouds, and $\dot{M} = const(R)$. This condition will be fulfilled if a significant fraction of $\dot{M}$ in the form of clouds does not fall into the equatorial plane to form a geometrically thin accretion disk, when the clouds are small and dense enough so that the time scale for cold matter to fall onto a disk

is longer than the typical infall time scale R/v_{ff}. We take the typical collision time $t_{coll} \leq 1/(n_{cld}\pi l_{cld}^2 v_{cld})$ to be the time scale of falling into a disk. From this requirement we obtain the following relation between n_{cld} and l_{cld}:

$$n_{cld} l_{cld}^2 < \left(\frac{v_{cld}}{v_{ff}}\right)^{-1} (\pi R)^{-1}. \tag{2.17}$$

The cloud velocity v_{cld} is uncertain, but it may be assumed to be Keplerian. Plugging equation (2.16) in (2.17) and using the definition of compactness in section 1.1 of chapter 1 one get

$$n_{th} l_{cld} > 10^{24} \left(\frac{l\xi}{16\pi\eta}\right) cm^2. \tag{2.18}$$

We see that semi spherical accretion in radio quiet AGN may take place for clouds of sizes less than $l_{cld} \sim 10^8$cm and atomic number density $n_{cld} \sim 10^{16}$ which is expected in the central engine. A typical cloud of size $10^6 - 10^8$cm is much smaller than the size of the central engine in radio quiet AGN. The above consideration is a simplified form of the macroscopic equation of motion for clouds which is further considered in chapter 4.

When the condition of equation (2.18) is not met the configuration is a disk full of clouds, or clouds which collapse to form a flat thin disk with sheets and filaments that still hover above and below the disk. In such case equation (2.16) includes another

parameter for the fraction of accreting matter in the clouds.

2.3 RESULTS

By simultaneously solving our basic equations, (2.10), (2.11), (2.14) and (2.17) the radial distribution of our characteristic parameters is obtained. For the spherical accretion of inhomogeneities we assume functional R dependence for the following quantities:

$$n_{th} = n_{th}(R_{max})\left(\frac{R}{R_{max}}\right)^{-\delta} \tag{2.19}$$

$$T_{cld} = T_{cld}(R_{max})\left(\frac{R}{R_{max}}\right)^{-\lambda} \tag{2.20}$$

$$n_{cld} = n_{cld}(R_{max})\left(\frac{R}{R_{max}}\right)^{-\chi} \tag{2.21}$$

$$l_{cld} = l_{cld}(R_{max})\left(\frac{R}{R_{max}}\right)^{\iota}. \tag{2.22}$$

Radial dependence is justified for high enough accretion rates, such that $\tau \geq 1$ in equation (2.7), and small enough clouds, such that (2.18) is fulfilled. The maximal radius, R_{max}, is the outer boundary in which the cloud model works. The reason that

the clouds, sheets and filaments have distance dependence physical properties, is that magnetic stresses, or the shocks, which probably result in the formation of the cold phase, are distance dependent (see also chapter §6). Equations (2.19) - (2.22) give us four unknown exponents.

These exponents can be found if the covering factor and albedo are small and the optical depth per cloud is large. The radial dependence of the temperature assumes small covering factor, and thus it is easily seen from equation (2.11) that $T_{cld} \propto R^{-1/2}$, or $\lambda = 1/2$. Furthermore, if the virial dependence of the confining pressure holds, as in equation (2.13), we find that $m_H n_{th} \propto R^{-5/2+\lambda}$, which gives an inverse square R dependence for the number density of cold plasma in the clouds with small covering factor. This result is encouraging. In a typical Seyfert galaxy the density needed for LTE in the central engine is approxImately $n_{th} = 10^{16} cm^{-3}$ for a Bolometric luminosity of $10^{44} erg/sec$, which is the minimum needed for there to be an effective clouds coverage. One may compare this density to the broad line region clouds at $\sim 10^4 R_g$, which have a density of $n_{th} \sim 10^{10} cm^{-3}$ in Seyferts. From this observational result we also get $n_{th} \propto R^{-2}$. When we include the theoretical results of Celotti, Fabian and Rees 1992 which require that the number density in a cloud near the SMBH is approximately $n_{th} = 10^{16-18} cm^{-3}$ for an absorption column of $N_H \leq 10^{21} cm^{-2}$, such

that the IR-optical wave bands are blocked we find that $n_{th} \propto R^{-2} - R^{-2.66}$. We like to stress, however, that this does not imply that the BLR clouds and the clouds in the central engine a part of the same physical mechanism. Using equation (2.18) the dependence of the clouds' size exponent have $\iota \sim 1 - 2$ and the cloud number density has the exponent $\chi = 3 - 4$.

With the above results we are confident that the equations above can be used in the radiative transfer code.

Chapter 3

THE RADIATIVE TRANSFER FOR THE CLOUD MODEL

The radiative transfer equation for a two component cloud model is presented and used for the calculation of output spectra in several wavebands. We assume that these clouds have many similar properties, and develop a macroscopic radiative transfer equation. The radiation transfer problem is written for macroscopic bodies, such as a multitude of clouds, and an optically thin hot component. The spatial distribution and physical properties of clouds roughly follow the equations of chapter 2. Possible solutions of the radiation transfer problem are outlined.

3.1 RADIATIVE TRANSFER FOR THE TWO COMPONENT MEDIUM

In this section the radiation transfer equation is described. We compare absorption and emission by clouds to the well known atomic absorption and emission processes. We than combine absorption and emission to form the full radiative transfer equation.

3.1.1 Absorption and Emission by Macroscopic Inhomogeneities

Absorption by atomic processes and absorption by clouds are similar. The absorption due to atoms with cross section σ_ν is $dI_\nu = -\sigma_\nu n I ds$, where I is the specific intensity (Rybicki and Lightman 1979), the absorption coefficient is $\alpha_\nu = \sigma_\nu n$, and the solution for constant α is $I = I(s=0)\, e^{-\alpha s}$. The absorption by cold clouds can be expressed as

$$dI_{\nu,\Omega} = (-)A(\Omega)\, n_{cld}\, I_\nu\, ds, \qquad (3.1)$$

where $A(\Omega)$ is the effective area of a cloud and the subscript *cld* is used indiscriminately in this chapter for clouds of arbitrary and specific shapes. The area of an opaque spherical cloud, $A_{cld} = \pi R_{cld}^2$, is the same as its cross section. (Optically thin clouds have frequency dependent smaller cross section.) For spherical opaque clouds

we therefore have a typical extinction of the intensity:

$$I_\nu = I_\nu(0) exp(-n_{cld} \pi R_{cld}^2 s). \tag{3.2}$$

In figure 3-1 we see the expected distribution of absorbing clouds in AGN and the resultant outcoming radiation.

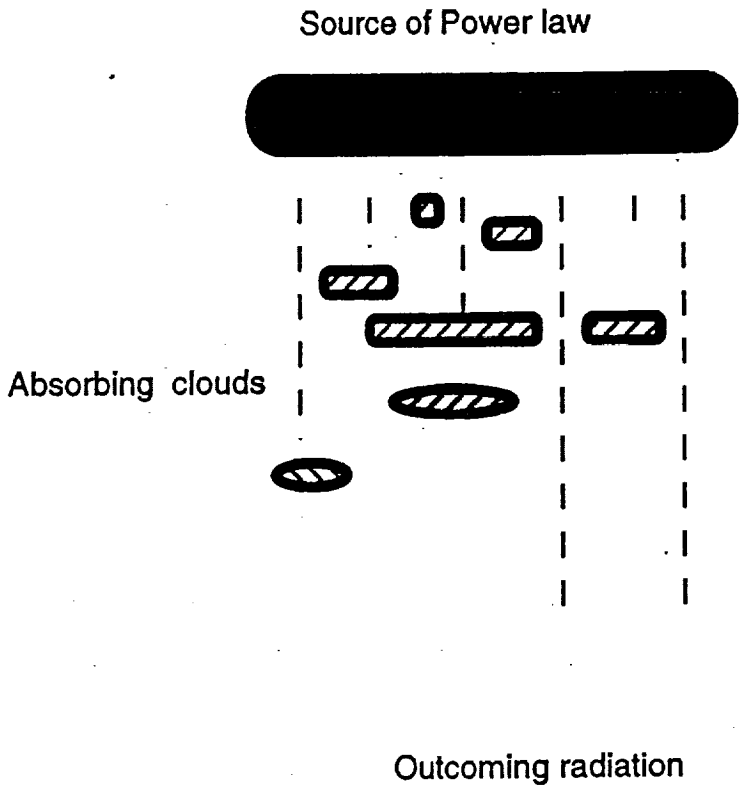

Figure 3.1: Absorption by optically thick clouds

Atomic materials and clouds both have direction dependent, and direction independent types of emissions. The emission generated by atomic material is

$$j_\nu = \frac{dE}{dV d\Omega d\nu dt}. \tag{3.3}$$

The intensity added to a beam traveling a distance ds through a volume element of unit area in an inhomogeneous material is

$$dI_\nu = j_\nu n_{cld}\, ds, \tag{3.4}$$

where j_ν is the emission coefficient for one cloud, and an exponential gain from the medium is possible, if $j_\nu \propto I_\nu$ (see, for example, appendix 1). Atomic emission may be of the type

$$j_\nu = \frac{e^2\omega^4 A^2 \cos^2\theta}{3c^2 4\pi} = \frac{P_{Larmor}}{4\pi}, \tag{3.5}$$

where A is the amplitude of oscillations of a dipole. Thermal emission is an example of an isotropic emission. A black-body (Kirchoff's - law) emission is:

$$j_\nu = n\sigma_\nu \frac{2h\nu^3/c^2}{exp(h\nu/kT) - 1}, \tag{3.6}$$

which is the result of equilibrium of absorbed and emitted radiation.

The emission by clouds, which is not necessarily isotropic, has the form:

$$j_\nu \, n_{cld} = \left(\frac{dE}{dV \, d\Omega \, dt \, d\nu} \right), \tag{3.7}$$

where j_ν is the emission of one cloud, and n_{cld} is the number of clouds per unit volume. (This number will usually be very small, of order $10^{-30}\mathrm{cm}^{-3}$). We define the emission per cloud to be j_ν, because of the simplicity in adding cloud emission spectra to the computer code. For reflecting clouds j_ν is direction dependent. In this thesis, for the case of optically thick matter, we simplified this problem by using the 'moon phases method' (see appendix 2). For optically thin matter a Monte-Carlo simulation for one cloud will give an angle-dependent emission (see, for example, Bond and Matsuoka 1994 and George and Nandra 1994).

In figure 3-2 we see the expected emission from an optically thick cloud in the central engine of an AGN.

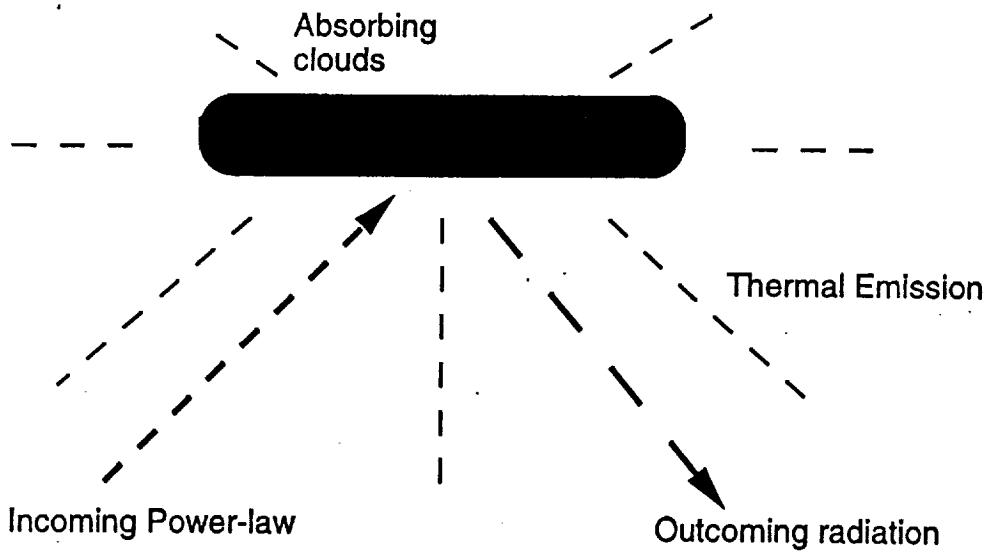

Figure 3.2: Compton reflection and thermal emission from optically thick clouds

3.1.2 Radiative Transfer in a Two Component Medium

Several simplifying assumptions have to be made in order to write a macroscopic radiative transfer equation. The radiative transfer equation for clouds is macroscopic in the sense that the absorbing and emitting elements are macroscopic bodies. In our code the non-thermal source is represented by a point source that emits a power-law spectrum from the innermost region of the central engine. This assumption is justified by the results of section 1.2 in chapter 2 and section 2 of chapter 4. The model also has to satisfy the variability requirement imposed by the absence of IR-optical variations during X-ray flares from Seyfert nucleus NGC 4051 (Done et al. 1991). Therefore, we assume that the IR-optical portion of the primary radiation is effectively absorbed by the extremely small 'cloudlets' within $10R_g$, which are transparent to the higher energy photons. Celotti Fabian and Rees (1992) predict the existence of such cloudlets, which we shall call 'the CFR cloudlets'. In our cloud model this modified spectrum is used as the input radiation, to be reflected and reprocessed by an assembly of cold, optically thick clouds. (The energy from the IR-optical wavebands is added to the UV band.) The inner boundary in our calculations is therefore $\sim 10R_g$. (We note, however, that in models with pair plasmas the intensity of optical-IR radiation from the central engine is inherently small, and CFR cloudlets

are not necessary.)

The clouds in this thesis are distributed over a spherical region from R_{min}, just outside the outer boundary of the innermost region with CFR cloudlets, to some maximum radius R_{max}. The outer boundary, R_{max}, may be as large as the radius in which the outer thin disk is unstable (see chapter 2). We generally assume $R_{max} \sim 100R_g$, outside of which the thin disk approximation should work (see, for example, Frank, King and Raine 1992). Since the IR-optical wave bands have been filtered out from the synchro-Compton spectrum by the CFR cloudlets, the radiation pressure on the cold clouds due to atomic absorption processes is significantly reduced. Clouds larger than the CFR cloudlets can therefore exist in a region larger than R_{min}, where optically thick clouds are assumed in our work.

Using the above assumptions the observed spectrum I_{obs} is calculated. The radiation transfer equation for the modified power-law source around which clouds are isotropically distributed (Sivron and Tsuruta 1993). The power-law source can be described as $I_{in}(0) \propto E^{-\Gamma}$ in most parts of the spectrum, where $E = h\nu$ is the energy of a photon, and Γ is the photon index. The radiative transfer equation is thus

$$I_{obs}(s) = I_{in}(0)\, e^{-\tau_{cld}} + \int_0^{\tau_{cld}} e^{-(\tau_{cld}-\tau'_{cld})}\, S_{cld}(\tau'_{cld}) d\tau'_{cld}, \qquad (3.8)$$

where s is the path length and $I_{in}(0)$ is the input spectrum. The optical depth of this

assembly of clouds is

$$\tau_{cld} = \int_{s_0}^{s} ds' \alpha_{cld}(s'), \tag{3.9}$$

which is independent of τ_{1cld} for opaque clouds. The absorption coefficient for an optically thick spherical cloud is $\alpha = n_{cld}\pi l_{cld}^2$. The source function S_{cld} is the energy dependent emission coefficient from one cloud divided by its absorption coefficient.

The outcoming spectrum has three parts. The first part is due to the reflection of partially absorbed power law emission from the clouds

$$I_{ref} = \int_{Rmin}^{Rmax} dR \int_{\theta=0}^{\pi} d\theta \left(2\pi R^2 \sin\theta \, e^{-f(R)} \left\{ S_{ref} \, n_{cld} \frac{\pi l_{cld}^2 (1 + \cos\theta)}{4\pi R^2} \right\} \right. \tag{3.10}$$

$$\left. \left(exp - \int_{\tilde{\theta}=0}^{\pi - \arcsin(R\sin\theta/R_{max})} d\tilde{\theta} \sin\tilde{\theta} R n_{cld} \pi l_{cld}^2 \right) \right),$$

where θ is the angle subtended by the central source and the observer at the cloud. The source function $S_{ref}(n_{th}(R), I_{int}(R), \nu)$ (see, for example, Lightman and White 1988) is a result of reflection from an individual cloud at R. For example, the solution of the radiative transfer equation for low energies is given by $S_{ref} = I_{in}(R)(1 - \sqrt{\epsilon})/(1 + \sqrt{\epsilon})$, where $\epsilon = \kappa_\nu/(\kappa_\nu + \kappa_{es})$ (see appendix 3). The free-free opacity κ_ν depends on the density $n_{th}m_H$ of a cloud, which is derived from equations (2.13) and (2.16). of this chapter.

The additional effects of the relative orientation of the cloud with respect to the central point source and the observer are taken into account by the method of moon phases (see appendix 2). For example, the decrease in reflection from a single spherical cloud is proportional to $\pi l_{cld}^2(1+\cos\theta)$, similar to the solution for the luminosity of the moon phases. The decrease due to this moon phases effect is crudely of the same order of magnitude as that of a circular slab tilted at an angle of $\theta = 0 - 60$ degrees (see, for example, the results of the Monte-Carlo simulation in George and Fabian 1991, Fig 12). The occultation of radiation after it is reflected from the cloud is taken into account in the second exponential in equation (3.10).

The thermal component of the outcoming radiation due to absorption and re-emission by the clouds is calculated from:

$$I_{thermal} = \int_{Rmin}^{Rmax} dR \int_{\theta=0}^{\pi} d\theta \left[n_{cld}\, 2\pi R^2 \sin\theta \left\{ F_{thermal}\, \pi l_{cld}^2 \right\} \right. \\ \left. \left\{ exp(- \int_{\tilde{\theta}=0}^{\pi - \arcsin(R\sin\theta/R_{max})} d\tilde{\theta} \sin\tilde{\theta} R n_{cld} \pi l_{cld}^2) \right\} \right], \tag{3.11}$$

where $F_{thermal}(T_{cld}(R))$ is the thermal radiation flux from the surface of the cold clouds, and $T_{cld}(R)$ is found from equations (2.11) and (2.19).

It is convenient to define a covering factor for the central engine. We define the

covering factor to be

$$f(R) = \int_{R_{min}}^{R} n_{cld} \pi l_{cld}^2 dR. \tag{3.12}$$

The covering factor at R_{max} is the total optical depth τ_{cld} for the radially propagating photons. If $f(R_{max}) > 1$ our integrals should be expanded to include two reflections and more, using a perturbative method. If $f(R_{max}) >> 1$ the above treatment does not work, and the region may be treated as an optically thick photosphere. The covering factor at R_{max} is a free parameter in our code.

The observed reprocessed radiation is therefore

$$I_{obs} = I_{in}(0) e^{-\tau_{cld}} + I_{ref} + I_{thermal}. \tag{3.13}$$

The integral of this spectrum, L, is equal to the integral over the primary spectrum, because we assumed that there is no internal source of energy for the clouds. The emission may be anisotropic if the number of clouds is very small.

In figure 3-3 we show the radiative transfer in a simplified geometry. The power-law source is in the center of a spherical distribution of spherical clouds. The clouds in our model absorb, emit and reprocess the power-law radiation. The effects of distance from the central source are expected to be implemented through the r dependence of the physical parameters calculated in chapter 2.

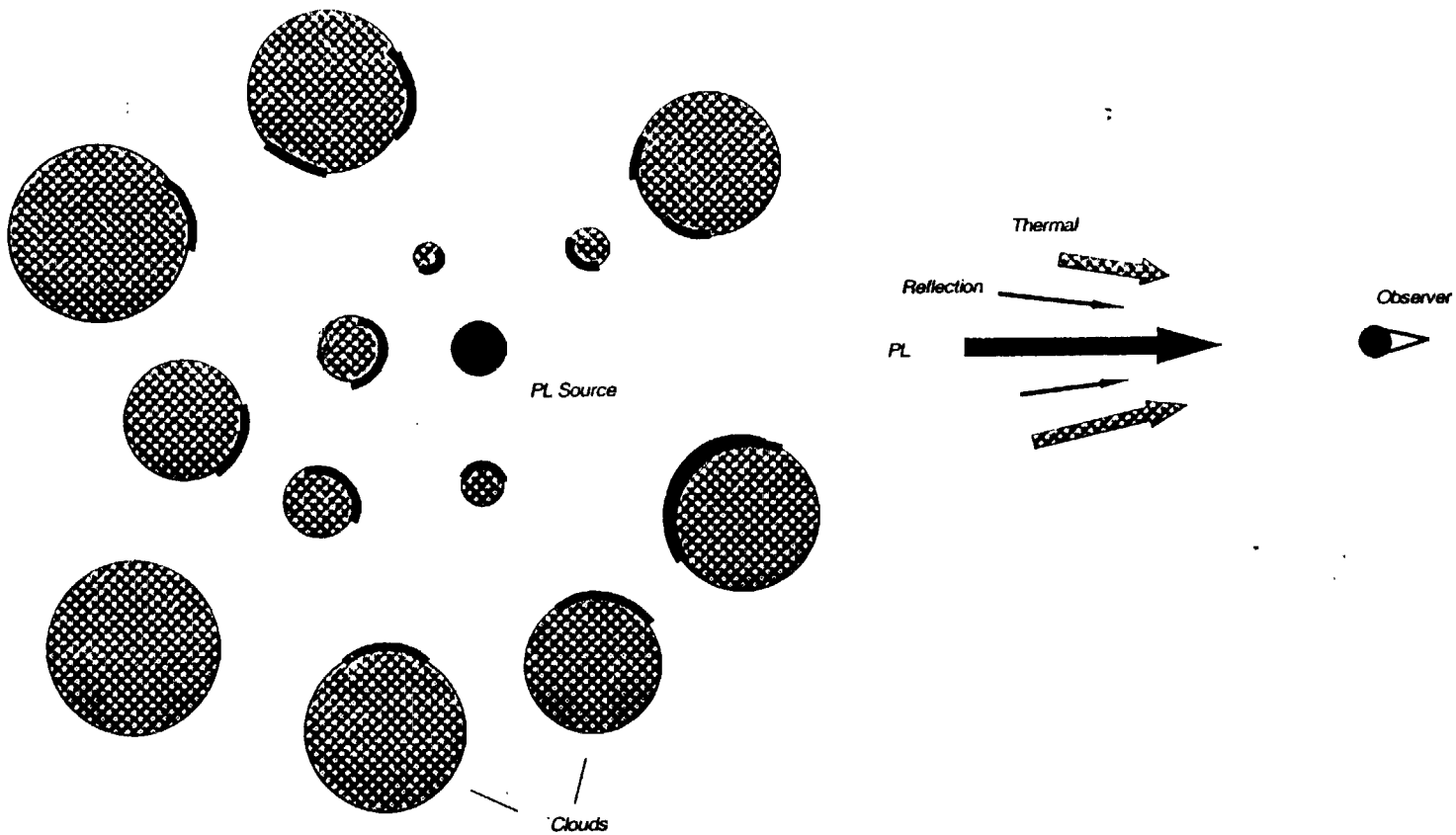

Figure 3.3: Radiative transfer near the central engine in the cloud model

3.2 RESULTS

In this section we present the spectra from our numerical solution of equation (3.13), and explain the consequences of these results. In figure 3-4 we show the different spectra for different covering factors. Small covering factor, $f(R_{max}) < 1$ and large optical depth per cloud $\tau_{1cld} > 1$ are assumed. Note that for $f(R_{max}) = 0.9$ the central source is heavily attenuated and the spectrum exhibits many spectral features. The spectra in figure 3-4 and figure 3-5 have no R dependence for the covering factor, no R dependence for the temperature and R^{-2} dependence for the density. The optical depth of each individual cloud is assumed to be much larger than unity. We study the conditions under which these assumptions are valid in the following two paragraphs.

The four unknowns n_{th}, T_{cld}, n_{cld} and l_{cld}, which determine S_{ref} and $F_{thermal}$, are obtained by solving equations (2.11), (2.13), (2.15) and (2.17) for the spherically symmetric region. Unlike the case in section 2 of chapter 2 in which we assumed $f(R_{max}) << 1$ the exponents of equations (2.19) - (2.22) can not be found explicitly. It is therefore important to check the limits on the exponents.

For optically thick clouds the final spectrum is not very sensitive to variations in

the radial dependence of the cold density $m_H n_{th}$, because the R dependence of S_{ref} is proportional to $(1-\sqrt{aR^{-2\delta}/b+aR^{-2\delta}})/(1+\sqrt{aR^{-2\delta}/b+aR^{-2\delta}})$, where a and b are comparable (see appendix 1). The dependence of spectrum on R is extremely sensitive to temperature variations because $T \propto R^{\lambda}$, and the emission is proportional to $R^{-4\lambda}$. This result is expected to be limited to the cases of high accretion rates in which optical thickness is achieved for most clouds, but may be far from true for optically thin clouds with cold matter. The radial dependence of n_{cld} and l_{cld} is harder to calculate, but can be estimated with equation (2.17). An upper and lower limits on these parameters can be established from as follows: For the upper limit we assumed $n_{cld} \propto R^0$ and $l_{cld} \propto R^0$. This distribution of clouds, which was chosen due to its contrast with the disk model in which no occultation occurs, results in a linearly increasing covering factor (equation (3.12)). This R dependence might be too large far from $R = R_{min}$, because the cloud number density must decreases with R (see equation (2.19)), whereas the cloud size might increase, but then it's opacity tends to vanish as it becomes transparent to the higher energy bands. The lower limit is derived by assuming that the equality holds in equation (2.17), a valid assumption when the free-fall velocity is proportional to the accretion velocity. The radial dependence in the first case is then $\chi = 3$, $\iota = 1$, $\delta = 2$ and $\lambda = 0.5 - 1$ and in

the second case $\chi = 4$, $\iota = 3/2$, $\delta = 2.5$ and $\lambda = 0.5 - 1$. The second case results in a logarithmic increase of $f(R)$ in equation (3.12). The parameter λ depends on the local covering factor $f(R)$ and is thus not directly related to χ and ι.

The spectra in figure 3-4 thus fall into an intermediate category. (For spectra with different R dependence see Sivron and Tsuruta 1994) The spectra were calculated by the numerical integrations in equations (3.10) and (3.11). We checked the code with four, ten and one thousand iterations. Less then ten iterations are needed in order to get the same outcoming spectrum. Because the code is randomly placing clouds in 3D space this means that very few clouds are needed per given covering factor for there to be isotropic reprocessing, and it would be hard to find the difference between few and many clouds. The number of clouds is expect to be larger by a factor of $1/\tau_{1cld}$ for clouds with optical depth smaller than 1. The cloud velocity v_{cld} which is uncertain, is assumed to be Keplerian for equation (2.17), an assumption which we will justify in chapter §4, but doppler broadening is not calculated (see Sivron and Tsuruta 1994).

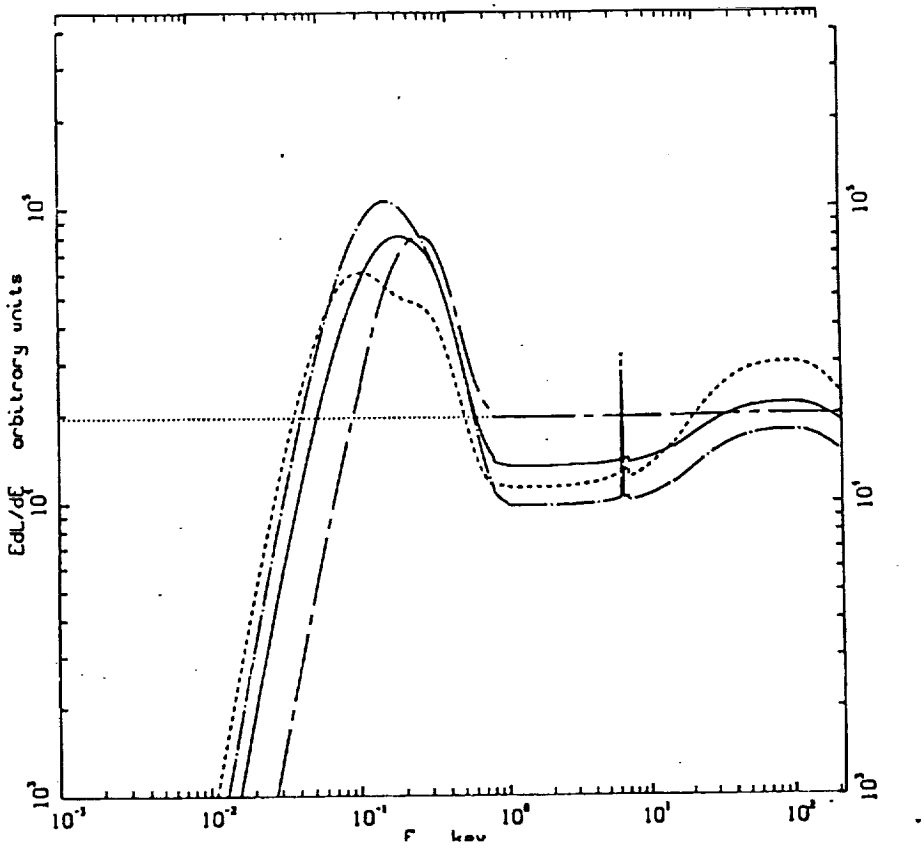

Figure 3.4: The spectra of radiation coming out of a spherical distribution of cool clouds are shown with the solid and dot - dashed curves, for the covering factor $f = 0.5$ and $f = 0.9$ respectively (the one above). The dotted curve is the primary synchro-Compton spectrum. The chain-dashed curve is the spectrum from the innermost region of the central engine where very small CFR cloudlets are present (see the text). The dashed curve is the spectrum coming out of a slab-corona system.

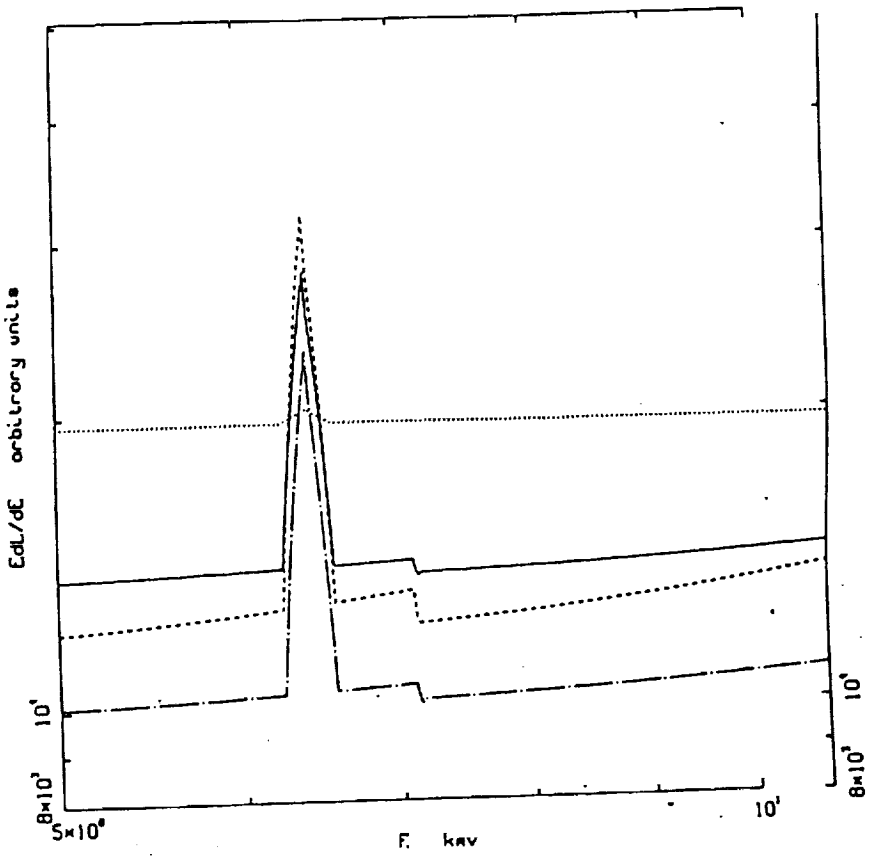

Figure 3.5: The same as figure 3-4, in the intermediate x-ray range. The upper dashed curve is for a covering factor of $f = 0.01$, and the curves below it are for $f = 0.5$ and $f = 0.9$ respectively. One can clearly see the 'flattening' of the power-law spectrum, and the increase in equivalent width with increasing f. Also noticeable is the fact that the edge is disappearing when f is small.

The spectrum in figure 3-4 can fit recent observation of radio quiet AGN. These observations show a power law spectrum with a bump in the EUV - soft X-rays wavebands, an Fe line edge system and a hard X-ray bump, all of which vary from source to source (Mushotzky, Done and Fabian 1993). These results are easily explained by a varying covering factor in the cloud model.

These results, combined with the unabsorbed portion of the input spectrum, can be compared with the slab case, which a simplified version of the disk corona model, where $I_{obs} = 0.5\ I_{in} + S_{ref} + \pi(R^2_{max} - R^2_{min})F_{thermal}$. In figure 3-4 the dashed line is for the slab case. In order to get the same variety1 of spectra the slab must be tilted, as in George and Fabian 1990. A disk has a few spectral features which are inherently different from those of clouds. The UV thermal bump must be broad, with emission that depends on $R^{-3/4}$ (Frank, King and Raine, 1992), whereas in the cloud model the dependence varies from $R^{-1/2}$-R^{-1}. The hard X-ray bump is a result of Compton reflection only, whereas in a more general case of the cloud model some clouds have $\tau < 1$ and a partial covering by a warm absorber should be present (see chapter 7). As seen in figure 3-5, the Fe line in the disk model is very strong (except for very high inclination angles of the disk, as in George and Fabian 1990). In the cloud model it is easy to show that if the Fe line originates in the central engine it may be obscured for

high accretion rates. This result can be compared with the X-ray Baldween relations (Iwasawa et al. 1993), in which higher luminosities were found to be correlated with lower line intensities.

Chapter 4

CENTRAL ENGINE DYNAMICS

In the first section of this chapter the typical timescales for variations of the physical parameters in the central engine are estimated. We show that those timescales result in perturbations in the accreting matter distribution, and the formation of cold and hot components. In the second section we show that perturbations readily form shocks in the central engines of AGN. These shocks are able to reproduce the observed flux and spectrum variability, transfer angular momentum away from the central engine and accelerate particles to high energies.

4.1 TYPICAL TIME SCALES

The dominant processes in the central engine are best determined by the typical timescales. Collisional or radiative process are present if their typical timescales

are shorter than the typical accretion timescale. The processes with the shortest timescales are usually the dominant processes. In this section we try to establish timescales and determine the dominant processes.

4.1.1 Variable Compact Sources

It is impossible to have highly variable homogeneous compact source. Compact sources have very high radiation density which easily accelerate particles to relativistic speeds. When the radiation is dramatically increased, equilibrium densities and pressures are easily perturbed.

The timescale for doubling the output of the central engine is similar to the accretion timescale. If the accretion is homogeneous and the amplitude of variability is large enough, the whole emitting region needs to change its emission in a period of time $t_{emission} \sim R/c$ which is only slightly smaller than the minimum accretion time $t_{acc} \sim (R/c)\sqrt{2r/9}$, where $r = R/R_g$, without changing the matter density distribution.

The timescale for perturbing the original matter density distribution in a compact region is similar to the accretion timescale. One may assume an initial Eddington luminosity, such that the matter is at equilibrium. In such a case the doubling of the luminosity results in the outwards flow of matter on timescales which are similar to

the accretion timescales. Since this timescale is distance dependent the matter closer to the source of radiation is accelerated more than the matter further away, and a shell, or a sheet, of overly dense matter is formed over timescales which are similar to the light crossing timescale. The original homogeneity is therefore easily wiped out.

4.1.2 Formation and Durability of the Cold Matter Clouds

In section 2 of chapter 2 the maximum timescale for the formation of cold clouds from perturbations in the central engines of AGN is estimated. These clouds should persist for a long enough duration so that the effect on the emission is noticeable. We next try to estimate the range of lifetimes of the cold clouds using two methods. The formation and persistence of cold clouds is then shown to be plausible.

The minimum life time of plasma sheets and filaments can be approximated for the case in which a cloud is, for simplicity, represented by a spherical cloud and all of the incident radiation is transformed into an energy increase of size ΔE. Then,

$$t_* \geq \frac{\Delta E}{F} = 140 r^{1/2} \left(\frac{r_*}{c}\right) \left(\frac{kT_*}{\mu m_H c^2}\right), \tag{4.1}$$

where F is the maximum flux incident on the cloud, r_* is the radius and $T_* \sim 10^8$K is the final temperature of the cloud in which all the elements are completely ionized (see also Bond & Matsuoka, 1994). For a cloud of size 10^8cm (obtained for $M \sim 10 M_6$,

using the same arguments as in Celotti, Fabian and Rees 1992, or chapter 2 of this thesis), the life time of the cloud is greater than 10^{-4} seconds. This result is a lower limit, because no radiative losses are considered, in spite of the fact that bound-free and free-free emissions are dominant mechanisms in the creation of the cold component clouds. These clouds have already been proven to be efficiently radiating energy in chapter 2.

The above timescale which describes the final dissipation of a cold cloud is a lower limit. We next try to determine an upper limit on the lifetime of a cloud from the beginning of such a process. We assume that that the temperature decrease is due to adiabatic expansion into vacuum. Since we only have a lower bound on the temperature of the clouds we get an upper limit on the speed of dissipation. We calculate the time-scale for the optical depth to be halved. The following equations govern the adiabatic expansion of clouds. The continuity equation in spherical coordinates, for a spherically symmetric time-dependent case is

$$\frac{\partial \rho}{\partial t} + \frac{1}{r_*^2}\frac{d}{dr_*}(r_*^2 \rho v) = 0, \tag{4.2}$$

where r_* is the radius of the exploding plasma cloud and v is the velocity. The Euler

equation is

$$\frac{dv}{dt} + \frac{1}{\rho}\frac{dP}{dr_*} = 0. \tag{4.3}$$

The adiabatic (energy) equation is

$$P = T^{\gamma/(\gamma-1)}, \tag{4.4}$$

where $\gamma = 5/3$ is roughly the adiabatic index for ideal monoatomic gas, for the mainly Hydrogen plasma. The equation of state is

$$T \sim \frac{m_H P}{\rho k_B}. \tag{4.5}$$

The total mass of a cloud, M_{cld}, is

$$M_{cld} = \frac{4\pi}{3} r_*^3 \rho. \tag{4.6}$$

The optical depth of a cloud, assumed here to be dominated by free-free and bound-free absorption processes is

$$\tau \sim 1.0 \times 10^3 r T^{-1/2} Z^2 \rho^2 \times \left(\frac{h\nu}{keV}\right)^{-3}. \tag{4.7}$$

Through expansion the clouds become more transparent, and their signature on the overall emission diminishes. We are therefore interested in the ratio of the optical depths of the clouds before and after they expand. By substituting equation (4-8)

into (4-7), and than into (4-6) we get $T \propto r^{3-3\gamma}$, which is identical with the result by Zeldovich and Raizer 1967. substituting this result into (4.9) we find:

$$\frac{\tau(r_*(t_0))}{\tau(r_*(t_f))} = \left(\frac{r_*(t_f)}{r_*(t_0)}\right)^6. \tag{4.8}$$

Here r_f is the final size of the expanding cloud. From this we can see that a bremsstrahlung and bound-free dominated, adiabatically expanding cloud will only need to grow by $r_f/r_0 \sim 1.12.$, in order for the optical depth to decrease by a factor 1/2. Substituting an the initial cloud size into equation (4-5) we can estimate the timescale in which a cloud becomes transparent. Since the pressure, density and size change very little when a cloud opacity is halved the Euler equation becomes roughly $d^2r_*/dt^2 \sim -(1/\rho_0)(P(t_0)/r_*(t_0))$ and integrating twice, using the initial conditions $v(t=0) = 0$ and $r_*(t=0) = r_*(0)$, we get

$$t_s \sim (10sec) \times \frac{(r_8)}{T_6^{1/2}}, \tag{4.9}$$

where $r_8 = r_*(0)/10^8$cm, $T_6 = T/10^6$K, and r_0 and P_0 are the initial size and pressure of the dense sheets, and t_s is the time from the beginning of the expansion. Hence, clouds lose their opacity on a time scale of tens of seconds. The life-time can be longer, as a result of confining pressure, due to ambient gas and magnetic fields pressures in it (Rees 1987).

Optically thick, cold plasmas, form if their creation time is longer than the time it takes to radiate the excess energy from the plasmas. In chapter 2 the life time was taken to be the infall time. In a more general case,

$$t_{emission} < t_{contraction} \tag{4.10}$$

Here $t_{emission}$, the typical time scale for emission, includes cooling by creation of pair cascades or thermal pairs, cooling of the post pair-dominated matter by synchro-Compton, bremsstrahlung and free-bound transitions, and thermal emission from matter in local thermal equilibrium. The upper limit for the emission timescale is given by equation (4-1). Assuming the expansion time is of the same order of magnitude as the contraction time, one can calculate the right hand side of equation (4-12) using the expansion timescales t_s or t_*. A minimum cloud size of $l_{cld} \sim 0.01 T_4^{-1}$cm is needed if $t = t_s$, and $l_{cld} \sim 10^9 r^{-1/2} T_7^{-4}$cm if $t = t_*$. For $t = t_s$ $T_7 = T/10^7$ is the maximal temperature for which equation (4.11) may be applicable. This result reaffirms the results obtained by Guilbert and Rees (1988).

4.1.3 Clouds Collisions

Clouds do not collapse to form a thin disk only if they are dense and small. The timescale for collisions therefore determines the geometrical distribution of clouds.

Numerous small and dense clouds may be spherically distributed, whereas large diffuse clouds may coalesce and form disks.

The first simplified approach for calculating the timescale for collisions is presented in chapter 2, and is elaborated upon here. In figure 3-3 an ensemble of clouds and sheets was presented, to which random motions can be added with an overall average angular momentum, with $\omega R << v_{avg}$, where ω is the angular velocity and v_{avg} is the random speed. The velocity field of inhomogeneities is affected by the gravitational and radiative fields, drag by the hot phase, and interactions with other inhomogeneities. The average speeds in the case of few inhomogeneities rapidly approach Keplerian speeds. Collision between two cold clouds results in the loss of some random motion, whereas the overall angular momentum is conserved, and the orbit thus becomes more axisymmetric. If the inhomogeneities are not compact the matter settles onto an accretion disk. A very stringent upper limit on the number density and size of the clouds is therefore found from this argument to be

$$n_{cld} l_{cld}^2 < \left(\frac{v_{cld}}{v_{acc}}\right)^{-1} (\pi R)^{-1} . \tag{4.11}$$

Here, unlike equation (2-17), the accretion velocity is not assumed to be proportional to v_{ff}. One may assume, for example, an initial distribution of clouds which are held at equilibrium (held by radiative pressure, for example), except for one cloud that is

only affected by gravity and elastic collisions with identical clouds on the same radial line. The result of this may be a 'domino effect', in which each cloud transfers all of its linear momentum to the cloud next to it, and one gets an equation of motion for the radial component $2v_{avg}/\Delta t_{dom} = GM/R^2$, where v_{avg} is the average velocity between collisions and Δt_{dom} is the time between cloud collision in the radial direction. This timescale is smaller than $\Delta t_{coll} = 1/(n_{cld}\pi l_{cld}^2 v_{avg})$, the time between cloud collisions in random motion. Comparing these timescales one gets $n_{cld}l_{cld}^2 < 1/(2\pi R)$, which is a stronger limit on the product of cloud density and size than equation (2-17).

4.1.4 Explanations of Low Amplitude Spectral Variability

We next show that the lack of simultaneous variability in the IR-optical and the X-ray parts of the spectrum does not imply that the synchro-Compton model for the central engine fails. In order to show this we establish a relation between the temperature of central engine opaque component and the timescale of variability.

Consider a source in which the amplitude variability is very large in one wave band, which includes a significant portion of the total emission. When in certain shorter wavelengths the flux variability of time scale Δt_{long} has small amplitude $\Delta L/\Delta t$ one of two things may be the cause: 1. The source of luminosity in that wave band is from a region far from the central engine, such that the light crossing time (equation

2.1 in chapter 2) is much larger than Δt_{long}. 2. The emitting matter has a very high 'heat capacity', such that the energy input from the highly variable central engine is reemitted over a large timespan. The mechanism for such 'smearing' of the variability is described below for the case of opaque clouds.

For the cloud model a 'turn-off' of the central X-ray emitting source results in cloud cooling over thermal time scales. The thermal time scale is derived from $dE/dt = -4\pi l_{cld}^2 \sigma_B T_{cld}^4$ where E is the total energy of one cloud and $\sigma_B = 5.65 \times 10^{-5}$erg cm^2 K^{-4}, and $T_{cld}(E)$ is found from the ideal gas law. σ_B is the Boltzman constant. Solving the above equation we get

$$t_c > \frac{10^4}{T_4^3} sec, \tag{4.12}$$

for Seyfert nuclei, e.g. NGC 4051 (Sivron and Tsuruta 1993). For instance, for very soft X-rays at 10^6K $t_c \sim 0.01$ sec, while it is nearly a year for the UV radiation at 1000 K. Consequently with our model, while the high energy end of the bump should vary almost simultaneously with the harder X-rays, similar rapid variations are not expected at the low energy end of the bump lying in the UV band.

We examined carefully the temporal behavior of the NGC 4051 spectrum near the optical B-band (Done *et al.* 1991) which shows no rapid variability during the X-ray flares, and find that the low energy end of the UV bump already appears at this

waveband. The lack of rapid variability at these wavelengths is consistent with the two component cloud model with no CFR cloudlets if $f(R_{max}) > 1$. This observation is consistent with the cloud model with $f(R_{max}) < 1$ if there are CFR cloudlets in the central engine, or if the continuum emission mechanism has no inherent IR-UV emission (for example, Comptonization of UV photons with relativistic electrons or pairs).

4.2 SHOCKS IN THE CENTRAL ENGINE

Shocks form readily in the central engines of AGN. Shocks are shown to form when a star is captured into the central engine, or directly, from strong and large density perturbations. If the shocks persist for a long enough period they are shown to significantly modify the emission from the central engine. Shocks also provide the necessary mechanism for the outward transfer of angular momentum which enables the accretion of matter onto the SMBH.

4.2.1 Introduction to Shocks

Using recent X-ray observations it was shown that a large fraction of the high energy luminosity is emitted by hot ($T_e > 10^9$K) plasmas (Blandford 1990, Mushotzky, Done and Pounds 1993, Svennson and Zdziarsky 1994). In order to explain the in-

creased emission from these plasmas a triggering mechanism should be devised in which a small perturbation can generate radiation from a large enough volume. The effect of the perturbation on the hot plasmas within this volume double its' radiative output, in some cases.

The largest speed in which perturbations can propagate is of the order of the speed of sound or the Alfven speed in the hot plasmas. Perturbations that are large enough to result in significant changes in emission are easier to produce by shocks than with regular compression waves. We therefore look for a mechanism that results in shocks. One should check that shocks indeed form under the conditions anticipated in the central engine, which we do in section 4.2.2. We show that shocks form in the central engines of AGN. We discuss what happens when a local cold inhomogeneity, such as a cloud, or a main sequence star, makes its way into the innermost region of AGN. We have to show that such an incident naturally results in the creation of a strong shock that may modify the emission from the continuum source, the hot plasma. We have chosen a main sequence star for two reasons. The first is that the capturing of such a star is a plausible event (Syer Clark and Rees 1990), and the second is that an analytic solution is possible when the lifetime of the inhomogeneity is long, as in the case of a star. We also discuss the consequences that the shock might have on

the accreting matter and the star. A more direct approach, in which a non-linear perturbation results in a shock wave, is calculated in our next paper (Sivron and Tsuruta 1995).

Finally we have to show that a relatively small inhomogeneity significantly modifies the light-curve from an X-ray region of at least an order of magnitude larger surface area. The creation, destruction and properties of the emission modifying matter are treated in section 4.2.3 The resultant flux variability is shown to be significant in section 4.2.4 A simplified geometrical model used to calculate a typical light-curve is presented in section 4.2.5. The problem of angular momentum transfer is treated in section 4.2.6. Shocks, turbulence and magnetic reconnections are probably the primary mechanisms in AGN for the creation of cold clouds, as is further discussed in chapter 7.

4.2.2 Shock Formation and Its Consequences

We next show that the velocity of a macroscopic inhomogeneity exceed the speed of sound and/or the Alfven speed when captured into the hot plasma in the inner region of an AGN. A shock wave, which always forms when matter supersonically flows past a body (Landau and Lifshitz 1987, hereafter referred to as LL87), forms near the inhomogeneity. A collisionless shock will form if the Alfven speed is exceeded.

Theory predicts (Shapiro Lightman and Eardley 1976, Rees et al. 1982, Blandford 1990) that the thin accretion disk will be disrupted within a critical radius, which may be as small as $r_{cr} \sim 10\dot{M}_{23}^{2/3} M_6^{-2/3} \alpha^{1/3}$, or as large as $r_{cr} = m_p/me$, where α is the parameter defined in the 'standard α disk' model, which relates the pressure and shear stress. Within r_{cr} heating due to gravitational and viscous energy release surpasses cooling by bremsstrahlung and black-body radiation, the temperature rises and the gas pressure inflates the disk. The accretion flow inside this radius will therefore form a geometrically thick torus, which will become a two temperature optically thin plasma for rates below the critical rate $\dot{m}_{cr} \sim 50\alpha^2$ (Rees et al. 1982). Even at higher accretion rates a two temperature state may ensue (White and Lightman 1990), which is not necessarily stable (Begelman, Sikora and Rees 1987, White and Lightman 1990). We hereafter concentrate on the optically thin two temperature plasma, and use the equations of Shapiro Lightman and Eardley 1976 and White and Lightman 1990. The thermodynamic parameters, such as the adiabatic constant Γ_a, are taken from a paper on shocks in pair-rich plasmas (Iwamoto 1989, hereafter referred to as I89 and references therein). Although the I89 equations, which are for matter in LTE, may be over-simplified for parts of the central engines of AGN, the results are expected to be qualitatively correct.

The speed of sound at a distance $r < r_{cr}$ from the black hole is:

$$c_s = \sqrt{\frac{\Gamma_a p}{\omega}}, \tag{4.13}$$

where p is the pressure in the accreting gas, and ω is the enthalpy (the I89 equation A18a). The pressure is dominated by the ion thermal energy, and the equilibrium temperature does not quite reach its virial value if the outwards transfer of angular momentum is dissipative. (This is because of a combination of inverse Compton scattering and bremsstrahlung in mild pair plasmas, synchro-Compton cooling in strong magnetic fields, or some collective plasma effects, such as those created by shocks.) The ion temperature is thus

$$T_i = a\, T_v, \tag{4.14}$$

with $a \sim< 1$ and $T_v = m_p c^2/(k_B r)$ is the virial temperature. The ideal gas law, which holds for optically thin gasses at high temperatures (I89 eq. A8), is a reasonable approximation for the equation of state. The speed of sound is therefore

$$\begin{aligned} c_s &= \sqrt{\frac{\Gamma_a k_B T_i}{\mu m_H}} \\ &= \left[\frac{a\Gamma_a}{\mu r}\right]^{1/2} c \end{aligned} \tag{4.15}$$

where m_H is the mass of the hydrogen atom and for cosmic abundance $\mu \sim 1$.

An inhomogeneity, which is more compact than the surrounding material, so that it cannot lose its angular momentum on dynamical time-scales (see sections 4.1.2 and 4.1.3), moves at a speed comparable to its Keplerian or free fall velocity, both of which are usually larger than the speed of sound:

$$v_* = |\mathbf{v}_* - \mathbf{v}_{fl}| = b\, r^{-1/2} c. \tag{4.16}$$

Here $\mathbf{v}_*$ is the velocity of the inhomogeneity and $\mathbf{v}_{fl}$ is the velocity of the accreting matter. The Mach number

$$\mathcal{M} = \frac{v_*}{c_s} = b\sqrt{\frac{\mu}{a\Gamma_a}} \tag{4.17}$$

does not depend on the distance from the SMBH, because both speed of sound and typical velocity are proportional to the virial energy. For $b \sim 5/4$ the Mach number is larger then 1, and a shock forms. Because a is not much smaller than 1 for a wide range of accretion rates (see WL90) $\mathcal{M}$ is not larger than ~ 10, and a shock, rather than tube, form. The Mach surface opening angle, $\phi \sim 2\arcsin(c_s/v_K)$, is therefore significant. The shocked surface so created roughly takes a conical shape. Higher accretion rates will make Γ closer to its radiation dominated value of 4/3, which makes shocks possible even in the cases of near virial temperatures and average

inhomogeneity velocity.

The creation of strong shocks by large enough inhomogeneities in the central engines of AGN is inevitable for a large range of accretion and dynamical parameters. These inhomogeneities can be stars, but may also be cold plasma sheets and filaments, that accelerate to supersonic velocities if the gravitational force, the radiation pressure or the (virial) magnetic stresses are greater then the drag force

$$\frac{GMm_*}{R^2} \geq \pi D_*^2 p_0, \tag{4.18}$$

where p_0 is the pressure on the inhomogeneity surface (see section 4.2.3). We assumed that the radiative force or the magnetic stresses are of the same order of magnitude as the gravitational force (see also chapter 2). Noting that the pressure is roughly $p_0 \sim \rho_g v_K^2$ (see section 4.2.3) this condition can be also written in the form:

$$\frac{\rho_*}{\rho_g} \geq \frac{R}{D_*}\left(\frac{a\Gamma_a}{\mu}\right), \tag{4.19}$$

where ρ_* is the average density of the inhomogeneity. This condition, which is fulfilled for inhomogeneities which are confined by virial magnetic fields (see Guilbert and Rees 1988, Sivron and Tsuruta 1993, and Celotti, Fabian and Rees 1992), may be less restrictive if we include acceleration by radiation. If confined by virial magnetic fields the inhomogeneities may be as small as $D_*/R_X = 10^{-4}$, two orders of magnitude

smaller than an orbiting star. The amplitude of perturbations in the density needed for shocks to form is therefore small, and shocks may form in the wake of large amplitude compression waves in the disk. These waves are probably non-axisymmetric (see section 4.2.6).

It is easier to calculate the resultant shocks for inhomogeneities with lifetime which is much longer than the dynamical timescales, such as stars. It has been shown that a star can be captured into a tightly bound orbit around a black hole through repeated interactions with a thin disk around the hole (Syer Clarke and Rees 1990), and that the probability of such an event in AGN is even higher for stars in bound orbits (Pineault and Landry 1994). Once captured the orbit will be circularized and eventually the star will be "grounded down" into the disk plane through repeated interactions with the disk. The timescale for circularization can be shorter than that for planarization, which may happen very close to the central source. Therefore, in our model, we assume that the orbit of the captured star has been circularized, whereas the orbital plane is still inclined to the disk plane. This situation is expected for a wide range of the original relative inclination angles of these planes.

The extent and magnitude of the shock depend on the size of the star, and so does the stability of the orbit. For example, for a similar orbital velocity a smaller star

produces weaker shocks than a larger star, the drag force is smaller, and the decay of the orbit is slower. To avoid rapid disruption the size of the star that has migrated into the innermost region cannot be much larger than its Roche lobe. The mass of a regular main sequence star is therefore limited to

$$m_* < 0.3 M_\odot \tag{4.20}$$

(King & Done 1993). The radius of the star may therefore be expressed in units of $d_{10} = D_*/10^{10}$, and its mass is in units of the solar mass $M_\odot$.

In most cases the generalized hydromagnetic speed of sound, $(c_s^* O)^2 = c_s^2 + v_A^2$, where $v_A = \sqrt{B^2/(8\pi\rho)}$ is the Alfven velocity and B is the magnetic field, is similar to the hydrodynamic speed of sound (equation (....)). The main effect that magnetic fields have is reducing the shock thickness:

$$\delta \sim \frac{2}{\sigma}\left(\frac{c}{4\pi}\right)^2 \frac{B_{1-2}^2}{\rho v_*^3}, \tag{4.21}$$

where $\sigma \sim ne^2 t_C/m_e$, t_C is the ion-electron collision timescale and B_{1-2} is the magnetic field variance across the shock. The smallest possible shock width is the Larmour radius, which for ions is $r_{Li} = AT^{1/2}/ZB \sim 10^6 T_{12}^{1/2}/B\mathrm{cm}$ where Am_p is the mass of an ion and Z is its charge. It is evident that even magnetic fields which are much smaller than the virial value (about 10^3 Gauss in the central engine, see Blandford

1990) limit the thickness of shocks.

Although the speed of sound in The extent and magnitude of the regular supersonic shocks depend on the size of the perturbation and the density of the perturbed matter, and in the case of AGN intermediate and high accretion rates make creation of significant shocks possible only in the inner $10R_G$. In that region the mean free path in the surrounding gas is smaller than the size of the inhomogeneities. However, if the accretion is not super Eddington, collisionless shocks form throughout the central engine, because the Alfven speed is usually much smaller than the speed of sound.

The Alfven wave speed in plasmas is roughly $C_A = \sqrt{B^2/8\pi n_s m_s}$, where the subscript s is for electrons or ions. Super Alfven speeds are therefore achieved if

$$\mathcal{M}_A = \left(\frac{v_*}{C_A}\right) \tag{4.22}$$

$$= \left(\frac{R}{10R_G}\right)^{-1/2} n_{10}^{1/2} \frac{1}{B_3} \left(\frac{m_s}{M_H}\right)^{1/2} \tag{4.23}$$

is larger than 1. Here $n_{10} = n_s/10^{10}$and $B_3 = B/10^3$. For the central engine one expects B fields of order 10^{3-4}gauss or smaller (Blandford 1990). It is apparent that the Alfven speeds are exceeded in most cases. Large magnetic fields and small

densities may be present in radio loud AGN. In such cases the ordered structure of the accretion disk is not perturbed by shocks, and advection, magnetized disks and jets may be possible. For higher accretion rates diffusion of magnetic fields out of the plasma and reconnection events may restrict the magnitude of these fields. We therefore expect that for near-Eddington accretion rates the magnetic fields are smaller than 10^3gauss, and collisionless and magnetic shocks form.

4.2.3 Radiation From the Shocked Matter

We show that the when the power transferred from the star to the shocked matter is emitted as radiation the light curve is modified. We then show that its highly probable that the shocked matter indeed radiates the power transferred from the star.

The power transferred from the star to the shock is at least

$$P_{sts} \sim (A_* p_0) \times v_*, \tag{4.24}$$

where $A_* = \pi D_*^2$ is the cross section area of the star and p_0 is the pressure near the stellar surface, behind the shock. The pressure on the star surface, p_0, is modified from the treatment of formation of shocks in supersonic non-relativistic flows past solids of revolution (LL87, §122). In our case the object is a sphere, the orbiting star.

The pressure near the stellar surface is thus related to the ambient matter velocity, density and speed of sound through

$$p_0 = p_1 \left(\frac{\Gamma_a + 1}{2}\right)^{(\Gamma_a+1)/(\Gamma_a-1)} \frac{\mathcal{M}^2}{[\Gamma_a - (\Gamma_a - 1)/2\mathcal{M}^2]^{1/(\Gamma_a-1)}} \tag{4.25}$$

$$\geq 1.5\rho_g v_*^2 \frac{1}{[1 - 1/(5\mathcal{M}^2)]^{1.5}},$$

where $\rho_g = \dot{M}/(\Omega R^2 v_{acc})$ for semi - spherical accretion, Ω is the solid angle and v_{acc} is the accretion velocity. If the parametric dependence of the density is less distance-dependent (see, for example, WL90) the pressure is even higher at larger radii. The adiabatic constant Γ was chosen to be at it's highest value of 5/3, which results in a lower limit on p_0. We have used the Ranking-Hugoniot relations for relativistic plasmas in thermal equilibrium (Iwamoto 1989). For collisionless shocks the minimum pressure on the stellar surface is $p_0 = B^2/4\pi$.

The power transferred from the star to the shock is thus at least

$$P_{sts} \sim (10^{41} ergs\ sec^{-1}) b^3\ d_{10}^2 \dot{M}_{23} M_6^{-2} r^{-3}. \tag{4.26}$$

If all this power is radiated the radiation emitted is quite large. This radiation may be smaller than the X-ray luminosity observed (table 1), but it may still modify the light curve and spectrum. We also note that relativistic effects, secondary shocks (see

section 4.2.4) and the effects of short living larger inhomogeneities are not taken into account. The modification of the emission through a single radiative shock may occur only in the innermost $10R_g$, as is anticipated (but not calculated) by previous authors that discussed pair modifications of the inner torus with the injection of a power-law distribution of relativistic electrons. (See Blandford 1990, White and Lightman 1990, Tritz and Tsuruta 1989, Kusunose and Takahara 1989, Kusunose et al. 1995. These authors mistakingly assumed strong shocks exist in the central engine by a-priory postulating geometrically thin, optically thick Keplerian accretion disk. In such disks the speed of sound is much smaller than that calculated in equation (4.12), but these disks are not necessarily stable.)

To show that the power transferred to the shock is indeed radiated one needs to look at the Ranking-Hugoniot relations away from the star. The increased densities, temperatures and particle number densities in the post-shock region must be large enough so that the timescale for radiative processes is smaller than the timescale for the dissipation of these quantities. For strong MHD shocks the mean free path for a particle in the post-shock region is approximately the shock width $\lambda_{sw} \sim 10^{11} n_{13}^{-1}$cm (see standard plasma texts such as Boyd and Sanderson 1968), which means that the radiative cooling timescale must be shorter than the $\lambda_{sw}/v_* \sim 100 n_{13}^{-1} r^{1/2}$ seconds in

which the matter passes in the post-shock region. In Guilbert and Rees (1988) and Ferland and Rees (1988) the cooling of a slightly compressed region in the central engine down to LTE temperatures by bremsstrahlung and synchro-Compton radiation was calculated to be possible for a region which is two orders of magnitude larger. Their calculation therefore assumed the average densities which were calculated in chapter 1.

In order to calculate the Ranking-Hugoniot relations in the shock we assumed thermal two temperature plasmas. This is a reasonable assumption for high accretion rates and moderate magnetic fields. This kind of formalism was developed by Iwamoto (1989) for plasmas near pair-creation temperatures, which is appropriate for the central engines of AGN. Using this formalism for the post-shock region the density is calculated from the Ranking-Hugoniot relations to be of order $7\rho_g$. The post-shock ion temperatures, including energy deposited into pairs created in the shock, are of order $10T_i$ for the central engine conditions of table 1. The synchro-Compton cooling (and pair cooling for high compactness sources) time is roughly shortened by at least $t_{sw}/t_{GR} \sim (\gamma_{GR}/7\gamma_{ps})^2$ where the subscripts GR stand for the Guilbert and Rees result. The timescale t_{sw} is the time for cooling in the shock. The factor 1/7 comes from the increased post-shock density effects on the synchrotron and Comptonized

radiation. The temperature of a shocked particle $T \propto KE \sim mc^2(\gamma_L - 1)$ implies that the Lorenz factor for the average downstream particle, γ_{ps}, is roughly an order of magnitude larger than the upstream γ_{GR}. It is thus evident that strong shocks can result in cooling timescales that are shorter than the typical crossing time of the shocks. The matter that was cooled by synchro-Compton processes can be further cooled by bremsstrahlung radiation. The timescale of cooling by bremsstrahlung is proportional to the square of the density, and is therefore much shorter than the time for reheating by radiation (see chapter 2). This cool matter is probably sheared and fragmented in the rarefaction region behind the shock. We see that not only does the post-shock matter can radiate most of the energy transferred from the star to the shock, but also post shock thermal (and possibly opaque) Guilbert and Rees 'cold' matter may forms.

In the above treatment we assumed that the magnetic field is perpendicular to the shock front and is unchanged in the shock. In such cases the shock thickness δ equals the mean free path of the ions (or the deflection radius) rather than the much smaller Larmour radius in the magnetic field.

In order for the power from the star to be given to radiation from the hot shocked matter the mean free path must be small enough. In the case of collision shocks the

mean free path is larger than the star, and smaller than the emitting region. In such cases shocks are inefficient. However we argue that magnetic fields can be rid off only to the level at which they are reconnected in reconnection events, such as in shocks. Since magnetic fields can be refracted and changed by shocks current sheets and DC fields can form. These can be the sight of reconnection events. If such is the case one expects that the leftover magnetic fields are enough for Larmour radiuses which are as wide as the typical inhomogeneity, which we assumed to be of order 10^{10}cm. The timescale for cooling is still enough, because the magnetic fields are increased by the compression ratio $r_C = \rho_2/\rho_1 \sim 7$.

The preferred shock thickness is therefore much smaller than the mean free path. Indeed it may be as small as the Larmour radius of an ion in the field. The case of collisionless shocks, which are expected in AGN for low accretion rates, is slightly more complicated because of the supposedly small shock front width and the increased importance of Fermi-shock processes, and because of the breakdown of the thermal plasma approximation (see Sivron and Tsuruta 1995).

The shock induced modifications of the emission from the central engine may result in a flare of softer than synchrotron X-ray spectrum, i.e. $0.5 < \mathcal{A} < 1$, where $\mathcal{A}$ is the slope of the continuum emission spectrum, because of the increased local

compactness (see, for example, Ghisellini and Haardt 1994, Grandi, Done and Urry 1994, and references therein), or because of the spectrum from reconnection events. Temporary increase in the brightness of an inhomogeneity could also be a result of lensing of the shock radiation near a Kerr black-hole (Blandford and Nárayan 1993, Rauch and Blandford, 1993).

Significant amounts of radiation from the shock front will also be observed if more efficient non-thermal pair cooling is present. Such cooling will result, for example, if the Fermi acceleration is very efficient (Blandford and Eichler, 1987, show that electrons heating by interaction with Alfven waves is limited, but relativistic pairs from various pair-creation events can efficiently cool the post shock matter by synchro-Compton and bremsstrahlung processes).

4.2.4 Effects of Post-Shock Matter on Radiation

If P_{sts} is expended on the cooling of the post-shock matter, that cool component may modify the emission by absorption in a post-shock sheet behind the Mach surface. We next show that the power needed to cool a large enough sheet is smaller than P_{sts}.

The X-ray continuum source, usually assumed to be $\sim 10R_g$ in radius,

$$R_X \sim (1.5 \times 10^{12} cm) M_6, \tag{4.27}$$

should be covered by a large enough sheet of area larger than about πR_X^2. The continuum region can be obscured if the absorption column through this sheet is larger than $N_H \sim 10^{20-24}\mathrm{cm}^{-2}$, where the lower number is for bound-free absorption in cold (the ionization parameter $\Xi_0 = 0$) cosmic abundance matter in which some features, such as an oxygen and iron K edges and lines may show up, and the higher number is for electron scattering. The sheet thus created must therefore be made out of at least $N_H \pi R_X^2 = 7 \times 10^{44-48} M_6^2$ particles.

In order that pair cascades will efficiently cool enough of the ambient matter the energy per particle, $\epsilon \sim (3/2) k_B T_2$ should be $\sim 10 m_e c^2$ (see, for example, Svennson 1984, Lightman 1982), where T_2 is the post shock matter temperature. The product of the rate at which particles are cooled and the life time of the post-shock cooled matter should be larger than N_H. (The life time of a cloud, t_s, is calculated in the Appendix.) The power of the shock therefore supplies enough energy per particle for cooling to take place

$$\begin{aligned} \epsilon &\geq \frac{P_{sts} t_s}{N_H \pi R_X^2} \\ &= (0.1 - 1000) m_e c^2 \frac{t_s}{10} d_{10}^2 M_6^{-4} \dot{M}_{23} r^{-3}. \end{aligned} \tag{4.28}$$

(The above quantity is similar to the 'compactness', $l = L\sigma_T/(Rm_e c^3)$, which was defined by Guilbert Fabian and Rees 1983, where σ_T is the Thompson cross section. One may thus think of shocks as an efficient mechanism for the local amplification of the compactness.) If we consider the synchrotron power P_{syn} in equation 4.25 instead of P_{sts} we will still get large enough energy per particle if the post shock magnetic fields are increased by a factor, as is expected in collisionless shocks.

Cold matter which is optically thick in soft X-rays may therefore exist in regions which are inside the thick disk if the inhomogeneity is as large as a star. (It is much more likely, though, that this matter will be 'warm', i.e. partially ionized by the stronger radiation from the central disk and from the nearby shock.) In the case of nonthermal pair cascade the existence of this matter is even more plausible. This cooled matter can be the same as the 'cold phase matter' suggested by Guilbert and Rees 1988 (hereafter referred to as GR88), and may take a spiral shape (see discussion in section §5). We note that modifications due to Fermi acceleration, will probably lower the efficiency of cooling while enhancing particle acceleration for the higher energies in equation (11) (Blandford and Eichler 1987, Levinson 1994).

4.2.5 The Effects of Shocks on the Overall Flux Variability

Our result for the minimum power transferred by the star to the shock may be

used for the purpose of finding an overall flux variability. The simplest scenario is thus a slow introduction of 'stars' of different sizes (see also section .... for details on the source for such 'stars') into the central engine with no angular momentum. The flux from each such event is $P_{sts}t_{in}$ which can be written in the form

$$L_i = (3 \times 10^{42} ergs) b^3 d_{10}^2 \dot{M}_{23} M_6^{-2} r^{-3} \left(\frac{r_{12}}{c}\right), \tag{4.29}$$

where r_{12} is the distance from the SMBH in units of 10^{12}cm. A random introduction of cold inhomogeneities with random distribution of Areas $A = 10^{20}\pi d_{10}^2$ naturally results in shot noise, providing that the events are not correlated.

When the accretion rate is higher the events are correlated, for example, by means of radiative pressure and radiative transfer. The speed of the infalling cold inhomogeneity is reduced, lowering P_{sts}, while the life time is reduced because of heating which speeds the initially adiabatic expansion, thus reducing the length of period of the event, and limiting the amplitude of variation. This scenario is similar to self organized criticality in phase transition physics (Bak et al. 1989). The power spectrum from such an event is expected to be a chaotic in nature, i.e. the slope of the power spectrum will reach -1.

4.3 OCCULTATION BY POST-SHOCK MATTER

In this section we calculate the effect of an optically thick sheet behind a shock on the light-curve. The main purpose of this exercise is to demonstrate the type of spectral variability to be expected when shocked matter modifies the emission from the central continuum source. Our approach is geometrical in nature. In our model the body obscuring the source is not circular. We treat the cases in which a triangular shock front eclipses a circular or a square continuum source.

Possible picture of what happens near the central region of an AGN with an inhomogeneity is shown in Figure 4-1, in which we see the shock inducing star (or spherical inhomogeneity), at point S, orbiting inside the thick accretion disk outside the X-ray continuum region, but confined to a region smaller than the thin disk. From an observer's point of view the points A, S and B on the Mach cone form a 'fan' in the shape of a triangle that partially obscures the internal continuum source. The type of occultation depends on the optical depth of the matter on and near the shocked surface. Emission from the shock surface may dominate the light curve in some configurations.

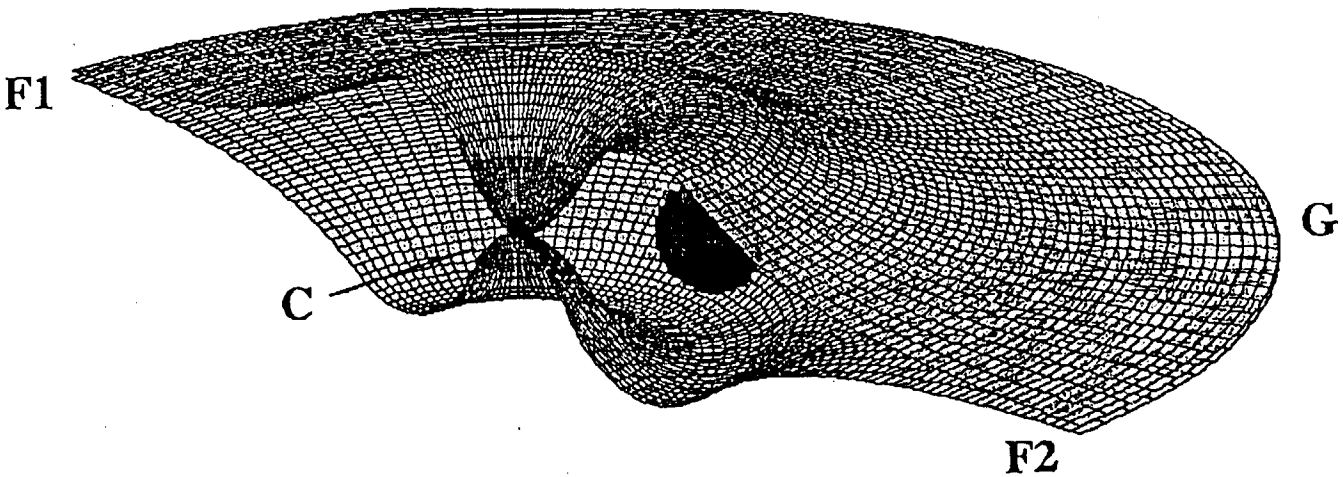

Figure 4.1: The doughnut shape ion-torus is shown here consists of the inner part of the thin disk (at points F1 and F2), the central super massive black hole (SMBH, at point C) and the continuum X-ray source (shaded in gray, near the SMBH). The rest of the ion-torus is filled with optically thin two-temperature plasma. Inside the torus a star orbits, and shocks the two-temperature plasma. Behind the surface of the 'Mach-cone' optically thick matter forms, which obscures the continuum region when in the line of sight. The obscuration is most effective if the observer is in the direction of point G.

Since the extent of the optically thick shock may be limited, as was shown in a previous section, we choose the point of view of an observer in direction G (Figure 1a. and 1c.), which requires the shortest extent of optically thick matter. Figure 1b. is applicable only when the shock effects extend far enough from the star.

Figure 4-2 is a simplification of the view from the direction of point G which is used for the calculation of the light curve. It is based on the following assumptions:

1. The continuum X-ray emitting region is assumed to be circular, with homogeneous surface brightness, as viewed when unocculted. Its radius is $R = R_X$. We note that in an alternative model, in which the soft X-ray region is larger than the hard X-ray region, the soft minimum flux will be significantly delayed with respect to the hard flux.

2. The Mach surface is assumed to be an equilateral triangle, passing across the center of the circular source. That is how a conical surface looks to an observer in a direction perpendicular to its altitude.

3. Density variations are simplified by assuming three density regions: in region 1 (angles smaller than ϕ_1) the matter is opaque to both hard and soft X-rays. In region 2, with angles between ϕ_1 and ϕ, the matter is transparent to hard X-rays, but opaque to soft X-rays. In region 3 the density of matter varies with distance,

due to the spread of matter, and is partially transparent. We consider only the hard X-ray wave-band in the 10–20 keV window in which no absorption is expected, and the soft X-ray wave-band in the 0.5–2 keV window in which absorption due to cold or warm oxygen is expected. We chose the maximum covering factor to be $f = 0.5$ for demonstrative purposes.

In Figure 4-3 we see the light curves near a dip in the two energy bands that will be observed when the source is eclipsed by the post-shock matter. The softer (dashed dotted) and the harder (solid curve) X-ray windows with $\phi = 45^0$. The dotted curve is for the case of a smaller Mach surface opening angle of $\phi = 30^0$, for the hard X-rays. The dashed curve is for the simplified case in which a triangle with an opening angle $\phi = 45^0$ eclipses a square source. In all cases the maximum covering factor is $f = 0.5$.

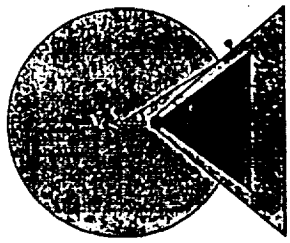

Figure 4.2: An observer's view of the AGN in our model with covering factor of $f = 0.5$. This is a simplified form of the view from point G in Figure 1. The stepwise fashion which was chosen to describe the absorber is for demonstration purposes. See section §4 for details

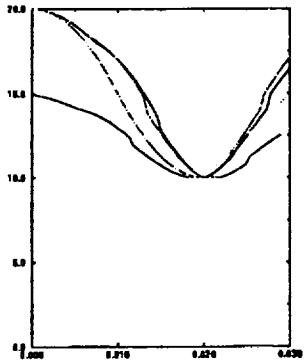

Figure 4.3: The light curves near a dip that will be observed when the source is eclipsed by the post-shock matter is shown for the softer (dashed dotted) and the harder (solid curve) X-ray windows with $\phi = 45^0$. The dotted curve is for the case of a smaller Mach surface opening angle of $\phi = 30^0$, for the hard X-rays. The dashed curve is for the simplified case in which a triangle with an opening angle $\phi = 45^0$ eclipses a square source. In all cases the maximum covering factor is $f = 0.5$ (See section §4 for details).

The decrease of flux toward the dip is energy dependent. A delay is observed in the sense that the decrease in photon count in higher energies lags the decrease in the lower energies. The light curve in the hardest window is chosen to have a cusp–like shape, dropping to half its value at the bottom so that the size of the central sector of absorbing material within ϕ_1 which is opaque to the harder X-rays is approximately half the size of the harder X-ray source size during maximal occultation. The maximum value for R_X is thus obtained with $\phi_1 = \pi/4$. A similar method is used for the simpler geometrical model. It is therefore speculated that the spectral variability observed in AGN may be with time scales which are related to the distance of post shock matter from the central continuum source.

4.4 TRANSFER OF ANGULAR MOMENTUM

In AGN shocks seem to be an efficient mechanism for cooling (but shocks in standard thin disks cannot self consistently explain the high-energy spectrum, see Chakrabarti and Wiita 1992 and references therein). The amplitude of perturbations needed for shocks to form is therefore rather small, and shocks may form in the wake of large amplitude non-axisymmetric waves in the disk.

Shocks may thus be also an efficient mechanism for the transfer of angular momen-

tum: Spiral shocks may form when a massive companion perturbs the disk (Morfill, Spruit and Levy, 1993, and references therein, in reference to galactic sources). Such companion cluster which was predicted to exist near AGN (Rees 1990 and references therein), was recently observed in M31 by the Hubble Space Telescope (HST) (Pei et al. 1994). Such shocks are considered to be an efficient mechanism for the outwards transfer of angular momentum in the case of galactic and proto-stellar disks when the mach number is not too large ($\mathcal{M} < 10$, Savonije, Papaloizou and Lin, 1994, Morfill, Spruit and Levy, 1993). This possibility should probably be reconsidered for AGN due to the HST observation of a spiral structure in M87 (Ford et al. 1994). It must be noted, however, that spiral shocks will result in non-chaotic X-ray temporal variability in low accretion rate AGN, that may be revealed by long exposures observations by X-ray telescopes such as Rosat, Asca, XTE, XMM and especially AXAF. The angular momentum transfer in the central engine in high accretion Seyfert 1 galaxies and radio quiet quasars can be due to chaotic, rather than spiral, shock structure. (In these sources temporal variability is already known to be nearly chaotic.)

A comprehensive study of the transfer of angular momentum in the outer disks (Caditz, Sivron and Tsuruta 1995) and central engines (Sivron, Caditz and Tsuruta 1995) with shocks is currently under way.

Chapter 5

OBSERVATIONAL METHODS

In this chapter we describe some observational methods in X-ray astronomy. Since we are interested in the analysis of data from X-ray satellites we emphasize the possible systematic and random errors in the instruments on board the satellites. The observation of weak X-ray sources, such as AGN, also requires the development of careful methods for the analysis of the data. We describe those methods for the Ginga and ROSAT satellites.

5.1 X-RAY DETECTORS IN ASTRONOMY

In this section we describe the physics of the proportional counter, the 'work horse' of X-ray astronomy. By understanding proportional counters one can understand most of the errors and background subtraction in X-ray data. (In this thesis only data from proportional counters is analyzed. Other X-ray detectors and techniques

are described in Fraser 1988.) A brief description of the detection of X-rays is outlined.

X-rays in the range 0.1 – 20keV entering a detector are absorbed by electrons in the innermost shell of an atom with high enough Z. Atoms with large enough Z have binding energies in the X-ray range for their innermost shells. Noble gasses, Argon and Xenon, are used so that chemical reactions, which complicate the energy transfer, will not be prevalent. The energy of the incoming X-ray photons is usually transferred to a cloud of ions and electrons through a combination of photoelectric and Auger processes, and later they are multiplied by ionization avalanches in the strong electric field around the anode wires. For example, a photo electron is ejected from the inner most K-shell. The vacancy in the K-shell thus created is filled by an electron in outer shells. The energy difference between the two shells is released in one of two ways: Auger electron emission from the outer most shells, or fluorescent X-ray emission. The primary photo electrons and Auger electrons dissipate their energy by ionizing electrons in outer shells of other counting gas atoms. Finally, all the energy of the incident X-rays, $E(KeV)$, is converted to a primary electron cloud with total number N, which is proportional to the primary X-ray energy as follows,

$$N = \frac{E}{W} \tag{5.1}$$

where W is the mean ionization energy of the counting gas, 26.2eV for Argon and

21.5eV for Xenon. Along the electric field of the detector, these electrons are collected and accelerated toward the anode wire. When the electron obtains enough energy to ionize another counter gas atom electron multiplication process takes place (this happens within a mean free path distance). Usually one primary electron yields on the order of ten thousand electrons on the anode wire. Therefore the height of the pulse is proportional to $N \times M$, where M is the gas multiplication factor. Such proportionality of the pulse hight to the incident X-ray energy is the primary reason for the name 'proportional counter'. The energy resolution of about 18% results from fluctuations in the primary electrons number and the gas multiplication factor.

The detected energy, number of photons and the time of detection are recorded by the satellite and relayed by telemetry to the relay station on earth. The information is stored on magnetic tapes, usually in a binary form.

5.2 THE GINGA MISSION

In this section we describe the Japanese X-ray satellite Ginga (1987 - 1991). The large area counter (LAC) on board Ginga, which used multi wire proportional counters technology, is described. Background rejection methods for LAC are explained, and techniques of data analysis are outlined. A more detailed technical description of

Ginga can be found in Turner et al. 1989 and Makino 1987. Hayashida et al. 1989 and Awaki et al. 1991 explain the background rejection methods for Ginga in detail.

5.2.1 Satellite Description

In figure 5-1 we see the satellite Ginga.

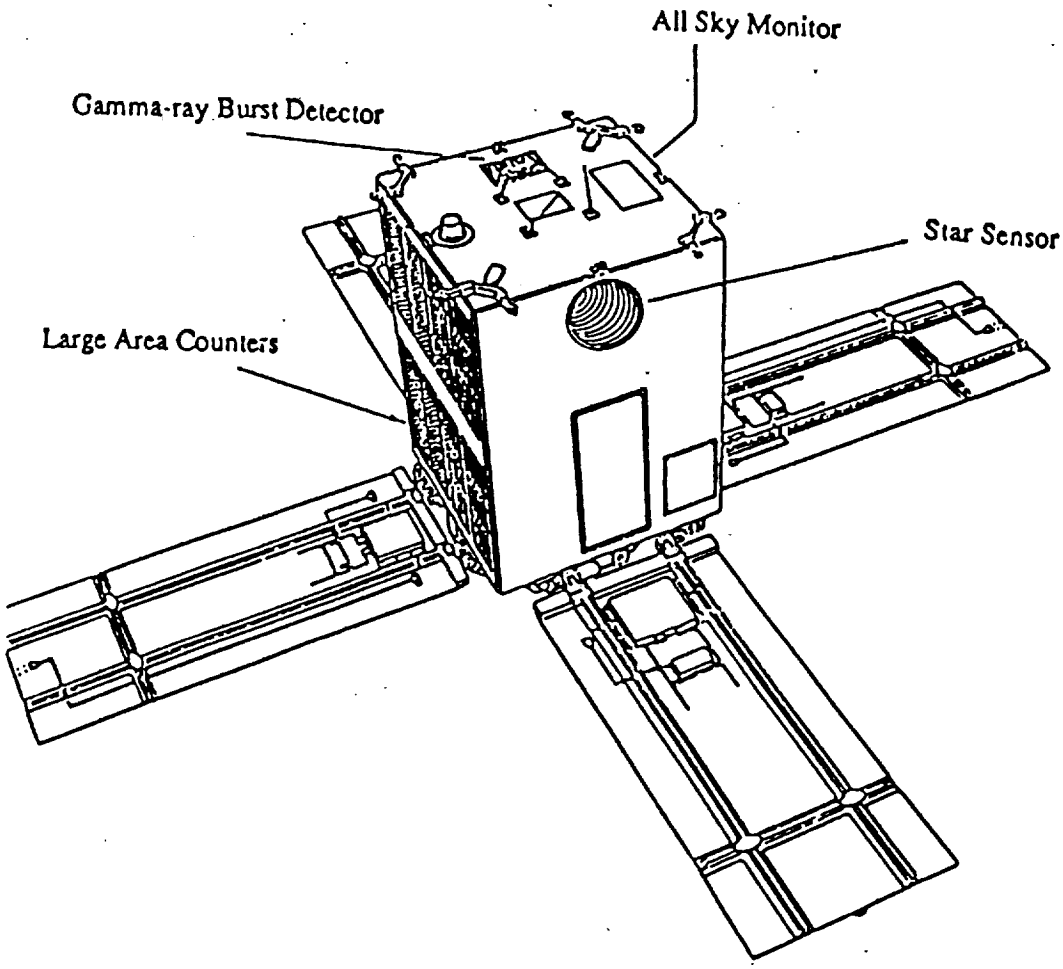

Figure 5.1: The Ginga satellite: the LAC eight detectors are pointed towards the left.

Ginga was launched in February 1987 into a low earth orbit with perigee of 505 km and apogee of 673.5 km, inclination of 31.1^0 to earth's longitudes, and orbital period of 96.5 minutes, which is an equivalent of roughly 15 orbits per day. Ginga satellite orbit decayed slowly as a result of interaction with the upper atmosphere (drag), and was lost on October 1991 when the increased solar activity resulted in increased drag.

The characteristics of Ginga's orbit determine its observational capacity. The relatively low orbit protected the satellite from earth's radiation belts, except in the South Atlantic Anomaly (SAA) where the radiation belt is 'hanging down' because of the weak geomagnetic field. Because of the low orbit the satellite body was also protected from most high energy cosmic rays which are deflected by the geomagnetic field, below energy referred to as the Cut Off Rigidity (COR). Regions with small COR are therefore subjected to high particle background. Because of the high particle background in the SAA weak pointed sources, like Seyfert galaxies and QSOs, could not be observed in the 5 orbits that transcended the SAA. This limited the observation of AGN to 10 orbits per day. In low earth orbit all sources are observed intermittently, because of earth occultation of the source. Out of the 96.5 minute Ginga orbit up to $\sim$ 65 minutes could be utilized for pointed observation, depending on the coordinates

of the observed source. During the rest of the period view of the source is blocked.

the three astronomical instruments on board Ginga were the large area counter (LAC), the all sky X-ray monitor (ASM) and the Gamma-ray burst detector (GBD). Here we present a very basic description of LAC (for further details see Turner et al 1989), which is the only Ginga instrument used for pointed observations of AGN. LAC consisted of eight proportional counters arranged in two layers with total effective area of 4000 cm^2. The counters were filled with a mixture of 75% argon, 20% xenon and 5% CO_2. The x-rays entered through a 62μm thick beryllium window which absorbed very low energy x-rays. The top layer was sensitive in the $1.5 - 37$keV range, while the 'MID' layer was sensitive in the $5 - 37$keV range. The combined sensitivity of the two layers is shown in figure 5-2. LAC is efficient in the $2 - 20$keV for weak sources. The angular field of view with the detector was $1.1^0 \times 2^0$ degrees, with the long axis perpendicular to the satellite equator. LAC had 64 energy channels, out of which the two lowest energy and the upper channels were not used for pointed source observations.

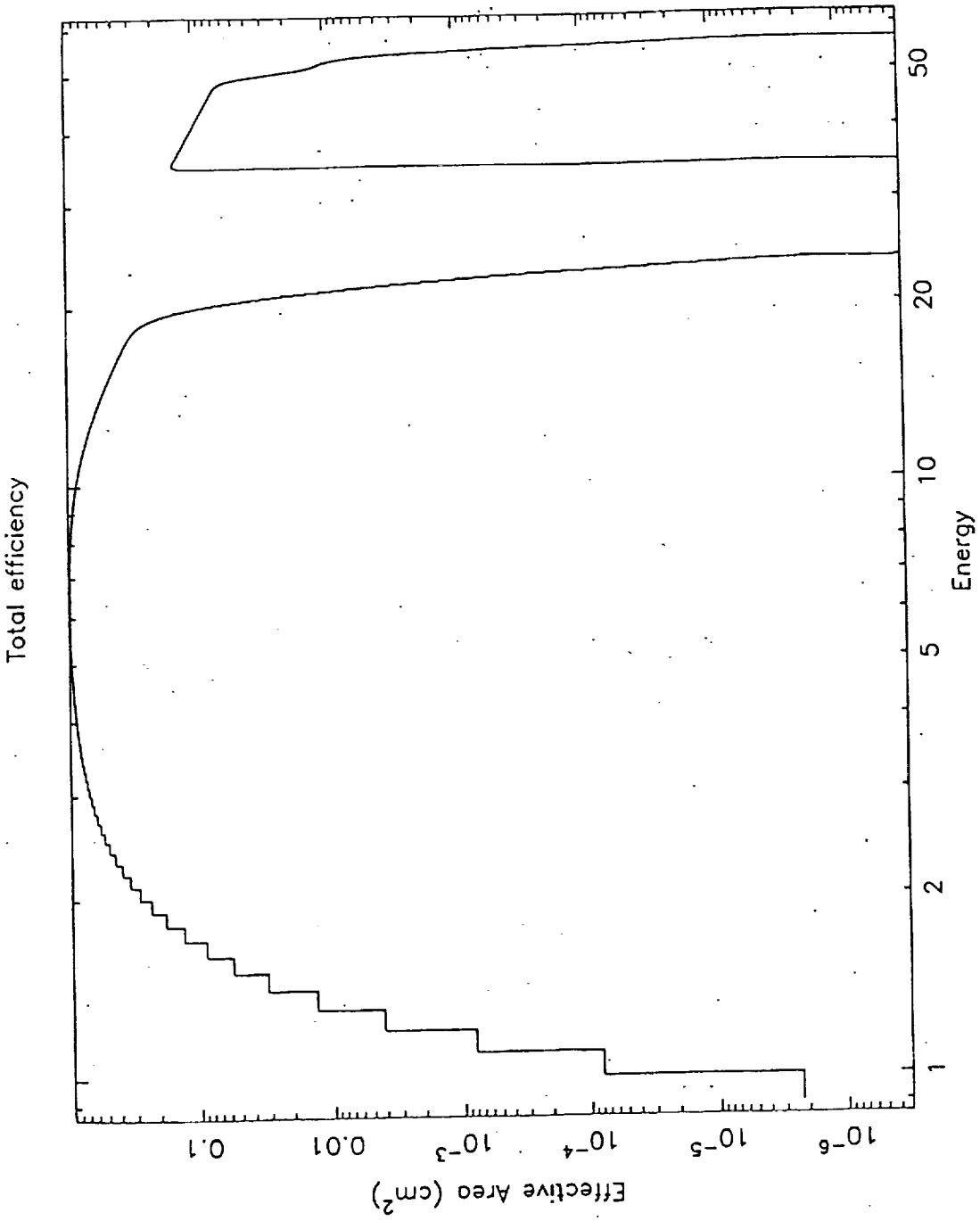

Figure 5.2: The relative effective area per photon energy for a combination of top and mid layers LAC on Cinga.

LAC on Ginga was a very successful instrument. The LAC detector had the largest effective area of any detector that has flown so far in this energy range. As such, it collected a high number of photons and could determine flux level, spectral features, flux variability and spectral variability with high statistical significance. LAC was therefore useful in discovering new spectral features in AGN. It was also the first X-ray detector that had significant sensitivity in the $10 - 20$keV energy range (Mushotzky, Done and Pounds 1993). Data from LAC was also used to determine significant X-ray spectral variability in AGN for the first time.

5.2.2 Background Rejection Methods

Unlike telescopes a large area counter has similar collection and detector areas. This makes background rejection very complicated. The many events detected by the large area detectors which are the result of ionization of and decay of detector parts by high energy particles and direct detection of particles is referred to as internal background. The large angular field of view requires a very accurate subtraction of the X-ray background radiation and radiation from other sources in the field of view, referred to as external background, which is not spatially smooth on this angular scale. Ginga background subtraction is especially challenging, because no simultaneous background observation was performed. For weak sources the number of total

events exceeds the number of source events even after sophisticated anti-coincidence techniques are applied. A complete description of background rejection for Ginga is given in Hayashida et. al. 1989.

To help the rejection of the main sources of internal background, the satellite recorded some 'house keeping functions'. Among them: When passing through the SAA the detector voltage was lowered, the observation was stopped and the time was recorded; Data bins from the next few tens of minutes right after the passage through the SAA were discarded because of strong components from the short term decay of the activated satellite material. In the other orbits the COR was calculated continuously from the local orbit parameters, including the magnetic field, and data bins which corresponded with the time in which particles with energy less than 9 Gev were expected to hit the satellite were discarded; Data bins from parts of the orbit in which the source was obscured by earth were discarded, as well as data from line of sight which grazed the upper atmosphere and thus contained possible X-ray reflection from the sun; The correlation of counts detected in the MID detectors in the high energy channels with the internal background (see Hayashida et al. 1989), was used for discarding data bins which contained high background; The lower energy channels were used for rejection of soft sources, such as random reflections from the

upper atmosphere of solar flares.

For rejection of the external (sky) X-ray background observation of the region near the source before and/or after the observation was usually used. For verification of this method the method developed by Awaki (1991) is used in our work.

5.3 Data Analysis

In order to obtain high statistical significance in the fitting of spectra several methods are usually employed. For example, data from the top and mid detector layers of LAC are combined for increased detection sensitivity in the $8-20$keV range. Combining these layers results in an increase of some internal background features near 3 and 5 keV (which are probably the result of the 41 minutes and 8 hours typical decays of satellite materials after the passage through the SAA). For flux variability observations eight 16 second collection bins are combined, and the external background is then subtracted.

Spectral fitting files are accumulated over the whole observation, or in temporal groups of certain minimum length so that each spectrum or hardness ratio are obtained with high statistical significance. (The hardness ratio, flux in $8-20$keV divided by the flux in $2-6$keV, is an approximate measure of the overall spectral slope.)

This technique is used in order to find correlation between spectral features. This is a sophisticated temporal analysis of the spectrum which determines the reaction times of parts of the spectrum to the overall changes in flux or hardness of flux. The changes in hardness of flux are generally used in order to find positive and negative delays in the onsetting of changes of the spectral features (Kunieda et al 1990).

5.4 THE ROSAT MISSION AND PSPC

ROSAT stands for ROentgen SATellite and is an X-ray observatory developed through a cooperative program between Germany, the United States, and the United Kingdom. The satellite has been designed and operated by Germany (Trumper 1990). It was launched on June 1, 1990. The ROSAT mission began with a six-month, all-sky survey, after which the satellite began a series of pointed observations which will continue for the duration of the project.

ROSAT carries three instruments. The main instrumentation consists of a grazing angle X-ray telescope (XRT) which can be used with two X-ray detectors: the Position Sensitive Proportional Counter (PSPC) and the High Resolution Imager (HRI). The X-ray telescope is complimented by the Wide Field Camera (WFC), an EUV telescope. With this instrumentation, ROSAT is capable of observing celestial tar-

gets at photon energies in the range from 20 eV to 2 keV (Trumper 1990). Beginning in the first half of 1994, all ROSAT-XRT observations were made with the HRI. After four years of successful operation, the PSPC instrument ran out of gas and stopped operating. The spectral sensitivity of the (late) PSPC is shown in figure 5-3.

Background rejection for ROSAT is relatively simple when compared with Ginga, and is not as critical in the data interpretation stage. We therefore choose not to elaborate on background rejection methods for ROSAT (but see Hasinger, Trumper and Schmidt 1991 and Nandra and Pounds 1992). The analysis of data from PSPC on ROSAT does not require any elaborate methods, such as those mentioned in section 5.2.3.

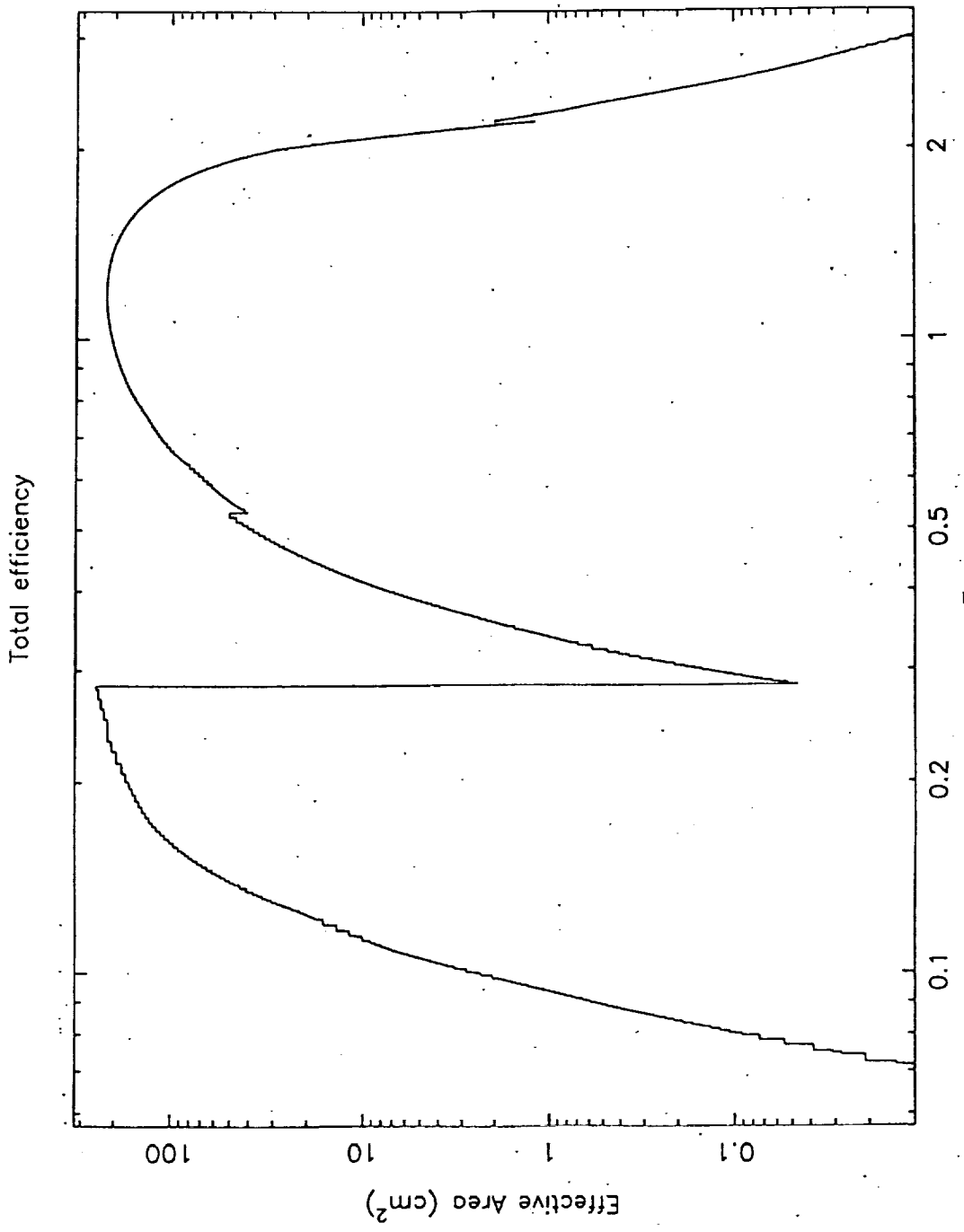

Figure 5.3: The total effective area of the PSPC on ROSAT.

Chapter 6

OBSERVATIONS OF MCG -6-30-15

In this chapter we describe the comprehensive analysis of data from the Seyfert galaxy MCG -6-30-15. After a brief description of past observations of this and other Seyfert 1 galaxies we present the observational data from the Ginga and ROSAT satellites. We then try to fit the observed flux variability, spectrum and spectral variability with current models of AGN central engines.

6.1 OVERVIEW

Much has been learned about the nuclei of Seyfert 1 galaxies from their X-ray spectra and light curves in the last decade. Ginga and ROSAT missions were instrumental in obtaining that data. Since we used data from these mission we open by presenting some of their successful results.

The X-ray spectrum of Seyfert 1 nuclei has many features. To first order, the $2-50$keV spectrum of the great majority of Seyfert 1 galaxies is dominated by a simple power law of the form $F(E) = AE^{-\Gamma}$photons cm^{-2} sec^{-1} keV^{-1} (Turner and Pounds 1989, Mushotzky, Done and Pounds 1993). This fact, which was known since the successful observations by the HEAO-2 satellite (alias Einstein Observatory), was verified by Ginga. Observations with Ginga and ROSAT have also revealed additional features in the spectra of Seyfert 1 galaxies. Ginga's broad energy band enabled the discovery of a hard 'tail' in the $8-20$keV range (Pounds et al 1990). This tail consists of X-ray flux in excess of that expected from the power law emission. The high photon count in Ginga was utilized in showing that Fe K-shell emission lines are a common feature in the spectra of most Seyfert 1 galaxies (Awaki et al 1991, Nandra et al. 1991). Observations with the German satellite ROSAT have revealed photoelectric absorption by cold and warm (partially ionized) material in the line sight in the $0.1-2.5$keV range. This absorption is larger than that expected from matter in our own galaxy, $\sim 3 \times 10^{20}$atoms cm^{-2} in high galactic latitudes, for most Seyfert 1s (Pounds et al. 1993). Oxygen absorption edges (for example, see Nandra and Pounds 1992), and emission lines (see Netzer, Turner and Pounds 1994 and George, Turner and Netzer 1995) were also found in the spectra of Seyferts by ROSAT and the new

Japanese satellite Asca.

Most Seyfert 1 nuclei show some evidence of variability. A significant fraction of Seyfert 1s was shown to have large amplitude ($\delta F/F > 1$) variability on time scales of days or less (McHardy 1988, Grandi et al. 1992, Green 1993). Ginga's good statistics helped discover temporal variability on very short timescales, and spectral variability on short time scales in most Seyferts. Temporal variability over timescales of hours was observed in more than half of all Seyfert 1s. Temporal variability over timescales of years was found in 97% per cent of all sources. Spectral variability was observed in roughly half of the Seyfert 1s. The spectrum is variable in the sense that the power-law usually steepens when the overall intensity increases (Grandi et al 1992, Mushotzky, Done and Pounds 1993).

We used the advantages of Ginga and ROSAT in our analysis of data from four Ginga and one ROSAT observations of MCG -6-30-15. The Seyfert 1 galaxy MCG -6-30-15 has a bright X-ray nucleus with relatively high signal to noise ratio. The relatively long observations of this source with Ginga made it a good candidate for the possible detection with high statistical significance of variability of continuum with timescales of down to minutes, variability of the absorption column with timescales down to tens of minutes, variability of the hard tail down to hours and variability of

the Fe K-shell emission line on time scales down to several hours.

The results of our analysis of data from MCG -6-30-15 constrain the possible models of this source. We verified that the flux from MCG -6-30-15 changed over timescales down to tens of minutes, which could be related to a size of the continuum emitting region of less than $\sim 3 \times 10^{13}$cm. We saw evidence for changes in the absorption column over timescales of down to hours. The thickness of this warm absorber might therefore be limited to $\sim 10^{14}$cm. The changes in absorption column were anti-correlated with the overall continuum flux, and could therefore be attributed to warm (partially ionized) matter in the line of sight. We also found evidence that the Fe emission line varied on timescales of days, which may correspond with warm or cold matter within 10^{15}cm of the SMBH. The excess of photons in the hard tail was found to be anti-correlated with the continuum flux and correlated with the absorption column. There were two possible interpretations of this result. In the first an accretion disk Compton scattered continuum radiation that was then absorbed by a warm absorber that lied within 10^{14}cm from the disk (see Mushotzky, Done and Pounds 1993). In the second interpretation the warm absorber itself, which only partially covered the continuum source, was responsible for the hard tail. The hard tail therefore included photons which were Compton reflected from warm absorber

outside the line of sight, and photons which were absorbed by the highly ionized warm absorber in the line of sight. In this interpretation the location of the partially covering warm absorber could be determined from the variability of the emission lines (See Netzer 1993, Sivron et al. 1995).

Other observations of MCG -6-30-15 agree with the above models. We verified the results of ROSAT observations of MCG -6-30-15, which revealed the presence of a warm absorber in the line of sight (Nandra and Pounds 1992, Fabian et al. 1994). We also used the observation by ROSAT to verify that MCG -6-30-15 field of view was free of sources that could have complicated the analysis for the lower resolution Ginga detectors. Our results could also be reconciled with recent Asca observations (Reynolds and Fabian 1995), but one of our interpretations differs from theirs.

6.1.1 History of the Observations of MCG -6-30-15

The existence of cold matter in the central engines of AGN is still an unresolved issue. AGN emit strong radiation in wave bands ranging from radio to X-rays. Multi-frequency observations have shown that those different wave bands do not originate in the same spatial region (Done et. al. 1990). In many of these extra galactic sources the spectrum of the X-ray emission itself has complex features superimposed upon a power-law feature (Turner and Pounds 1989, Pounds, Nandra and Stewart

1992, George and Nandra 1994) which is known to be variable, and thus assumed to originate in the central engine of AGN (Guilbert and Rees 1988). Much effort has been directed towards finding whether these features also originate in the central engine. These features are thought to originate in cold, or partially ionized, matter in the central engine. In this chapter we show that in the case of MCG -6-30-15 the origin of some of these features is probably very close to the central engine.

The Seyfert 1 galaxy MCG -6-30-15, at red-shift $z = 0.0078$, was observed by HEAO-2 and EXOSAT before it was observed by Ginga. The detectors on Einstein observatory observed MCG -6-30-15 in 1979 and the detectors on Exosat observed it in 1984 and 1985. The total luminosity was found to be $L_x \sim 0.8 \times 10^{43}$ and $L_{0.2-2} \sim 1.2 \times 10^{43}$erg sec^{-1}, but the luminosity in the EUV range was expected to be much larger due to ionization of the Balmer series lines (Reichert et al. 1985, Pounds, Turner and Warwick 1986). An iron emission line was also found by EXOSAT (Nandra et al. 1989). Analysis of the temporal behavior of this source by means of sophisticated power spectrum techniques have been performed by McHardy in 1988 and Green in 1993 (see section 1.1.5). These yielded a slope of $-1.35\pm^{0.1}_{0.25}$ for the power spectrum for both the Exosat 1985 and the Ginga 1987 observations.

Ginga observations of MCG -6-30-15 were analyzed in several earlier papers. The

Seyfert 1 galactic nucleus of MCG -6-30-15 is among the brightest radio quiet AGN observed, which makes the background subtraction easier than in other Ginga weak sources (Matsuoka et al. 1990, Nandra, Pounds and Stewart 1990), and the comparison of Ginga observations from four different years therefore reliable. Most of the superimposed spectral features mentioned in the previous section are found in MCG -6-30-15, which is found to have a variable flux on time scales down to hours (Nandra, Pounds and Stewart 1990), and is therefore a prime candidate for the detection of spectral features variability. Evidences for a 'soft excess' below 1keV, a strong Fe K - emission line, a possible Fe K - absorption edge and a significant hard tail excess in the $10 - 20$keV were found in previous analysis of the 1987 GINGA observation and the 1984 Exosat observation of this source (Matsuoka et. al. 1990, Nandra, Pounds and Stewart 1990). The recent Asca and ROSAT observations have revealed the presence of an O_{VIII} absorption edge, and a possible O_{VII} absorption edge (Nandra and Pounds 1992, Fabian et al., 1994, Matsuoka et al. 1994, Reynolds and Fabian 1995). Data from the ROSAT and Asca X-ray telescopes have also shown that the absorption by cold matter in the line of sight could not be much more than the galactic value. The recent observation of this source with Asca in the $0.5 - 10$keV energy band, a little bit lower than that of Ginga, has shown it to be spatially clean of

interferences from other sources (especially ones with similar spectrum) in a 1^0 f.o.v. (Nandra and Pounds 1992, Fabian et al. 1994, Inoue 1994), which makes it free of possible confusion with galactic sources.

Our analysis of MCG -6-30-15 focuses on problems that were not addressed in previous papers. Although the flux variability and spectral variability of this source were analyzed by previous authors (September 1987 data, Matsuoka et. al. 1990, Nandra Pounds and Stewart 1990, Fiore et al. 1992) we note that their analyses did not take advantage of the low noise in the late observations data (June 1989, February 1990, July 1990) by GINGA, which we extensively use in this thesis. The transmission rate in those later observations is much improved when compared with the 1987 observation. The main focus of this chapter is much different from the earlier papers in that the emphasis is on variability of the spectral components over ranges from minutes to years, and thus a maximum utilization of the multiple observations is achieved. The fact that the source was observed with the same instrument is extremely helpful in establishing year to year variations.

6.2 OBSERVATIONS

In this section we describe the observations of MCG -6-30-15 by the LAC detectors

on Ginga and the PSPC detectors on ROSAT. The LAC and the PSPC are described in chapter 5.

The conditions of the LAC observations were determined by machine and orbit constraints. The LAC observations were performed in the MPC-1 mode, in which the X-ray signals were accumulated in 48 energy-sorted channels. The temporal resolution in this mode is 16 seconds. To obtain better statistical significance in both the temporal and spectral studies of this source we combined the top and mid layers. This method was effective for the later observations, in which the internal background was reduced due to the decay of Ginga's orbit. The accumulation time for the light-curves was chosen to be 128 seconds, just above the Poissonian noise. The maximum continual observation time obtainable by Ginga is roughly $1000-2000$ seconds. Interruptions due to Earth occultation, passage through the South Atlantic Anomaly (SAA) and other high background regions can be noticed in the light curve in Figure 6-2. A 1000 seconds accumulation time is also the shortest for a spectrum of this source. The longest continuous observation time we used was five, almost consecutive, observation days (see table 6-1).

Table 2. MCG -6-30-15 observations in this thesis:

File names[a]	Date of Observation[b]	Instrument[c]	Flux[d]
87	October 9-10 1987	LAC	10^{-11}
89	June 25-26 1989	LAC	10^{-11}
89a[e]			
89lw,md,hi			
89lmdmin,himin[e]			
89sft,hrd			
90	February 2-7 1990	LAC	
90a[e]			
90lw,md,hi			
90lwmin,mdmin,himin			
90sft,hrd			
90d1	February 2		
90d2	February 3		
90d3	February 5		
90d4	February 6		
90d5	February 7		

[a]File names after comma have the same first three letters.

[b]The dates in which the observation took place.
[c]LAC: Large Area Counter on Ginga. PSPC: Position Sensitive Proportional Counter on Rosat.
[d]Flux at 1 Kev.

MCG -6-30-15 ($\alpha = 13^h33^m00^s$, $\delta = -34^002'$) was observed on four separate occasions with Ginga. In the September 10, 1987 observation two of eight detectors, placed at an end of the 4×2 detector array, were excluded because they were illuminated by the sun at angles $< 75^0$. The other detectors were in the shadow of the solar panel. Only top layer data was used, because at that early stage of the mission the internal background was the largest, and because the mid layer exhibits a lower efficiency for X-rays when compared with the particle noise. Also, the collimator efficiency was mediocre ($< 85\%$, Nandra, Pounds and Stewart 1990). These handicaps resulted in different values for the same spectral features when different background substruction were used (See Nandra et.al. 1990 for details). In reanalyzing this measurement we add the mid layer, which significantly increases the efficiency in the $10 - 20$keV range (see section §4). Adding the midlayer increases the internal background because the satellite was at a high altitude in the early stage of the mission, but must be done in order to be consistent with the later observations. The background subtraction method, similar to that performed by Matsuoka et.al. 1990, used nearby sky background, observed within several days, in the direction $\alpha = 13^h13^m$, $-38^042'$.

In the June 25-June 26, 1989 observation the collimator efficiency was high, the overall background was lower because of the satellite descent into the upper atmo-

sphere and the low solar activity, and the adjacent day background observation was in MPC-1 mode. The overall flux level was higher and all detectors were pointed at an angle $> 90^0$ from the sun. We therefore used an off source data base made from observations in the direction ($\alpha = 13^h31^m$, $\delta = -35^058'$) on June 24, 1989.

By far the longest observation of MCG -6-30-15 with Ginga occurred on February 2nd through 7th 1990. During that period the LAC field of view drifted on several occasions, resulting in low collimator efficiency during most of the February 4th observation, and the last few orbits on February 2nd and 5th, all of which were discarded. For background subtraction two methods were used. A nearby observation of blank sky on February 12, 1990, in the direction $\alpha = 13^h31^m$, $\delta = -35^058'$ was used as background for the observations. We also used the sky averaging method described by Awaki 1991. The nearby blank sky observation was chosen, because of better correlation of mid to top layer ratio with the theoretical value. In figure 6-1 we see the correlation of the top to mid ratio with its theoretical value for the 1990 observation.

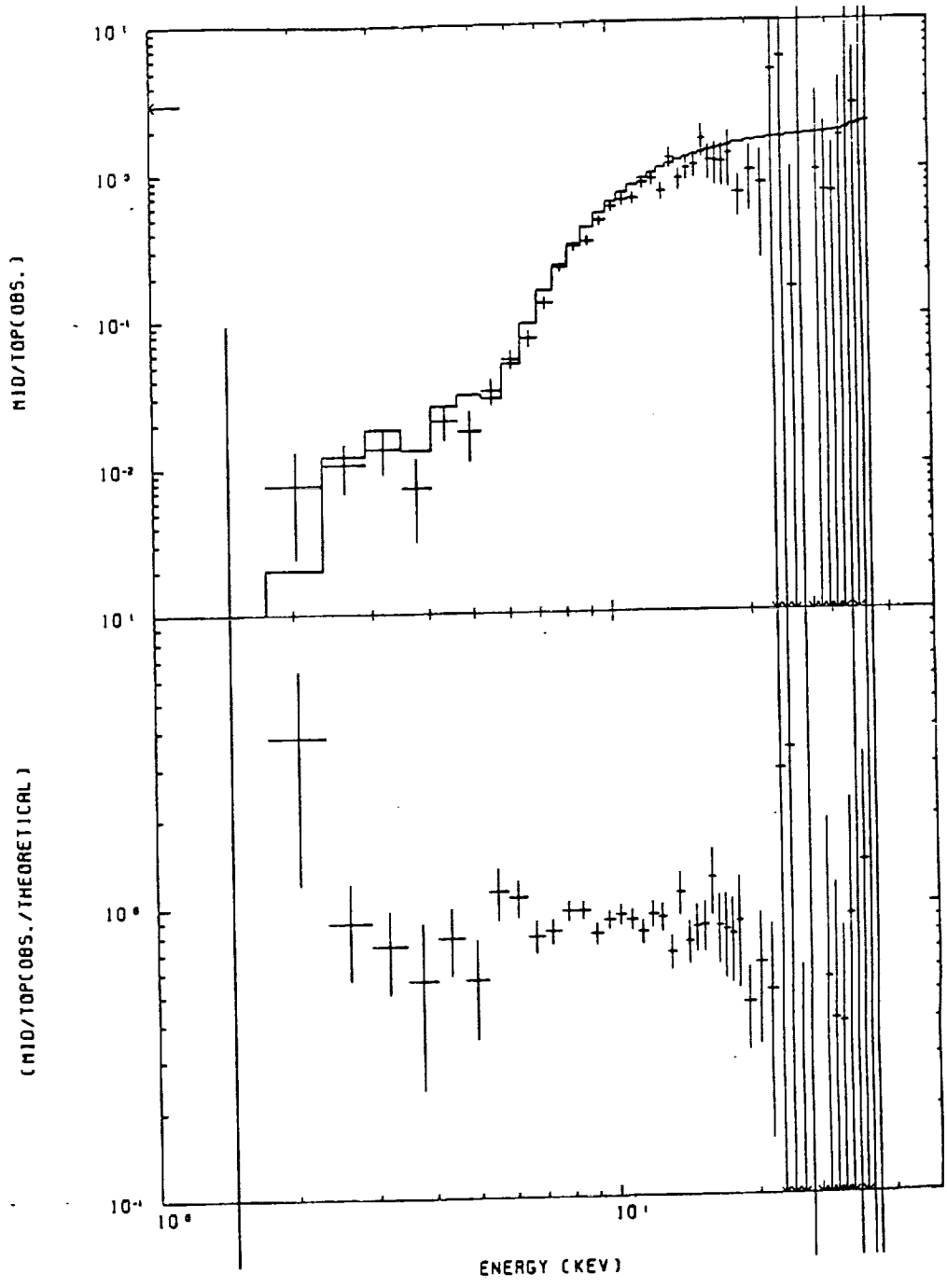

Figure 6.1: The expected theoretical ratio of the counts observed in the top layer of the LAC detectors over the mid layer is shown in solid steplike curve. The observed value is shown by the error bars. This method is used for verification of data quality.

We have reanalized the PSPC observation of MCG -6-30-15 on January 29, 1992 using standard background subtraction and correcting for the 10 arc-minutes misalignment which can be seen in figure 6-2. In figure 6-2 we see that MCG -6-30-15 was roughly 10 arc-minutes off target on the date of the observation. It is also clear that there are no major interferences from other sources in that observation.

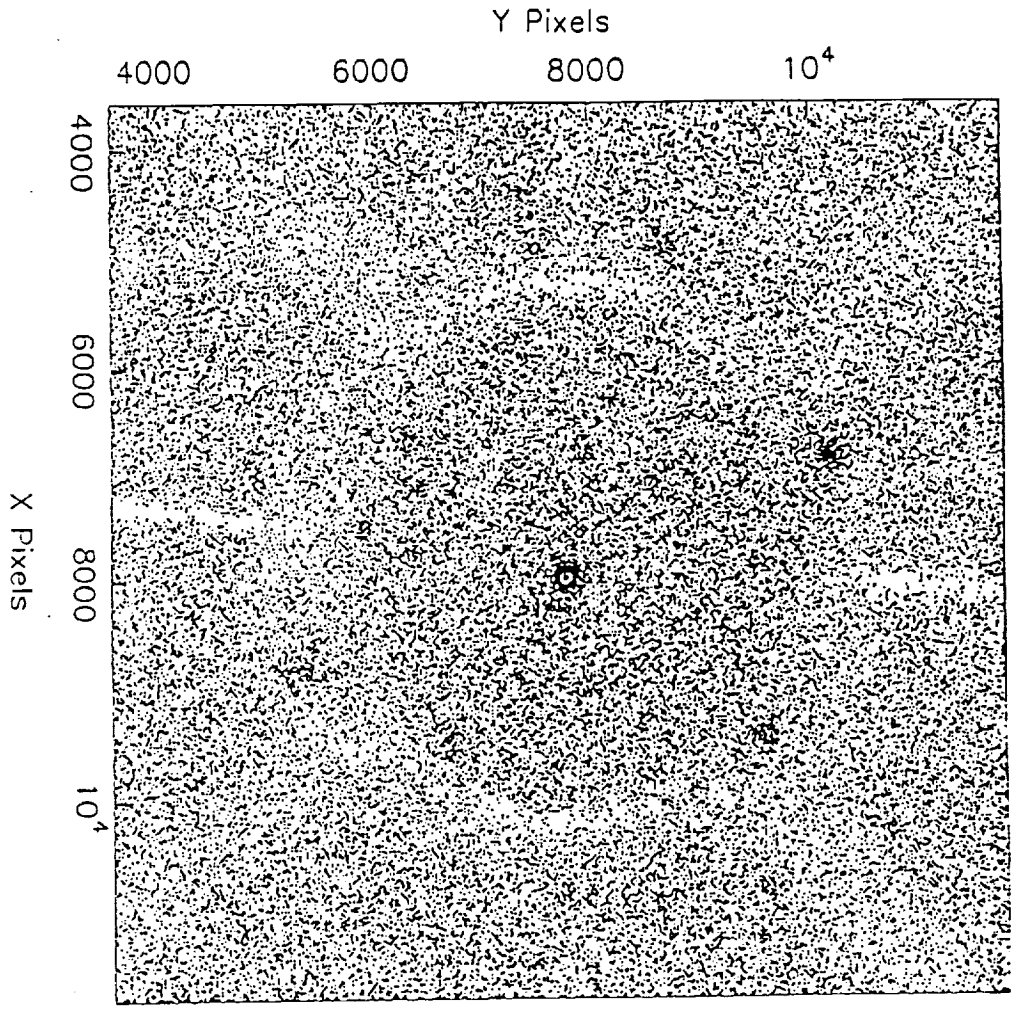

Figure 6.2: Rosat observation of MCG -6-30-15 on January 1992 shows the field of view to be free of intense hard sources.

6.3 INTENSITY VARIATIONS

Before looking at the X-ray spectrum of an AGN observers usually consider the light curve in the different wavebands. Visual inspection of these light curves usually indicates the general spectral variability behavior of the source.

6.3.1 Light Curves

The light curves observed by the top and mid layers of LAC in the first day of the 1990 observation are presented in figure 6-3. The total (background subtracted) flux of $2 - 20$keV photons is shown in the lowest panel. The lower energy cutoff (2keV) of the low band, shown in the middle panel, is chosen so that the soft excess, and the O_{VIII} edge of MCG -6-30-15 (Nandra and Pounds 1992, Walter and Fink 1993) are not included. The high energy cutoff (4keV) of the low energy band was chosen so that the Fe K line (6.4keV) is not be included. The low energy cutoff (8keV) of the high energy band was chosen to avoid possible contribution from the Fe edge ($7.1 - 8.8$keV, depending on ionization state, but known to be less than 8keV in this source), if such edge existed. The high energy cutoff (20keV) of the high energy band, shown in the upper panel, was chosen to discard the energy range with low signal to noise ratio.

The light curves in the 1987, 1989 and 1991 observations show similar behavior (however, see chapter 7).

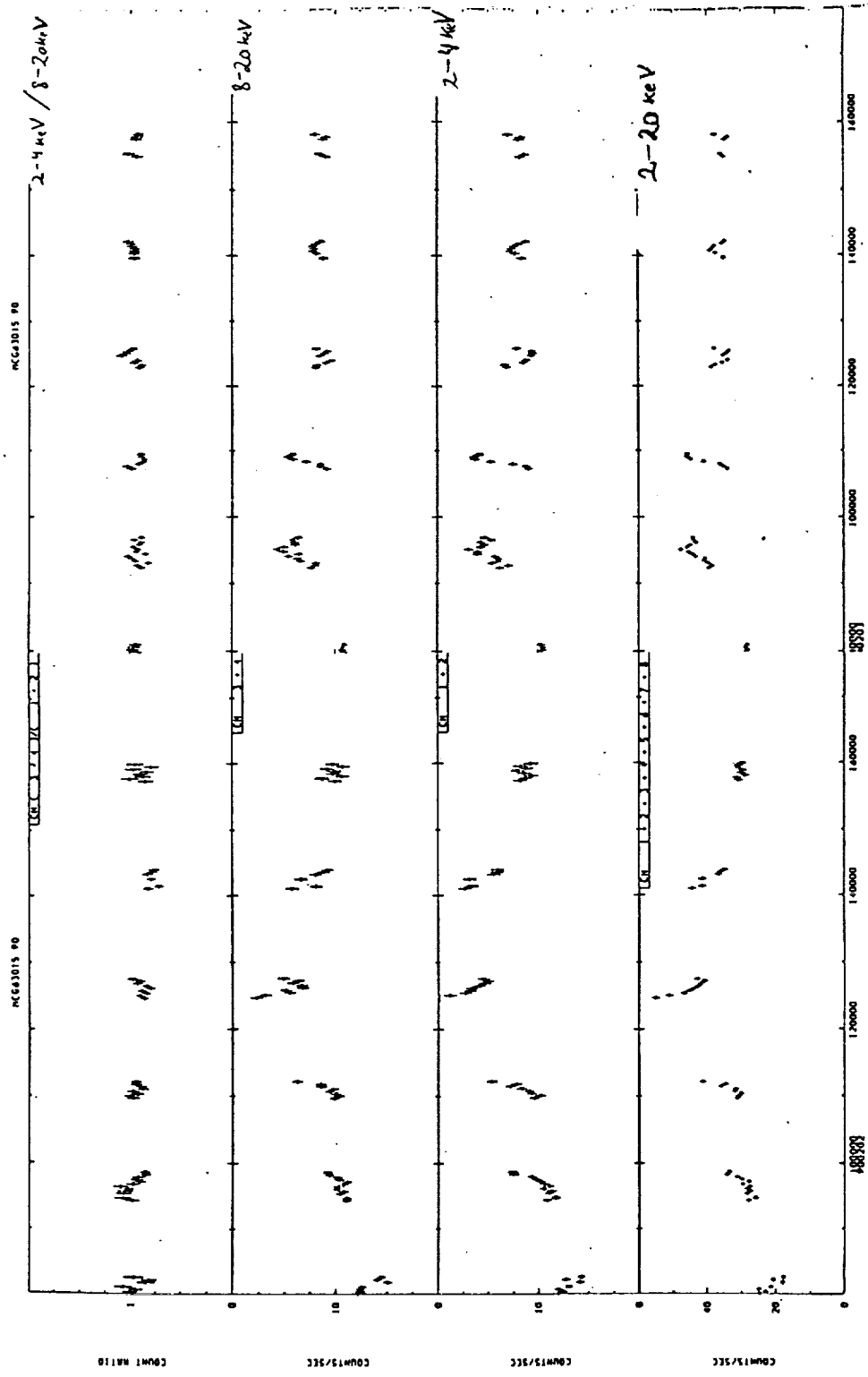

Figure 6.2: The flux variablility observed by Ginga in the first two days of the 1990 observation. The variability of the total flux is shown in the lower panel, the variability of the $2-4$Kev flux is shown in the second panel. The variability of the $8-20$Kev flux is shown in the third panel. The ratio of the $8-20$Kev over the $2-4$Kev flux is shown in the top panel. The abscissa unit is seconds.

6.3.2 Correlation of the Two Energy Bands

In the upper panel of Figure 6-3 we see correlation between the low and high energy bands. The hardening of the spectrum with decreasing flux is obviously present throughout the observation period. No delays can be inspected by eye (delays with low significance level were found in Piro et al. 1992 for the 1987 observation). Assuming that specific spectral features that were emitted from the AGN are responsible for these changes we can differentiate between models in which the hardening with flux is expected and other models.

In figure 6-4 we see the correlation of the $8 - 20$keV and $2 - 4$keV energy bands with 128 seconds time bins. Note that the data cannot be fit with a line that goes through the origin. The existence of hard photons in the zero soft photons limit may be attributed to reflection or partial covering of a power-law spectrum (see section 6.4), whereas the scattering may be attributed to delays.

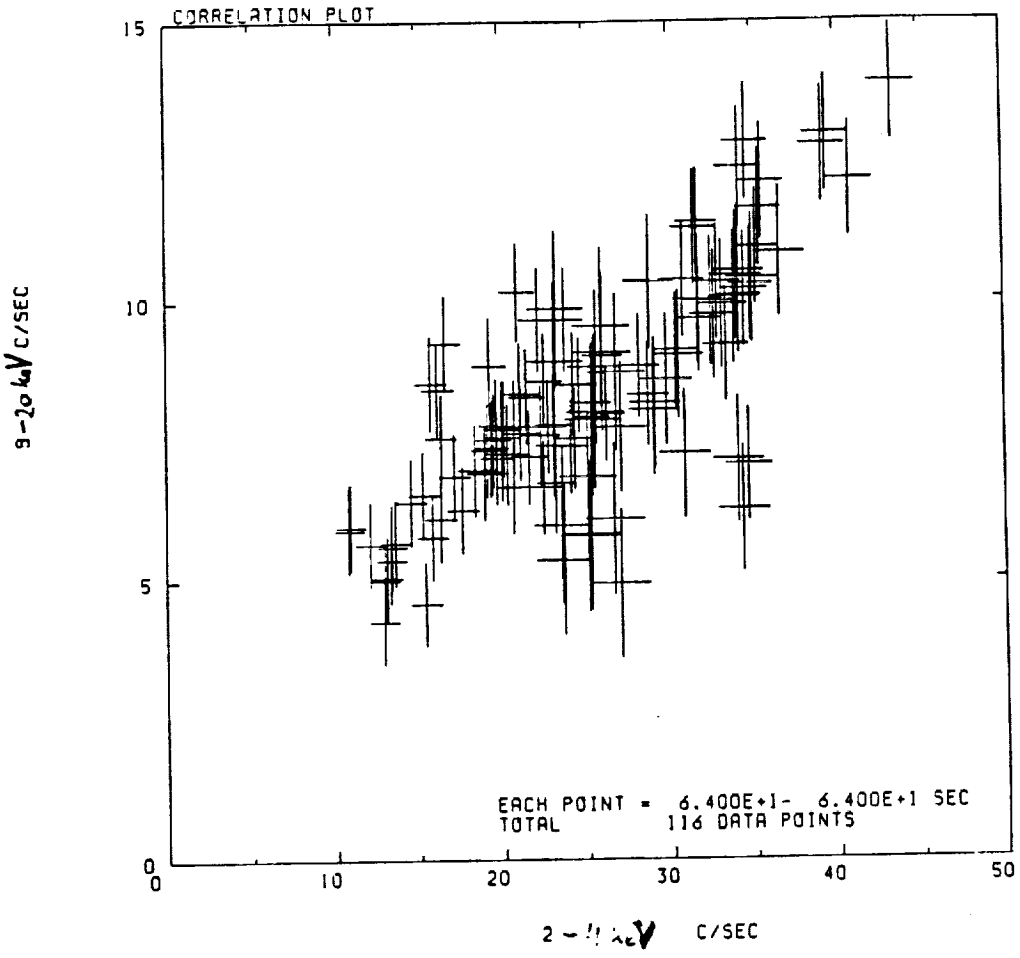

Figure 6.4: The correlation of the 8-20 keV flux with the 2-4 keV flux.

6.4 CHANGES IN SPECTRAL FEATURES

The various parts of the spectrum may be related to processes in the nuclei of MCG -6-30-15. In this section we present and evaluate models that may explain the spectral features.

6.4.1 Preliminary inspection of the sorted spectrum

In figures 6-5 and 6-6 we see the raw data after background subtraction for the 1990 observation. In figure 6-5 the accumulation time is the entire observation, whereas in figure 6-6 the data was accumulated by flux level with binning time of roughly tens of minutes. The data was accumulated by flux level with binning times of minutes, tens of minutes, days and years (87, 89, 90 and 91, see table 2). An accumulation of data by hardness ratio with binning time of tens of minutes, as described in chapter 5, results in spectra which are similar to the low and middle flux levels in figure 6-6. Figure 6-7 includes the 1992 observation by PSPC on ROSAT. Similar spectral files for the 1987, 1989 and 1991 observations are described in Sivron et al. 1995.

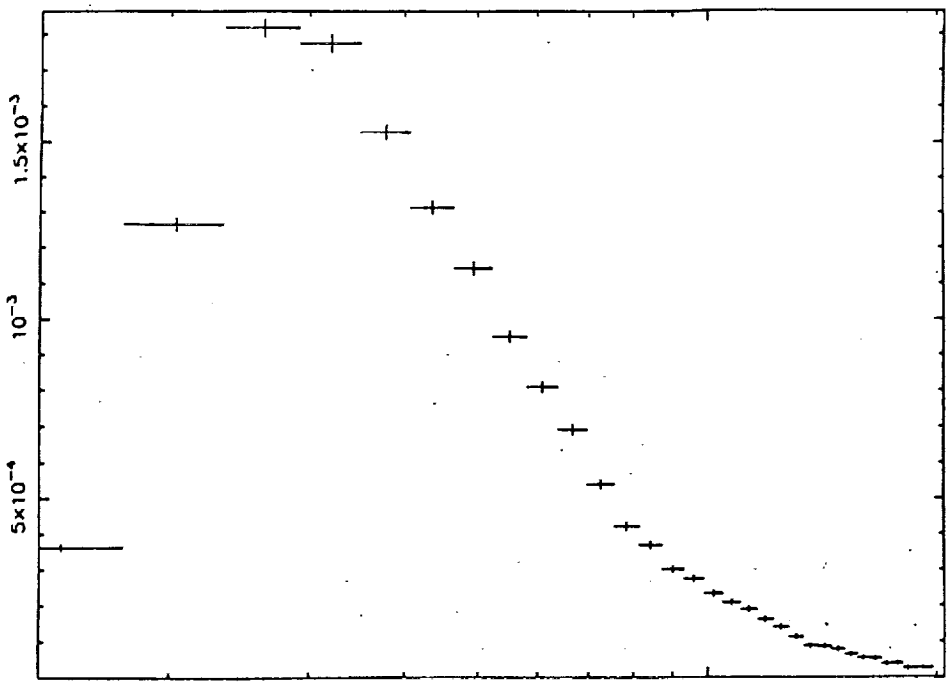

Figure 6.5: The unfitted spectrum of the 1990 background subtracted data.

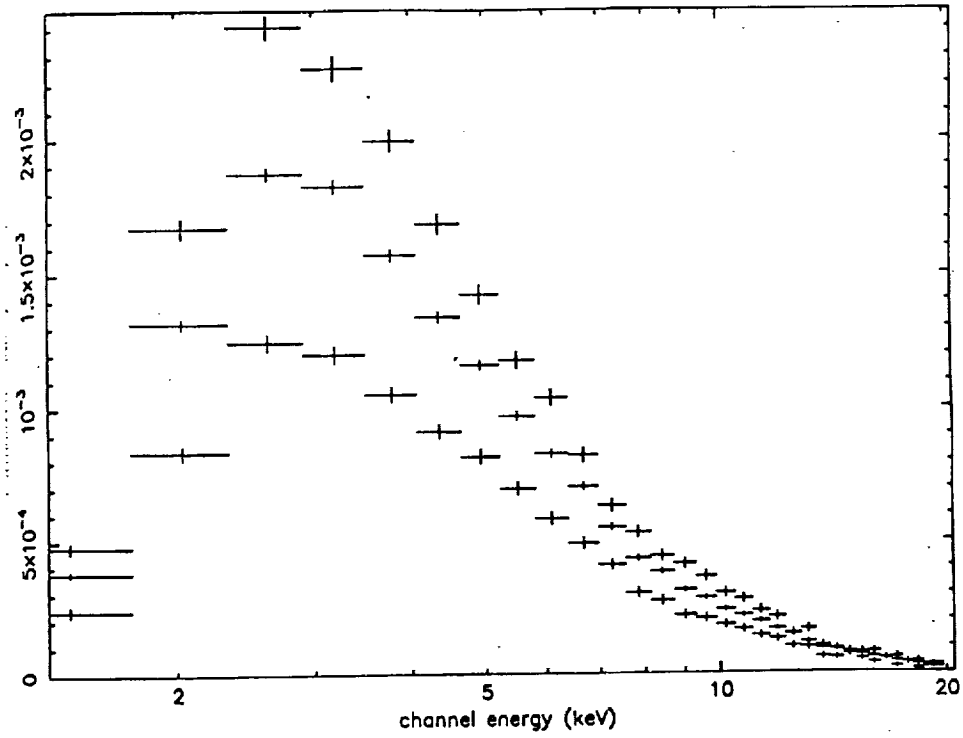

Figure 6.6: The unfitted spectra of three 1990 background subtracted files that were accumulated by flux level with tens of minutes energy bins.

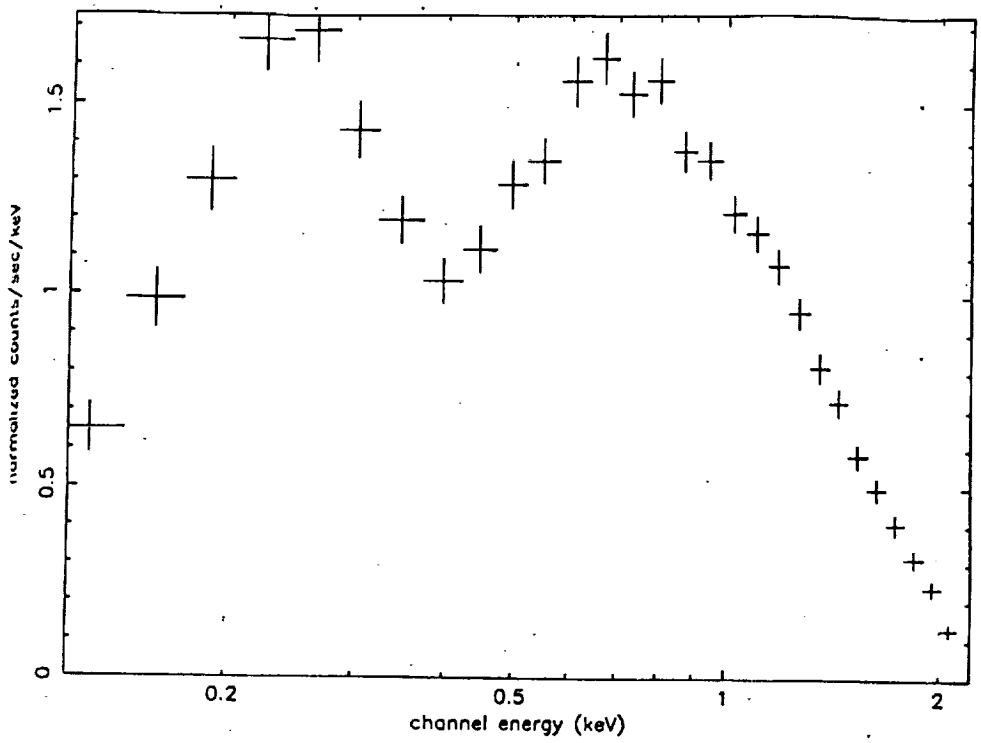

Figure 6.7: The unfitted background subtracted spectrum from the 1992 ROSAT observation.

Although some of the decrease in photon count in the $\sim 2-3$keV range can be attributed to detector efficiency (see figures 5-2 and 5-3 in chapter 5), it is evident that some of the decrease is due to true observed spectrum. This decrease is clearly anti correlated with flux, and also anti correlated with softness. In the $3-5.5$keV the photon counts spectrum seems to have a negative slope, which decreases in the $8-14$keV range. The decrease is anti correlated with flux and softness. In the ROSAT raw data there is deficiency in counts in the $0.2-0.9$keV range, as compared with the detector efficiency and power-law emission (see section 6.4.6 below).

6.4.2 The Absorption Column

The absorption column of matter in the line of sight to MCG -6-30-15 is probably smaller than the $N_H \sim 10^{21.6}$ cm^{-2} value previously considered for the Ginga observations (Nandra, Pounds and Stewart 1990). Preliminary results from ROSAT and ASCA find $N_H \sim 10^{20.7}$ cm^{-2} with high statistical significance (Nandra 1991, Fabian et. al. 1994). Earlier observations with MPC on Einstein observatory (Reichard et.al.1985) and ME combined with LE on EXOSAT (Nandra et al. 1989) are consistent with the smaller values. The approximate galactic value for the cold absorption is roughly $N_H = 10^{20.7}$cm^{-2} (Walter and Fink 1993 and references therein).

It may be noted that fitting models which include warm absorption in or near

the central engine may introduce an additional absorption column as an artifact of the multi-parameter fit, especially as a result of bound-free transitions in partially ionized oxygen. We therefore set the value of the absorption column at its galactic value, for most of our spectral fits. In figure 6-8 a schematic picture of the effect of absorbing material in the line of sight on a power-law spectrum is shown.

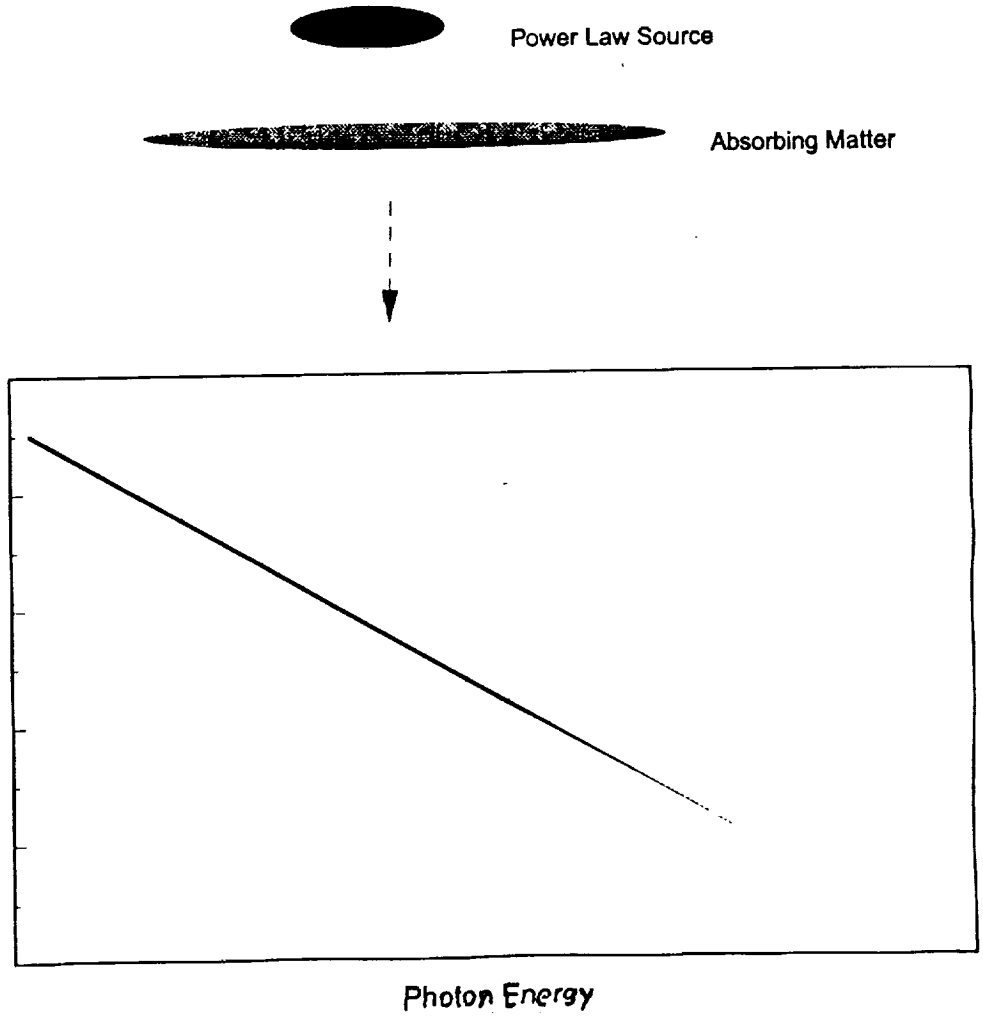

Figure 6.8: A schematic picture of the effect of absorbing material in the line of sight on a power-law spectrum. The upper curve in the graph is the unabsorbed spectrum.

6.4.3 Power law with an absorption feature and an Fe emission line

The simplest description of the above spectra is with

$$F(E) = (N \times E^{-\Gamma} + N_{Fe} e^{-((E-E_{Fe})^2/\sigma_{Fe}^2)}) e^{(-\sigma(E)\times N_H)}, \tag{6.1}$$

where N and N_{Fe} are the normalizations for the power law and Gaussian emission line, E is the photon energy, $\sigma(E)$ is the cross-section for cold cosmic abundance matter, E_{Fe} is the iron emission line energy and σ_{Fe} its observed width.

We fitted the spectra with an iron emission line with local frame energy 6.4keV, a power-law spectrum with photon index in the $1.8 - 2.2$ range, and a cold absorption column in the range $N_H = 10^{20-22}\mathrm{cm}^{-1}$. The natural width of the line was assumed to be 0.05keV, but after Fabian et.al. 1994 reported an intrinsic width of $\sim$ 0.4keV the data was fit again, albeit with negligible changes, because the energy resolution of the LAC proportional counters is 1keV.

The results from the 1990 observations are summarized in tables 3, 4, 5 and 6. The fit is unacceptable in most cases, and we the residuals, using the 1990 file in figure 6-9, show an edge-like feature near 8keV with excess of hard X-ray counts, usually referred to as the hard tail.

Some results can be derived by fitting together spectral accumulation files for

different flux levels in different energy bins. In tables 3, 4 and 5 one can see that the normalization of the power-law emission is variable with at least 99.99% confidence level (see Bevington 1968). The absorption column is also variable with 99.9% confidence level. We assumed this variable absorption column to be an indication of internal changes inside the source, which can probably be associated with variable warm absorption or variable covering factor (see section 6.4.6). In figure 6-10 we see that the photon index Γ and the absorption column are strongly correlated, suggesting that these parameters cannot be individually determined with the above model.

It is not at all clear that the Fe line flux is variable for all time binnings. The confidence level is best for binning by days (90 %) and binning by years (95 %), both of which are only marginally acceptable. Figure 6-11 is a schematic picture that describes the possible location of the Fe line emitting matter.

figure 6-9

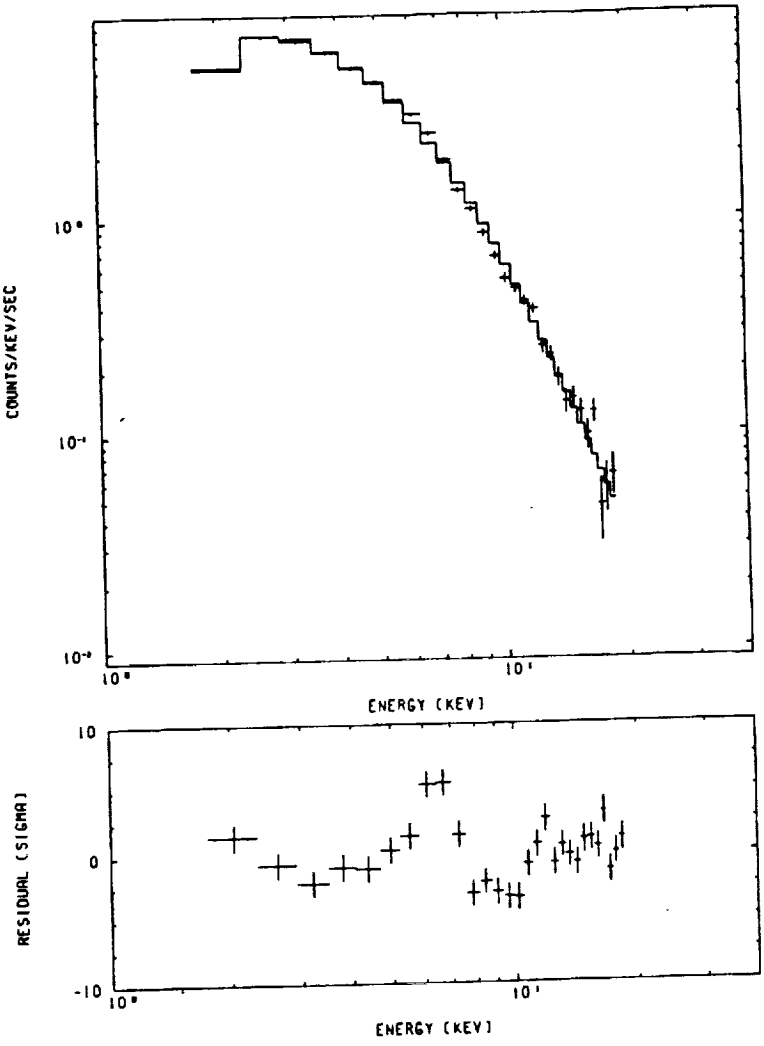

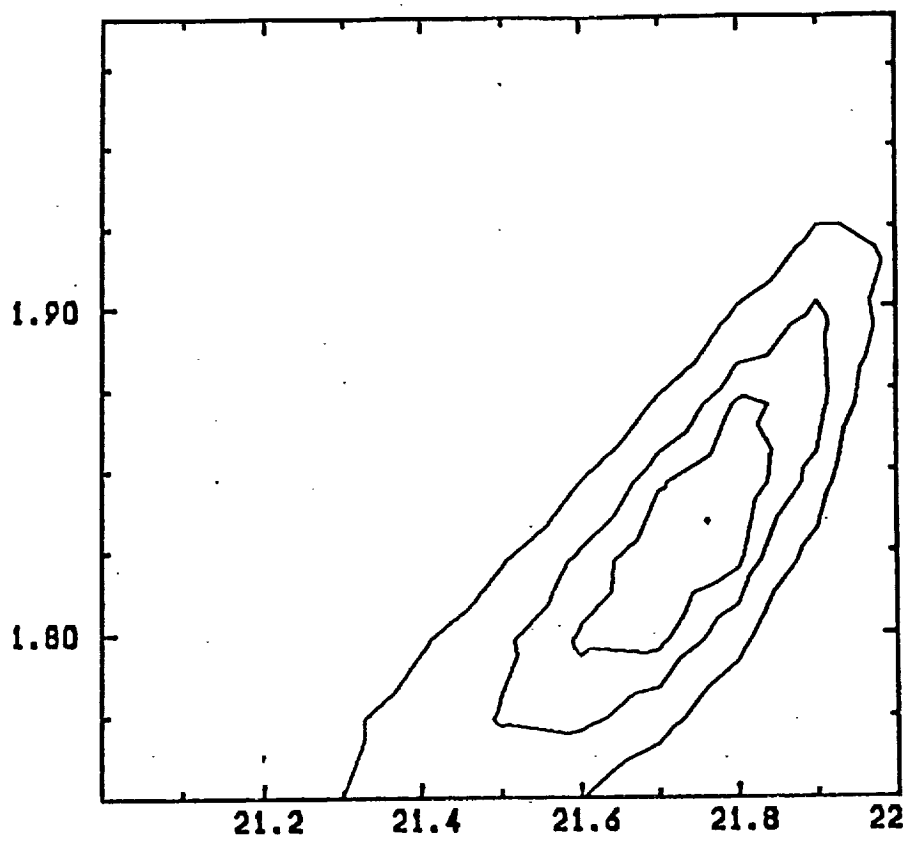

Figure 6.10: The χ contour plot for the absorption column and the photon index in the second day of the 1990 observation. The inner contour corresponds to 99% confidence level of fit, the second contour corresponds to 95 % confidence level, and the outer contour corresponds to 67 % confidence level.

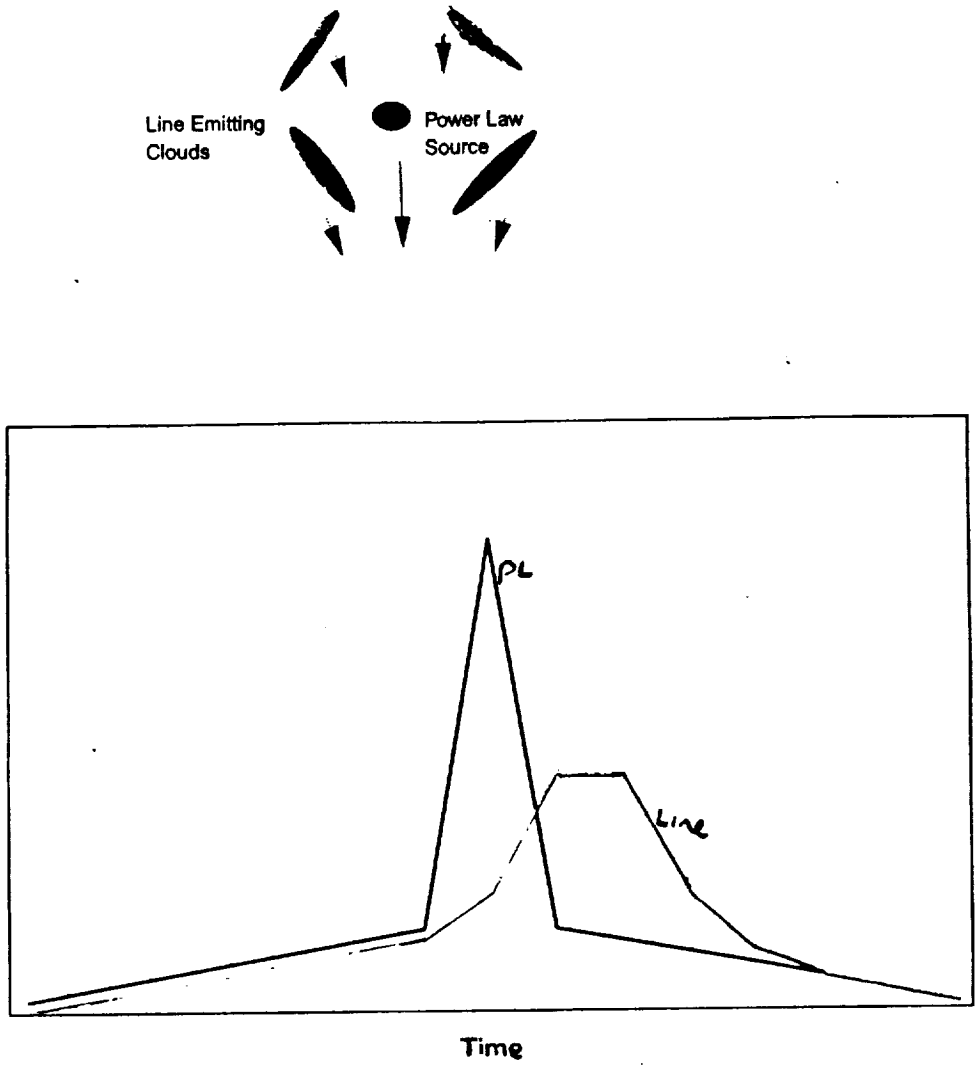

Figure 6.11: A schematic picture that describes the possible location of the Fe line emitting matter around the power law source. The graph describes the subsequent delay in Fe emition flux with respect to the power law flux.

6.4.4 The Hard tail and the Apparent hard 'Edge'

There are two models with which we tried to determine if the hard tail and edge features are variable. The first one is the disk reflection model. The disk model can be written as

$$F(E) = (N \times E^{-\Gamma} \times [1 + rA(E)] + N_{Fe} e^{((E-E_{Fe})^2/\sigma_{Fe}^2)}) e^{(-\sigma(E)\times N_H)}, \qquad (6.2)$$

with $r = \Omega/4\pi$, where Ω is the solid angle subtended by the disk, and $A(E)$ is the Albedo as calculated, for example, in appendix .

The second model is the partial covering by cold absorber model, or the 'leaky' absorber model. The leaky absorber model can be written as:

$$F(E) = (N \times E^{-\Gamma} \times [1 + f_{cov}/(1 - f_{cov}) e^{-\sigma(E)N_{Hcov}}] + N_{Fe} e^{((E-E_{Fe})^2/\sigma_{Fe}^2)}) e^{(-\sigma(E)\times N_H)}, \qquad (6.3)$$

where f_{cov} is the covering factor, and N_{Hcov} is the absorption column in the cold matter which partially covers the source. We note that for column densities in excess of 10^{23} atoms cm^{-2} this model is not accurate in a three dimensional manner, because some reflection is expected from the absorbers on the other side of the power-law source. For covering factor of much less than ~ 0.5 this contribution is probably very small. (See also discussion in chapter 7.)

The improvement in the fits is similar with both models (see tables 3 through 6). There is also a similar improvement in confidence level when the solid angle or the covering factor become free components. When we fit the different flux level files and let f vary we get significant improvement in fits of about 99.99% significance level in the days and years binning. For r we get 99.99% significance level of improvement for all binnings. This is incredibly important, because it implies that the disk changes on time scales of minutes. In order to verify this point we also checked the files 90hrd and 90sft, with similar results.

Schematic pictures of the reflection and leaky absorber model are shown in figures 6-12 and 6-14. The fits and residuals in both of the above cases are shown in figures 6-13 and 6-15.

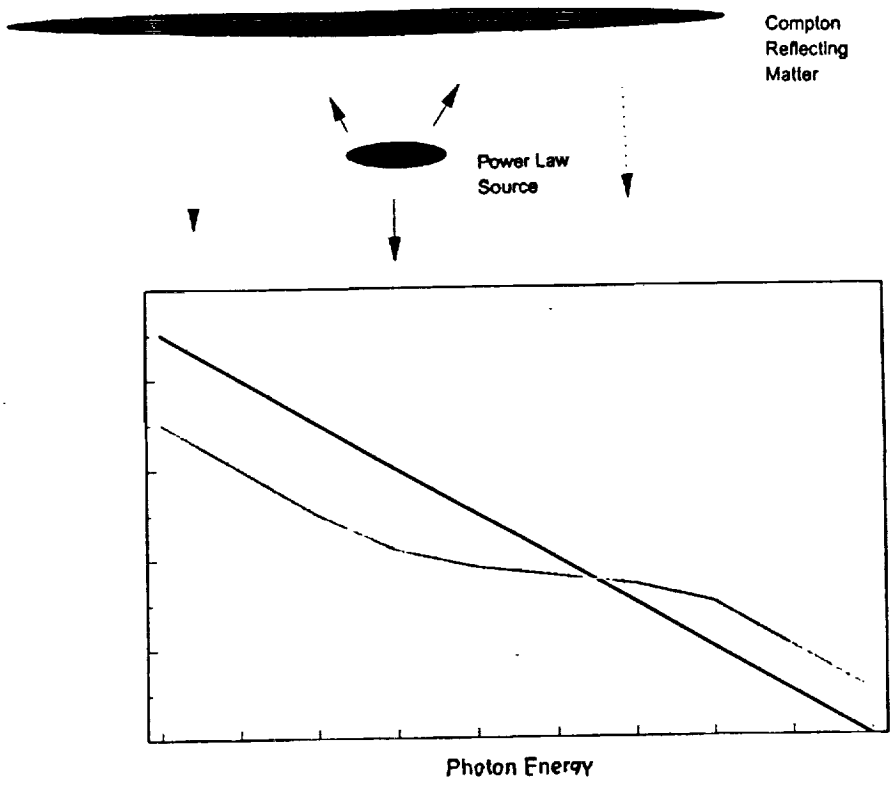

Figure 6.12: A schematic picture of the reflection model, and the resulting spectrum.

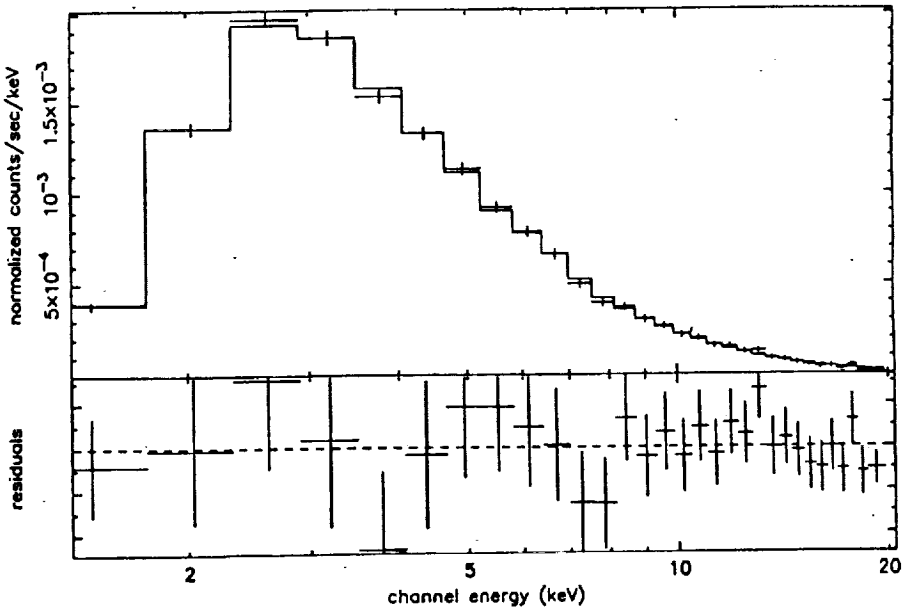

Figure 6.13: The residuals and spectral fits for a power-law reflection from a disk for the 1990 data

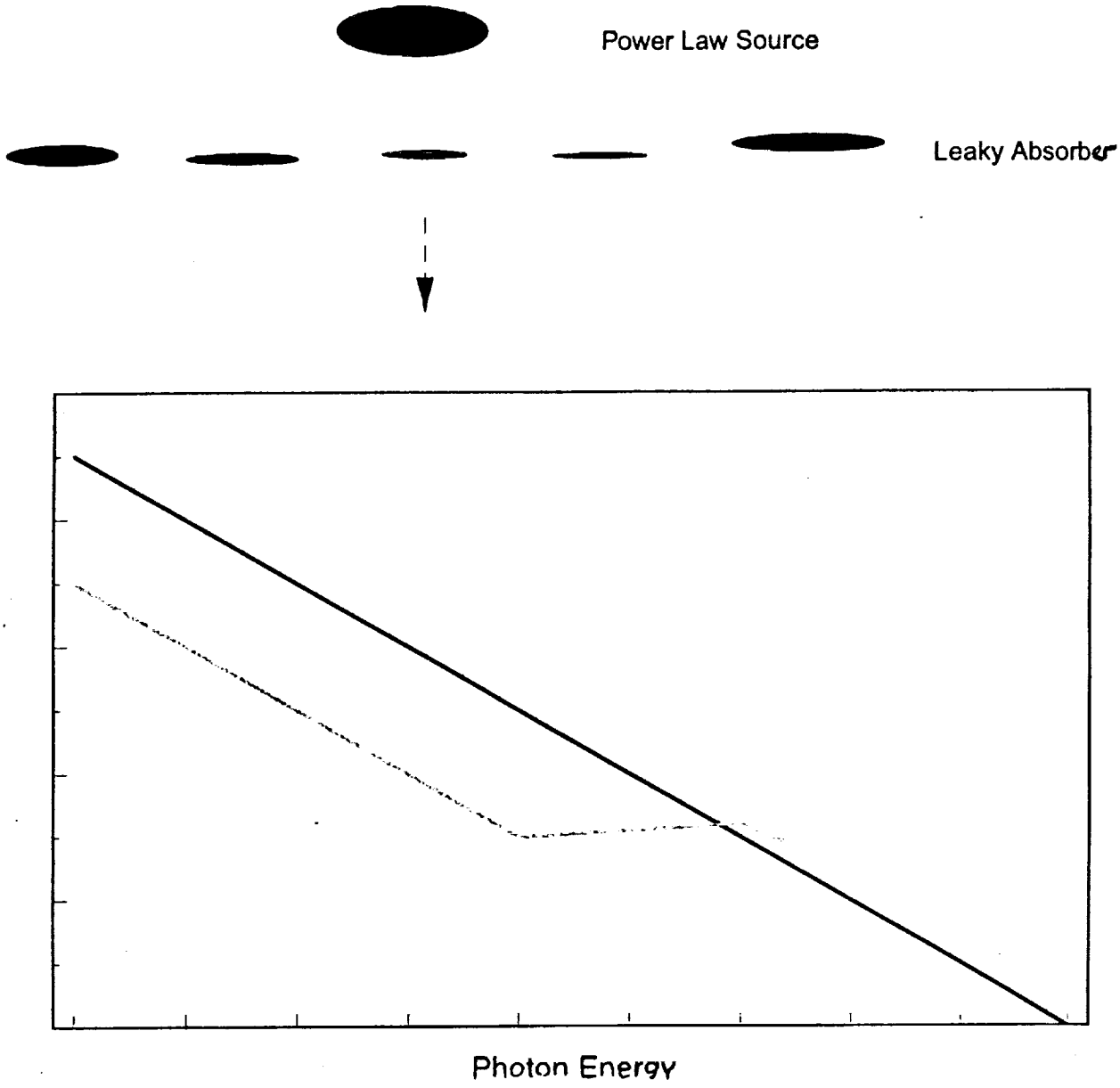

Figure 6.14: A schematic picture of the leaky absorber model, and the resulting spectrum.

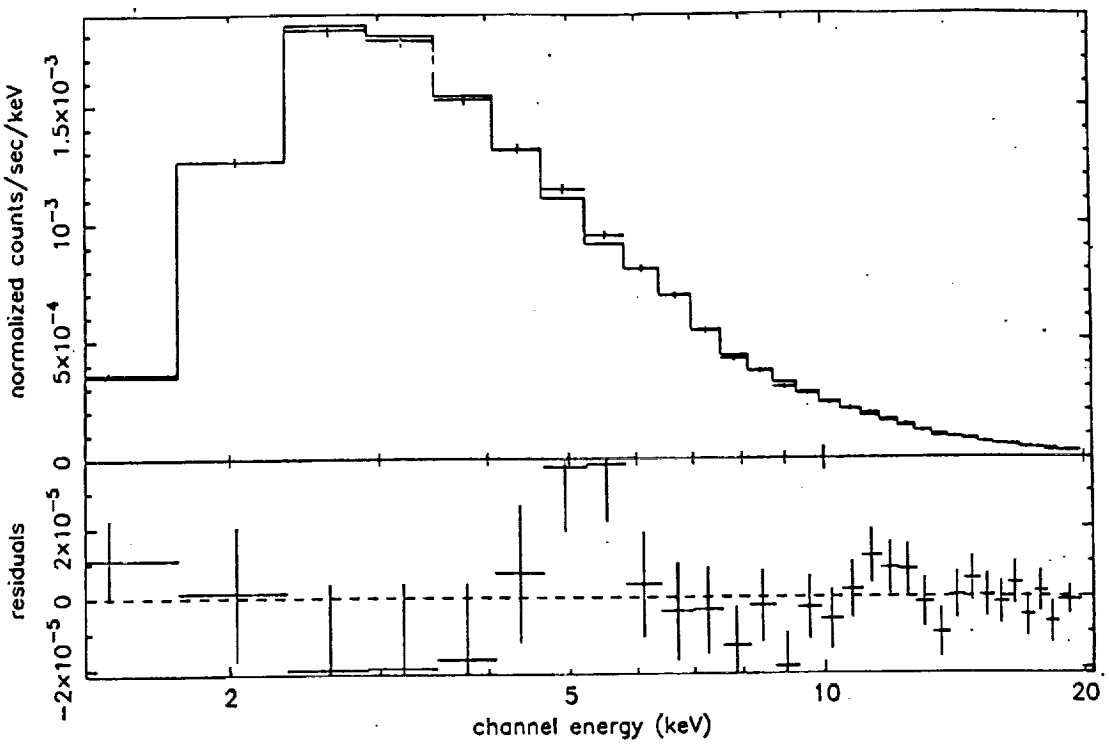

Figure 6.15: The residuals and spectral fits for a power-law source which is partially obscured by cold clouds, for the 1990 data.

6.4.5 Soft X-ray features

Since the soft x-ray absorption like feature is correlated with the hard tail we considered models that naturally relate these two. The first one is the disk plus warm absorber model. To show that warm absorption is indeed possible we fit the ROSAT $0.1 - 2.5$keV data with an edge feature of the sort

$$F(E) = N \times E^{-\Gamma} \times e^{-\tau(E-E(edge))} \times e^{(-\sigma(E)\times N_H)}, \tag{6.4}$$

where $\sigma(E)$ is set to the galactic value, and $\tau(E - E(edge))$ is the edge optical depth. In figure 6-16 an edge is indeed apparent in rest frame energy 7.8keV, corresponding to highly ionized O_{VII} or O_{VIII} oxygen (see Nandra 1992).

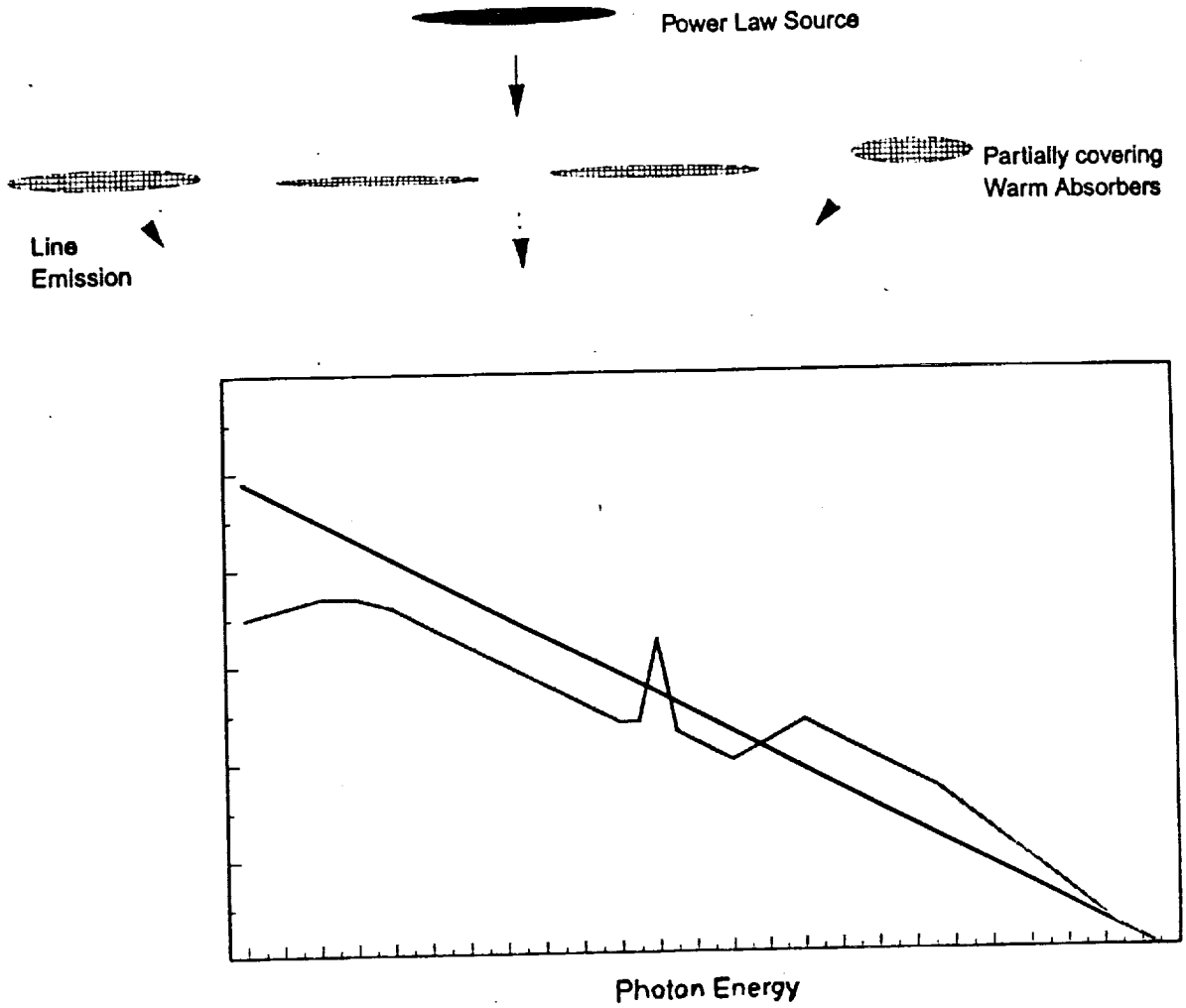

Figure 6.16: A schematic picture of the partial covering by a warm absorber and the resulting spectrum.

We tried to tie together the coefficients responsible for soft absorption and hard tail in the Ginga data. The fit improves with high confidence level. In order to include more general cases, in which the warm absorber may be, for example, highly ionized in one distance and less ionized in another, we modeled the disk reflection as we did before, but with variable edge (see table 6). In figure 6-16 a schematic picture of the disk plus warm absorber model is presented.

The partial covering model of the previous section was approximated as

$$\begin{aligned} F(E) &= (N \times E^{-\Gamma} \times [1 + f_{1cov}/(1 - f_{1cov})e^{-\sigma(E)N_{Hcov1}}] \\ &\times [1 + f_{2cov}/(1 - f_{2cov})e^{-\sigma(E)N_{Hcov2}}] + N_{Fe}e^{((E-E_{Fe})^2/\sigma^2_{Fe})}), \end{aligned} \tag{6.5}$$

for small covering factors. There is hardly a case in which there is significant improvement when the first covering factor becomes different from the second covering factor, but the mere addition of another absorption column improves the fits tremendously in all time bins (see tables 3, 4 and 5). In figure 6-17 a schematic picture of the partial covering by a warm absorber is presented.

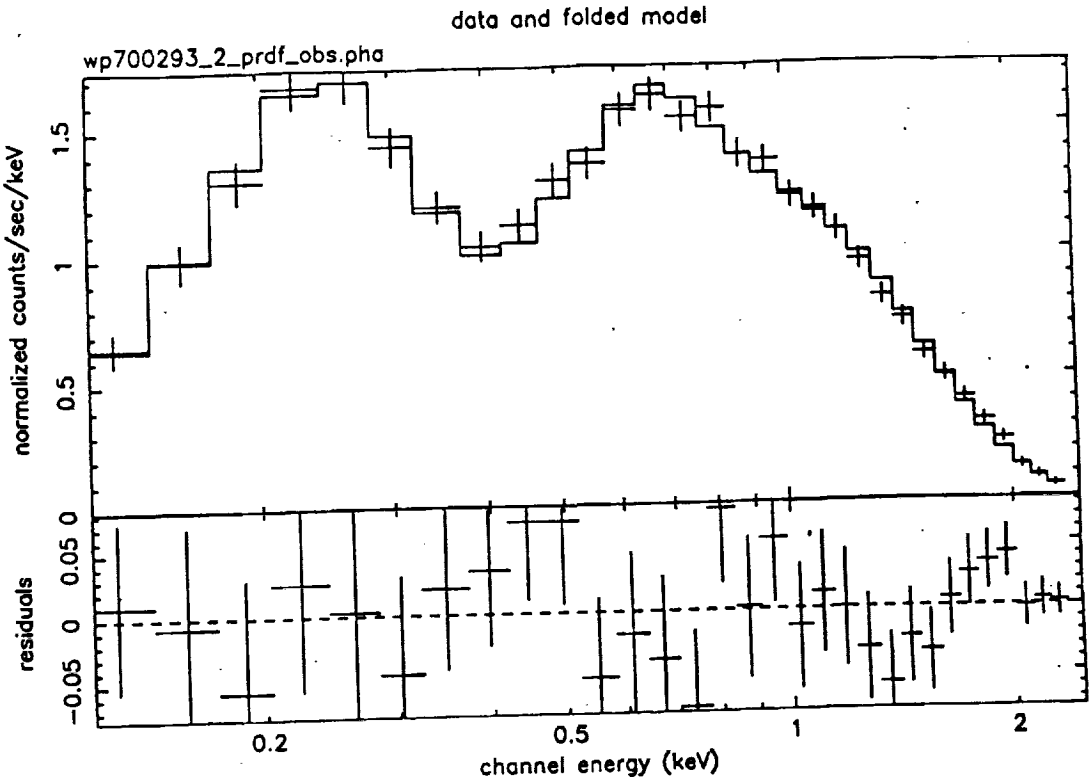

Figure 6.17: The residuals and spectral fits for a power-law source which is absorbed by an oxygen edge in the line of sight for the ROSAT 1992 data.

Table 3. Hours, Partial Covering,90

File	Norm[a]	Γ	N_H[b]	I_{Fe}[c]	f[d]	N_{H2}[e]	χ^2_R/F[f]
90LW	1.5 ± 0.09	1.82 ± 0.03	0.34 ± 0.12	1.04 ± 0.49	...	...	0.92
	2.5	1.82 ± 0.03	0.34 ± 0.12	1.6 ± 3.0	0.4	1000	0.993/0.01
	2.6 ± 0.8	1.93 ± 0.10	4.3 ± 2.9	1.4 ± 0.8	0.29 ± 0.09	340 ± 200	0.97/0.53
	6.0 ± 7.3	2.3 ± 0.4	3.1 ± 2.2	0.5	0.58/0.48	54 ± 20	0.89/3.6
90MD	2.6 ± 0.07	1.92 ± 0.01	0.34 ± 0.05	1.4 ± 0.3	...	...	1.29
	4.1	1.92	0.34 ± 0.05	2.2	0.38	1000	1.4/0.01
	4.7 ± 0.6	2.03 ± 0.05	3.4 ± 1.1	2.2 ± 0.5	$0.33 \pm).04$	310 ± 80	1.05/8.2
	4.5 ± 1.0	2.05 ± 0.08	3.0 ± 1.1	2.0 ± 0.5	0.38/0.26	190 ± 100	0.96/3.3
90HI	3.3 ± 0.1	1.94 ± 0.02	0.35 ± 0.08	1.2 ± 0.6	...	...	1.07
	7.4	1.96 ± 0.05	0.36 ± 0.13	2.7	0.55	1000	1.15/0.14
	6.2	1.96	0.99	2.2	0.45 ± 0.5	1000	1.16/0
	10.9 ± 10	2.35 ± 0.33	3.15 ± 1.44	0.9	0.55/0.42	70 ± 10	1.14/1.3
varpo	1.7 ± 0.4						
	2.6 ± 0.6						
	3.2 ± 0.7						
varFe				1.4 ± 0.5			
				1.4 ± 0.3			
				1.0 ± 0.6			1.4
varΓ		1.82					

Table 3—Continued

File	Norm[a]	Γ	N_H[b]	I_{Fe}[c]	f[d]	N_{H2}[e]	χ^2_R/F[f]
		1.92					
		1.94					1.07/17.8
varf1					0.5		
					0.5		
					0.5		0.0
vΓf1		1.82					
		1.92					
		1.95					1.12/26.7
f1f2		set			0.42		
		set			0.31		
		set			0.26		1.05/29.4
vf1f2					0.57/0.48		
					0.51/0.39		
					0.49/0.37		0.99/11.2
90SFT	3.3 ± 0.1	2.02 ± 0.02	0.46 ± 0.07	1.6 ± 0.4	...	...	1.48
	7.0	2.02 ± 0.02	0.46 ± 0.07	3.3	0.53	1000	1.6/0

Table 3—Continued

File	Norm[a]	Γ	N_H[b]	I_{Fe}[c]	f[d]	N_{H2}[e]	χ^2_R/F[f]
	6.6 ± 3.1	2.02 ± 0.4	1.2 ± 1.2	2.9 ± 2.5	0.49 ± 0.27	1000	1.63/0.0
	11.0 ± 8.9	2.44 ± 0.29	2.5 ± 1.2	1.0 ± 1.2	0.64/0.44	55 ± 13	1.47/3.2
90HRD	1.9 ± 0.1	1.81 ± 0.03	0.27 ± 0.08	1.5 ± 0.4	...	...	1.33
	3.1 ± 1.5	1.81 ± 0.03	0.27 ± 0.08	2.5	0.39	1000	1.44/0.0
	3.1 ± 0.7	1.89 ± 0.09	2.9 ± 2.1	2.2 ± 0.7	0.28 ± 0.07	260 ± 160	1.39/0.9
	5.8 ± 5.9	2.19 ± 0.36	3.3 ± 1.5	1.6 ± 1.0	0.50/0.40	70 ± 17	1.39/1.1
varpo	2.92 ± 0.09						
	2.28 ± 0.07						2.72
varFe				1.00 ± 0.45			
				2.13 ± 0.39			2.57/4.24
varΓ		2.00					
		1.84					1.44/44.7
varf1					0.0		
					0.27 ± 0.03		1.44/46.9
vΓf1		2.02					
		1.95					1.45/0.72

Table 3—Continued

File	Norm[a]	Γ	N_H[b]	I_{Fe}[c]	f[d]	N_{H2}[e]	χ^2_R/F[f]
f1f2		set			0.58		
		set			0.36		1.49/0.7
vf1f2					0.64/0.50		
					0.68/0.62		1.4/3.8

[a]in 10^{-2}erg sec^1 cm^{-2} at 1Kev.

[b]Cold Absorptions, 10^{22}cm^{-1}

[c]in 10^{-2}erg sec^1 cm^{-2} at 1Kev.

[d]Covering factor/second covering factor.

[e]Cold Absorptions, 10^{22}cm^{-1}, coefficient 2.

[f]Note: 31 channels per file. The F test: level of confidence in an additional parameter.

[g]Power law normalization is variable in different files in the fitting program

[h]Variable Gaussian norm

[i]Variable Photon index

[j]Variable one partially covering cold absorber covering factor

[k]PC Cold absorber + variable photon index

[l]Two PC cold absorbers, with a single covering factor

[m]Two PC with two covering factors

References. — (1) me.

Table 4. Days, Partial Covering, 90

File	Norm[a]	Γ	N_H[b]	I_{Fe}[c]	f[d]	N_{H2}[e]	χ^2_R/F[f]
90D2	2.1 ± 0.1	1.95 ± 0.03	0.57 ± 0.10	1.7 ± 0.4	···	···	0.82
···	4.6	1.95 ± 0.09	0.59 ± 0.19	3.5	0.5	1000	0.88/0.17
···	4.6 ± 1.5	1.98 ± 0.04	1.6 ± 1.4	3.3 ± 2.1	0.51 ± 0.20	1000	0.86/0.6
···	3.2 ± 1.0	2.04 ± 0.13	2.4 ± 1.7	2.1 ± 0.9	0.48/0.21	220 ± 290	0.83/2.2
90D3	2.5 ± 0.1	1.88 ± 0.02	0.23 ± 0.07	1.3 ± 0.4	···	···	1.04
···	3.9 ± 0.9	1.92 ± 0.03	0.33 ± 0.08	2.1 ± 1.0	0.33 ± 0.16	460 ± 320	0.83/8.8
···	4.5 ± 1.0	2.02 ± 0.07	4.2 ± 1.7	1.3 ± 0.7	0.29 ± 0.06	260 ± 100	0.72/3.76
···	4.8 ± 1.0	2.0 ± 0.06	4.3 ± 1.8	2.0 ± 0.8	0.27/0.35	350 ± 180	0.70/0.62
90D4	3.0 ± 0.1	1.88 ± 0.02	0.16 ± 0.08	1.3 ± 0.6	···	···	1.67
···	5.4 ± 1.2	1.94 ± 0.03	0.28 ± 0.09	2.6 ± 1.3	0.40 ± 0.14	430 ± 230	1.37/8.07
···	4.7 ± 1.1	1.94 ± 0.06	0.73 ± 0.16	3.7 ± 1.7	0.5 ± 0.1	330 ± 160	1.36/0.07
···	5.7 ± 1.3	1.96 ± 0.06	1.3 ± 2.4	2.6 ± 1.2	0.31/0.41	420 ± 230	1.42/0.01
90D5	2.5 ± 0.1	1.88 ± 0.02	0.23 ± 0.07	1.3 ± 0.4	···	···	1.04
···	3.9 ± 0.9	1.92 ± 0.03	0.33 ± 0.08	2.1 ± 1.0	0.33 ± 0.16	460 ± 320	0.83/8.8
···	4.5 ± 1.0	2.02 ± 0.07	4.2 ± 1.7	1.3 ± 0.7	0.29 ± 0.06	260 ± 100	0.72/3.76
···	4.8 ± 1.0	2.0 ± 0.06	4.3 ± 1.8	2.0 ± 0.8	0.27/0.35	350 ± 180	0.70/0.62
90D6	3.0 ± 0.1	1.88 ± 0.02	0.16 ± 0.08	1.3 ± 0.6	···	···	1.67
···	5.4 ± 1.2	1.94 ± 0.03	0.28 ± 0.09	2.6 ± 1.3	0.40 ± 0.14	430 ± 230	1.37/8.07
···	4.7 ± 1.1	1.94 ± 0.06	0.73 ± 0.16	3.7 ± 1.7	0.5 ± 0.1	330 ± 160	1.36/0.07
···	5.7 ± 1.3	1.96 ± 0.06	1.3 ± 2.4	2.6 ± 1.2	0.31/0.41	420 ± 230	1.42/0.01

Table 4—Continued

File	Norm[a]	Γ	N_H[b]	I_{Fe}[c]	f[d]	N_{H2}[e]	χ^2_R/F[f]
varpo	1.98 ± 0.05						
	2.42 ± 0.06						
	2.93 ± 0.07						
varFe				2.1 ± 0.6			
				1.8 ± 0.4			
				1.0 ± 0.6			1.78/3.64
varΓ		1.76					
		1.88					
		1.9					1.41/24.6
varf1					0.57 ± 0.07		
					0.28 ± 0.07		
					0.3 ± 0.08		14.3
vΓf1		1.84					
		1.93					
		1.96					1.07/35.4
f1f2		set			0.49		

Table 4—Continued

File	Norm[a]	Γ	N_H[b]	I_{Fe}[c]	f[d]	N_{H2}[e]	χ^2_R/F[f]
		set			0.31		
		set			0.28		0.92/10.9
vf1f2					0.43/0.54		
					0.29/0.36		
					0.25/0.4		0.9/4.2
89SFT	2.5 ± 0.1	1.84 ± 0.02	0.20 ± 0.06	1.3 ± 0.4	...	...	1.14
...	4.4 ± 1.3	1.91 ± 0.02	0.29 ± 0.07	2.4 ± 1.3	0.41 ± 0.18	610 ± 340	0.84/11.5
...	4.1 ± 0.7	1.93 ± 0.4	1.4 ± 1.0	2.1 ± 0.9	0.33 ± 0.11	420 ± 250	0.81/0.95
...	4.7 ± 1.1	1.96 ± 0.05	3.2 ± 1.9	2.1 ± 1.0	0.25/0.38	450 ± 250	0.81/0.93
89HRD	1.7 ± 0.1	1.77 ± 0.04	0.50 ± 0.16	1.4 ± 0.7	...	...	1.45
...	4.0 ± 1.0	1.91 ± 0.09	0.82 ± 0.23	3.3 ± 1.7	0.46 ± 0.11	270 ± 150	1.16/8.8
...	12.0 ± 7.0	2.3 ± 0.2	6.6 ± 1.6	4.1 ± 2.1	0.61 ± 0.09	200 ± 50	0.80/11.3
...	12.1 ± 7.4	2.3 ± 0.2	6.6 ± 1.6	4.0 ± 2.2	0.62/0.61	200 ± 70	0.83/0.01
varpo	2.4 ± 0.07						
	1.9 ± 0.06						
varFe				1.1 ± 0.6			
				2.2 ± 0.7			2.02

Table 4—Continued

File	Norm[a]	Γ	N_H[b]	I_{Fe}[c]	f[d]	N_{H2}[e]	χ^2_R/F[f]
		set			0.31		
		set			0.28		0.92/10.9
vf1f2					0.43/0.54		
					0.29/0.36		
					0.25/0.4		0.9/4.2
89SFT	2.5 ± 0.1	1.84 ± 0.02	0.20 ± 0.06	1.3 ± 0.4	···	···	1.14
···	4.4 ± 1.3	1.91 ± 0.02	0.29 ± 0.07	2.4 ± 1.3	0.41 ± 0.18	610 ± 340	0.84/11.5
···	4.1 ± 0.7	1.93 ± 0.4	1.4 ± 1.0	2.1 ± 0.9	0.33 ± 0.11	420 ± 250	0.81/0.95
···	4.7 ± 1.1	1.96 ± 0.05	3.2 ± 1.9	2.1 ± 1.0	0.25/0.38	450 ± 250	0.81/0.93
89HRD	1.7 ± 0.1	1.77 ± 0.04	0.50 ± 0.16	1.4 ± 0.7	···	···	1.45
···	4.0 ± 1.0	1.91 ± 0.09	0.82 ± 0.23	3.3 ± 1.7	0.46 ± 0.11	270 ± 150	1.16/8.8
···	12.0 ± 7.0	2.3 ± 0.2	6.6 ± 1.6	4.1 ± 2.1	0.61 ± 0.09	200 ± 50	0.80/11.3
···	12.1 ± 7.4	2.3 ± 0.2	6.6 ± 1.6	4.0 ± 2.2	0.62/0.61	200 ± 70	0.83/0.01
varpo	2.4 ± 0.07						
	1.9 ± 0.06						
varFe				1.1 ± 0.6			
				2.2 ± 0.7			2.02

Table 5. Years, Partial Covering

File	Norm[a]	Γ	N_H[b]	I_{Fe}[c]	f[d]	N_{H2}[e]	χ^2_R/F[f]
87	1.3 ± 0.1	1.73 ± 0.04	1.1 ± 0.18	1.04 ± 0.56	...	...	2.05
...	14.0	1.85 ± 0.11	1.4 ± 0.3	1.04 ± 1.9	0.89 ± 0.21	1000	1.63/8.8
...	10.5 ± 11.1	1.85 ± 0.05	1.8 ± 0.6	7.5 ± 9.3	0.85 ± 0.16	1000	1.61/0.3
...	20.0 ± 30.0	1.94 ± 0.10	4.2 ± 1.4	10 ± 13	0.64/0.90	1000	1.6/1.2
89a	2.66 ± 0.08	1.91 ± 0.02	0.24 ± 0.06	1.3 ± 0.4	...	...	1.18
...	3.9 ± 0.5	1.96 ± 0.03	0.35 ± 0.08	2.0 ± 0.7	0.27 ± 0.09	310 ± 180	0.88/11.3
...	4.5 ± 0.7	2.00 ± 0.06	2.3 ± 1.4	2.1 ± 0.7	0.31 ± 0.05	290 ± 120	0.86/0.73
...	4.3 ± 0.7	2.01 ± 0.06	1.9 ± 1.5	2.0 ± 0.7	0.34/0.28	240 ± 140	0.88/0.0
89b	3.0 ± 0.1	1.88 ± 0.02	0.16 ± 0.08	1.3 ± 0.6	...	...	1.67
...	5.4 ± 1.2	1.94 ± 0.03	0.28 ± 0.09	2.6 ± 1.3	0.40 ± 0.14	430 ± 230	1.37/8.07
...	4.7 ± 1.1	1.94 ± 0.06	0.73 ± 0.16	3.7 ± 1.7	0.5 ± 0.1	330 ± 160	1.36/0.07
...	5.7 ± 1.3	1.96 ± 0.06	1.3 ± 2.4	2.6 ± 1.2	0.31/0.41	420 ± 230	1.42/0.01
90	2.5 ± 0.1	1.88 ± 0.02	0.23 ± 0.07	1.3 ± 0.4	...	...	1.04
...	3.9 ± 0.9	1.92 ± 0.03	0.33 ± 0.08	2.1 ± 1.0	0.33 ± 0.16	460 ± 320	0.83/8.8
...	4.5 ± 1.0	2.02 ± 0.07	4.2 ± 1.7	1.3 ± 0.7	0.29 ± 0.06	260 ± 100	0.72/3.76
...	4.8 ± 1.0	2.0 ± 0.06	4.3 ± 1.8	2.0 ± 0.8	0.27/0.35	350 ± 180	0.70/0.62
91	3.0 ± 0.1	1.88 ± 0.02	0.16 ± 0.08	1.3 ± 0.6	...	...	1.67
...	5.4 ± 1.2	1.94 ± 0.03	0.28 ± 0.09	2.6 ± 1.3	0.40 ± 0.14	430 ± 230	1.37/8.07
...	4.7 ± 1.1	1.94 ± 0.06	0.73 ± 0.16	3.7 ± 1.7	0.5 ± 0.1	330 ± 160	1.36/0.07
...	5.7 ± 1.3	1.96 ± 0.06	1.3 ± 2.4	2.6 ± 1.2	0.31/0.41	420 ± 230	1.42/0.01
varpo	1.98 ± 0.05						

Table 5—Continued

File	Norm[a]	Γ	N_H[b]	I_{Fe}[c]	f[d]	N_{H2}[e]	χ^2_R/F[f]
	2.42 ± 0.06						
	2.93 ± 0.07						
	2.42 ± 0.06						
	2.93 ± 0.07						
varFe				2.1 ± 0.6			
				1.8 ± 0.4			
				2.1 ± 0.6			
				1.8 ± 0.4			
				1.0 ± 0.6			1.78/3.64
varΓ		1.76					
		1.88					
		1.76					
		1.88					
		1.9					1.41/24.6
varfl					0.57 ± 0.07		
					0.28 ± 0.07		
					0.57 ± 0.07		
					0.28 ± 0.07		
					0.3 ± 0.08		14.3
vΓfl		1.84					
		1.93					

Table 5—Continued

File	Norm[a]	Γ	N_H[b]	I_{Fe}[c]	f[d]	N_{H2}[e]	χ^2_R/F[f]
		1.84					
		1.93					
		1.96					1.07/35.4
f1f2		set			0.49		
		set			0.31		
		set			0.49		
		set			0.31		
		set			0.28		0.92/10.9
vf1f2					0.43/0.54		
					0.29/0.36		
					0.43/0.54		
					0.29/0.36		
					0.25/0.4		0.9/4.2

[a]See table notes, table 3

Table 6. Hours, plref

File	Norm[a]	Γ[b]	N_H[c]	I_{Fe}[d]	$\Omega/4\pi$	χ^2_R/P
S90LW	1.6 ± 0.2	1.9 ± 0.1	0.45 ± 0.19	1.0 ± 0.5	0.5 ± 0.7	0.93
S90MD	3.0 ± 0.2	2.04 ± 0.48	0.52 ± 0.09	1.4 ± 0.3	0.9 ± 0.4	1.03
S90HI	3.6 ± 0.3	2.00 ± 0.07	0.43 ± 0.13	1.2 ± 0.6	0.4 ± 0.5	1.87/24
varpo[e]	1.9 ± 0.1					
	2.9 ± 0.1					
	3.6 ± 0.2					1.29

[a]See table notes, table 3

here tab

6.5 DISCUSSION

Important Questions and answers about variable features in MCG -6-30-15:

1. Is the basic power-law norm variable? The answer is yes for all of the models applied in this thesis. Is the photon index variable? In the partial covering by a warm absorber the answer is probably not, because not only is there more improvement for two absorption columns but also the changes in the photon index are small (< 0.15). For the disk the changes in the power law index are also very small, and variations of Ω are much more probable.

2.Do the superimposed absorption/reflection spectral features vary? They certainly do! For the two absorption column case the variability of the higher absorption column is questionable on very short time scales, but certain on time scales of hours, days and years.

2. In the case of variable partial covering: Can we find any reliable relation between absorption and partial covering fraction? A positive answer may strengthen the case for partial covering vs. warm absorber (see also appendix F).

Chapter 7

DISCUSSION AND CONCLUDING REMARKS

In this chapter we present some concluding remarks on this thesis. In the first section the two component cloud model is considered, and compared with the more 'standard' disk-corona model. In the second section we discuss the dynamics of the central engine and the merits of the shock model. In the last section we discuss the results of our analysis of data from MCG -6-30-15.

7.1 THE CLOUD MODEL

7.1.1 Accretion Disks Versus Clouds

In many cases the two component cloud model is advantageous over the disk-corona model. We argue that, at least in the case of high accretion rates, cloud configuration is more plausible than disk configuration. We first present some theo-

retical arguments, followed by evidence from observations.

The main advantage of an accretion disk is its ability to transfer angular momentum outwards and its axisymmetry. This ability is of less important in the central engine, where the typical densities and magnetic fields are sufficient for the outwards transfer of angular momentum in semi-spherical configurations.

One theoretical reason to consider inhomogeneities, such as clouds, is the fact that the standard thin disks assume that the shear and the resultant angular momentum transfer happens in convection cells of size which is proportional to the height of the disk. In the central engine such assumption means that the cells are comparable in size to the size of the source itself! This picture is more apparent in chapter 4, in which an optically thin disk is perturbed by an inhomogeneity. In this thesis we also note that all of models of variability require inhomogeneities and strong magnetic fields (see chapters 2 and 4).

Significant emission in the UV and EUV parts of the spectrum may be easier to explain with clouds. It was shown that UV emitting accretion disks may be unstable in the central engine. With this result in mind it is hard to explain the UV band, which contains a significant portion of the total emitted radiation, which is supposed to have originated in the central engine. In order to produce so much UV a large

surface has to absorb and re-emit the X-rays and γ-rays from the central engine (see chapters 2, 3 and 4). Very small amount of matter in the form of clouds is needed in order to reprocess the radiation from the central engine. In order to reprocess a significant portion of the emission from the central engine an increased surface area is needed (see chapter 3). If the surface is not large the reprocessing probably results in the same thermal instability which disrupts the disk, especially when a small portion of the disk is illuminated by a flux doubling flare.

Ultimately the alternative geometrical configurations may be distinguished with X-ray telescopes with very high resolution. Present day telescopes, however, cannot achieve this resolution. In the outer regions of AGN the resolution of the NLR and the molecular torus is within reach with optical telescopes of sub-arcsecond resolution. The HST observation of a non-axisymmetric accretion disk in a radio galaxy already shed some light on the configuration. (The observed configuration already posses some problems for the standard accretion disk, because viscous instabilities are expected with varying $\dot{M}$. See, for example, Chakrabarti 1995.) But the resolution is now limited to arc-minutes in the UV to X-ray regime (ROSAT HRI), in which most of the energy is emitted. Improvement of at least two orders of magnitude in resolution without compromising the spectral resolution is thus needed in order to resolve the

geometrical configuration of the central regions. Until such technology is achieved the best way to determine the geometrical configuration is through temporal and spectral analysis of data. The recent campaigns of multi wave-band observations by Tsuruta et al. and others may thus prove to be invaluable in distinguishing between existing models.

One way by which we can distinguish between the disk and cloud models come from the observation of polarization. In thin disks scattering atmospheres should induce a high degree of polarization (Netzer 1990, and references therein). On the other hand, our cloud model predicts very low polarization, because for the size of clouds of our kind the reflection directionality in Equation (3.10) results in weak polarization (Sivron and Tsuruta 1993). Observations favor weak polarization (Netzer 1990). Polarization in the X-ray regime, which can improve our determination of the geometry, may be achieved in the near future.

No sharp Lyman edges (as predicted by many disk models) are expected to be observable with the cloud model, because the strong feature emitted by the clouds is broadened and smeared by e.g. the Doppler shifts with a variety of cloud velocities. This is consistent with observations (Antonucci, Kinney, and Ford 1989, and references therein).

The spectral behavior of the NGC 4051 data near the B-band was examined (Done et al. 1990) which shows no rapid variability during the X-ray flares, and find that the low energy end of the UV bump already appears there. Therefore the lack of rapid variability at this wavelength is consistent with our cloud model. In our model the power-law portion of the IR-optical radiation is due to different mechanisms (Tsuruta 1990), and hence no correlation is predicted between the IR-optical-UV bands and the X-ray band. On the other hand definite correlated variations are predicted among the IR-optical-UV and X-ray bands when a variety of disk models are adopted; for instance, the standard thin-disk model (Shakura and Sunyaev 1973) and a disk with a hot spot (Abramowicz 1990).

In chapter 6 of this thesis we have shown that there is evidence from the Seyfert galaxy MCG -6-30-15 that the 'hard tail' is variable on time scales similar to that of the minimum light crossing. One must determine if the disk can remain stable when such variations are present.

Some evidence for inhomogeneities in the central engine of AGN already exists from X-ray observations (see chapter 6). The variability and spectral variability of the X-ray emission, which accounts for most of the emission from radio quiet AGN, require that the emitting region be unstable. Homogeneous and isotropic (with

respect to the SMBH) accretion, or stable thin disk accretion, cannot be unstable unless perturbations are introduced. The model presented in chapters 2, 3 and 4 of this thesis is natural in that the source of the power law emission which requires some form of magnetic fields is consistent with the fields that confine inhomogeneities. The same fields are also responsible for shocks that can explain spectral variability, the creation of clouds and outward transfer of angular momentum! This outward transfer of angular momentum is not inconsistent with the instability of the disk, because its mechanism is not stationary. The mechanism for accelerating particles (Blandford and Eichler 1987) is naturally explained in the context of clouds and shocks.

It is therefore evident that the transfer of angular momentum property can be explained with clouds rather than disk. For the case of low accretion rates, however, we speculate that the disk-corona model is applicable. The critical accretion rate in AGN with shocks is calculated in Sivron and Tsuruta 1995.

7.1.2 Other Results for the Cloud Model

In deriving the physical properties of the cold clouds component we have shown that the optical depth in the central engine is nearly one when the luminosities are nearly L_{Edd}. It is therefore reasonable to assume that the clouds are indeed optically thick, as long as the number of clouds in the line of sight is relatively small. This was

shown to be a reasonable assumption when we considered shocks as a mechanism for the creation of these clouds (see section 4.2.2).

The radial dependence of cloud parameters found from equations (2.11), (2.13), (2.14) and (2.17) is $T_{cld} \propto R^{-1/2}$, $n_{th} \propto R^{-2}$, $n_{cld} \propto R^{-1}$, and $l_{cld} \propto R^{1/2}$. Since these results change with the dynamics the accuracy is $\pm 1/2$ for the exponents. Note that the density needed for LTE closest to the central object is approximately $n_{th} = 10^{16} cm^{-3}$ for a Bolometric luminosity of $10^{44} erg/sec$ expected in a typical Seyfert I galaxy, whereas the broad line region clouds at $\sim 10^4 R_g$ have a density of $n_{th} \sim 10^{10} cm^{-3}$. From this observational result we also get $n_{th} \propto R^{-2}$. When we include the theoretical results of Celotti, Fabian and Rees 1992 in which the number density of a cloud near the SMBH is approximately $n_{th} = 10^{16-18} cm^{-3}$ for an absorption column of $N_H \leq 10^{21} cm^{-2}$ (for a Seyfert 1 galaxy), we find that $n_{th} \propto R^{-2} - R^{-2.66}$.

In the case that very few clouds exist one expects the outcoming radiation to be partially polarized, because of the effects of the source–cloud–observer angle on this radiation. When X-ray observation of polarization are available the results will probably help determine the geometry of the central engine. (Polarization which is observed from NLR clouds and electron scattering regions that probably reprocess emission from the BLR region in some Seyfert 2 galaxies was used in the determina-

tion of the geometry in the outer regions of Seyferts by Antonucci and Miller 1985). Calculations of the polarization in such a case are relatively straight forward, and should include clouds with $\tau_{1cld} < 1$.

With the same value of f, the major spectral effects of the cloud configuration, as compared with the slab geometry, are (i) the increase of the UV bump, and (ii) the decrease of the reflection features. The difference in the reflected component is due to the part of the reflected component which is absorbed by the clouds between the reflector and the observer. Using the R dependence of the physical variables shown earlier we find that reflection is most effective at intermediate radii. At a representative radius of $R = 30R_g$, with $R_{max} \sim 300R_g$ and black hole mass $M = 10^7 M_\odot$ we get $T_{cld} \simeq 3 \times 10^5$ K and $n_{cld} \simeq 10^{16} cm^{-3}$. For the lower limit on the radial dependence of the clouds size and number density, and for $f \sim 0.9$, we obtain $l_{cld} = 10^{12} cm$ and $n_{cld} = 10^{-39} cm^{-3}$ for NGC 4051. Most of the covered portion of the input spectrum is absorbed by the clouds and reradiated as thermal radiation producing a large UV bump. We calculated the total integrated bolometric luminosity. Using equation (3) it is found that for the most extensively studied rapidly variable Seyferts, NGC 4051 and NGC 6814, the total primary bolometric luminosity L_{bol} is still less than or roughly equal to the Eddington limit. We assumed a large f, e.g. ~ 0.9, and

$M_{bh} \sim 10^6 - -10^7\ M_\odot$, reasonable values. Broadening of the UV bump is evident, with the bump extending from the UV to the soft X-ray excess region.

The generalization of the code which was used in chapter 3 is relatively straight forward. The complete code includes an extended non-thermal source, that is dependent on the distance from the SMBH, and which will therefore be represented by a continuous emission radius dependent function multiplied by the fraction filled by the hot phase. This emission will be added to the macroscopic radiative transfer equation. This code is not applicable in this thesis because the dominant emission mechanism used is bound free emission and absorption which is applicable from $\sim 30R_g$, just outside the region in which most of the non-thermal radiation is probably produced.

The cloud model as presented in chapters 2 and 3 might also be applied to galactic x-ray sources which are black hole candidates, because the underlying physical mechanisms governing these objects are considered to be similar. In the case of the x-ray galactic source Cygnus X - 1 our cloud model agrees better with observations than disk models, because the weaker and symmetrical Fe line feature predicted from our models with $f << 1$ is consistent with the observed data, while the slab reflection models predict this feature to be stronger than and different in shape from the observed Fe line (Done et al. 1991).

In reality the clouds are most likely distributed unisotropically, forming e.g. a quasi-spherical flow or a torus, due to the expected presence of angular momentum. These geometrical effects are currently under investigation (Sivron and Tsurua 1994). Also, because of the plasma and magnetic effects the shape of the clouds is most likely non-spherical, e.g. melon-seed or sheet like, or filamental. We predict that our results presented here are still qualitatively adequate, because random orientation of the clouds will average out most geometrical effects other than the ones considered in this paper. Generalizing the code for such cases is best done by assuming elliptical disks of random and magnetic field modified shapes.

7.2 DYNAMICAL CONSIDERATIONS

Dynamical equations for the two components cloud model may include continuous equations for the optically thin component, and Maxwell-Boltzman type equations for the optically thick component, as is customarily done in galactic mergers (see Barnes and Hernquist 1992). In our case, however, we do not know the shape of the clouds, and their possible preferred direction. It is also hard to argue that the cold component clouds are much smaller than the spacing between such clouds. We therefore solve a simple problem, and point out the method one should employ for a

more dynamically accurate picture.

7.2.1 Results and Conclusions for Shocks

A star orbiting an SMBH can be a curiosity, or a rule — depending on future observations, but shocks are probably present in the central engines of AGN, and they probably modify the emission and should be taken into account in future work.

Natural sizes of perturbations in the outer thin Keplerian disk must be much smaller than R, because the speed of sound in thin disks is much smaller than the Keplerian speed (Frank, King and Raine 1992). The thickness of the thin disk may be a natural size for the perturbations. From equation (2.18) the natural size for the perturbations is l_{cld}, which is similar to the size of a main sequence star in Seyferts.

If shocks are formed the following description is the result of the treatment presented in chapter 4: Considering the velocity of the inhomogeneity found in section 2, and the fact that the post shock matter moves at subsonic velocity, this result determines that the clouds form a 'foamy' wall of thickness $\sim c_s t_s \sim 10^{10}$ cm. A typical filling factor of $C \sim 0.01$ is reasonable for the ratio of ambient and thermal matter under the assumption that half the ambient matter becomes thermal in the post shock region (with the necessary covering factor ~ 1, see Lightman and White 1988, Celotti, Fabian and Rees 1992, Sivron and Tsuruta 1993, Bond and Matsuoka

1994, Goerge and Nandra 1994). Therefore, on the average, one sheet of thickness 10^8 cm can occult the continuum source. Some internal absorption is therefore expected, but there is not yet enough data to determine whether flares or absorption are dominant.

We note that in the case of virial magnetic fields the pressure on the inhomogeneity is similar to that calculated in equation (4.25) and cooling is independent of speed. This results in a 'shooting star effect': When an inhomogeneity plunges into the central engine it slows down while creating tubes, until it reaches lower super Alfvenic speeds and a shock is formed.

We also note that the result of the treatment in section 4.2.5 leads to a prediction on correlation between the slope of the power spectrum and the overall luminosity, because the total number per second of cold inhomogeneities accreted is proportional to $\dot{M} \propto L$. This is shown to be observationally plausible by Green 1993.

The idea of optically thick shock fronts may result in periodic spectral variability in galactic sources, such as the Cataclysmic Variable (CV) in the field of view of NGC 6814, is found to be consistent with observations (Sivron, Tsuruta and Leighly 1994). We note that CVs may be fueled by accretion disks with spiral shocks (Morfill, Spruit and Levy, 1993). We also note that shocks are considered to be the reason for the

spiral structure in the outer disk of M87 (Chakrabarti, 1995).

7.3 RESULTS AND CONCLUSION FROM OBSERVATIONS

The results of chapters 2, 3 and 4 may be related our observational results of chapter 6. Some of our results support the existence of a cold or warm component in or near the central engine of MCG -6-30-15. Some interesting variable features in the spectrum can be explained in this way. Compton reflection from cold matter and emission from hot matter with warm (partially ionized) absorbing matter model can be fit to the data if both the cold and warm absorbers are near the central engine. This scenario is consistent with both the observational reflection and leaky warm absorber and the theoretical disk corona and the two component cloud models. Partial covering of the emission from the hot matter is with very warm matter (in which all elements except Iron are mostly ionized), which is also successful, may be checked by Asca, XTE and AXAF missions. This model is consistent with the two component model, but not the disk model. From the results of chapter 6 it is evident that there is correlation between the low energy absorption feature and the hard x-ray tail, and that they vary together on time scales as short as hours. Some information

on the ionization state of this matter may already be obtained with the above results. See, however, the discussion in appendix F.

In future work the variation of the lower energy part should be checked with the long observations that was performed this summer (1994) by the Asca satellite. The X-ray Time Explorer (XTE) should be invaluable in determining the spectrum in the now unchartered $20 - 100$keV range, which will help establish a clear difference between reflection and absorption models, and will determine which pair model is reasonable for the central engine. Possible observations of polarization with the calorimeter on the Japanese Astro E mission may reveal evidence for a preferable geometrical configuration of the central engines of AGN. (Observations of highly redshifted QSOs by HST may reveal some information on the spectrum in EUV, albeit the observed luminosity may come from anomalously strong AGN with different spectrum.)

Bibliography

[1] Abramowicz, M.A. 1990, Structure and Emission Properties of Accretion Disks, ed. C. Bertout, S. Collin, and J.-P. Lasota (Les Editions Frontieres), 299.

[2] Abramowicz, M.A., Jarosznski, M., and Sikora, M., 1978, A & A, 63, 221.

[3] Antonucci, R.R.J., Kinney, A.L., and Ford, H.C. 1989, ApJ, 342, 64.

[4] Awaki, H., 1991. PhD thesis, Nagoya Univ. Japan.

[5] Awaki, H., Koyama, K., Kunieda, H. and Halpern J.P., 1991, Pub. Astron. Soc. Jpn., 43, 195.

[6] Barnes and Hernquist, 1992, Annual Review of Astronomy and Astrophysics, 30,705.

[7] Begelman, M. ,Sikora and Rees, M.J., 1987, and Rees, M.J., 1987, ApJ,

[8] Bevington, P.R. 1968, Data Reduction and Error Analysis for the Physical Sciences.

[9] Blandford, R.D. , 1990, Active Galactic Nuclei, Saas-Fee Advanced Course 20, Springer-Verlag.

[10] Blandford, R.D., and Eichler, D, 1987, Physics Reports, 154, 1.

[11] Blandford, R.D., Narayan, R., 1993, Annual Review of Astronomy and Astrophysics, 30, 311

[12] Bond, I.A., and Matsuoka, M., 1993, MNRAS, in press.

[13] Caditz, D., Tsuruta, S. and Sivron, R., 1995, in preparation.

[14] Celotti, A., Fabian, A.C., and Rees, M.J. 1992, MNRAS, 255, 419.

[15] Chakrabarti, S.K. and Wiita, P.J., 1992, ApJ, 387, L21.

[16] Chakrabarti, S.K., 1995, ApJ

[17] Devries and Kuipers 1989, Two topics in X-ray astronomy, 1069, eds Hunt, J. & Battrick, B., ESALAB symposium, ESALAB SP-296, ESTEC.

[18] Done, C., Mulchaey, J.S., Mushotzky, R.F., and Arnaud, K.A. 1991, Preprint.

[19] Done and Fabian 1989, MNRAS 240, 81.

[20] Done, C., Ward, M.J., Fabian, A.C., Kunieda, H., Tsuruta, S., Lawrence, A., Smith, M.G., and Wamsteker, W. 1990, MNRAS, 243, 713.

[21] Fabian, A.C. and the Asca PV team, preprint.

[22] Fabian, A.C., Blandford, R.D., Guilbert, P.W., Phinney, E.S., and Cueller, L. 1986, MNRAS, 221, 931.

[23] Fabian and Brancos 1992, Annual Review of Astronomy and Astrophysics, 30, 429 .

[24] Ferland, G.J. and Rees, M.J., 1988, ApJ, 332, 141.

[25] Fiore, F., Perola, G.C., Matsuoka, M., Yamauchi, M. and Piro, L. 1992, Astron. Atrophys. 262, 37.

[26] Ford, H.C., Tsvetanov, Z.I., Kriss, G.A., Harmes, R., Dressel, L., 1994, BAAS 184, meeting abstracts, 64.02.

[27] Ford, H.C. et al., 1994, ApJ, 435, L27.

[28] Frank, J., King, A.R. and Raine, D.J., *Accretion Power in Astrophysics* (Cambridge: Cambridge University Press, second edition 1992).

[29] Fraser, 1988, X-ray detectors in astronomy, Cambridge University Press.

[30] George, I.M., and Fabian, A.C. 1991, MNRAS, 249, 352.

[31] George I.M., and Nandra K. 1994, preprint.

[32] George, I.M., Turner, T.J. and Netzer, H. 1995, preprint.

[33] Ghiselinni, and Haardt, 1994, ApJ.

[34] Grandi, P., Tagliaferri, G., Giommi, P., Barr, P., Paslumbo, G. 1992, ApJSuppl. 82, 93.

[35] Grandi, Done and Urry, 1994, ApJ, 428, 599.

[36] Green, A. 1993, PhD thesis, University of Southampton, U.K.

[37] Guilbert, P.W., Fabian, A.C. and Rees, M.J., 1983, MNRAS205,593.

[38] Guilbert, P.W., & Rees, M.J. 1988, MNRAS, 233, 475

[39] Hasinger, Trumper, J. and Schmidt 1991, ROSAT bgd.

[40] Hayashida, K. 1989, Pub. Astr. Soc. Jpn., 41, 373.

[41] Inoue, 1994, private communication.

[42] Iwamoto, N., 1989, Phys. Rev. A., 39, 8 , 4076.

[43] Iwasawa, K. et al. 1993, ApJ

[44] King, A.R., & Done, C. 1994, preprint.

[45] Kunieda, H., Turner, T.J., Awaki, H., Koyama, K.,Mushotzky, R.F., and Tsusaka, Y. 1990, Nature, 345, 786.

[46] Kunieda, H., Turner, T.J., Awaki, H., Koyama, K., Mushotzky, R.F. and Tsusaka, Y. 1990, Nature 345, 786.

[47] Kunieda, H., Hayakawa, S., Tawara, Y., Koyama, K., Tsuruta, S. and Leighly, K.M., 1992, ApJ384, 482.

[48] Kusunose and Takahara 1988, PASJ, 40, 435.

[49] Landau & Lifshitz, 1987, 2nd edition, Pergamon press.

[50] Levinson, A., 1994, ApJ,

[51] Lightman, A.P., 1982, ApJ253, 842.

[52] Lightman, A.P. and Eardley, D.M., 1974, ApJ, 187, L1.

[53] Lightman, A.P. and White, T. 1988, ApJ, 335, 57.

[54] Lightman, A.P. and Zdziarski, A.A. 1987, ApJ, 319, 643.

[55] Lynden-Bell 1969, Nature, 223, 690.

[56] Makino, F. 1987, Ap. Letters Comm., 25, 223.

[57] Matsuoka, M., Piro, L., Yamauchi, M. and Murakami, T. 1990, ApJ, 361, 440.

[58] Matsuoka, M. et al. 1994, preprint.

[59] Mazur 1982, J. Phys.A, 15, 3173.

[60] McHardy 1988, Mem S.A. It, 59, 239.

[61] Misner, C.W., Thorne, K.S. and Wheeler, J.A. 1972, W.H.Friedman and company.

[62] Morfill, G., Spruit, H. and Levy, E.H., in Protostars and Planets III, University of Arizona Press.

[63] Mushotzky, R., Done, C. and Pounds, K., 1993, Annual Review of Astronomy and Astrophysics, 30, 717.

[64] Nandra, K. 1992, ROSAT background.

[65] Nandra, K. and Pounds, K.A. 1990, Nature, 359, 215.

[66] Nandra, K., Pounds, K.A. and Stewart, G.C. 1990, MNRAS242, 660.

[67] Nandra, K., Pounds, K.A. and Stewart, G.C., Fabian, A.C. and Rees, M.J. 1989, MNRAS236, 39p.

[68] Nandra, K., Pounds, K. A., Stewart, G.C., George, I.M., Hayashida, K., Makino., F., and Ohashi, T. 1991, MNRAS, 248, 760.

[69] Netzer H. 1990, *Structure and Emission Properties of Accretion Disks*, ed. C. Bertout, S. Collin, and J.-P. Lasota (Les Editions Frontiers), 177.

[70] Netzer, H., Turner, T.J. and George, I.M. 1994, ApJ435, 106.

[71] Netzer, H., 1990, Active Galactic Nuclei, Saas-Fee Advanced Course 20, Springer-Verlag.

[72] Papaloizou and Pringle 1984, MNRAS, 208, 721.

[73] Pei, Y.C., Tsvetanov, Z.I., Ford, H.C., Kriss, G.A.,Ferrarese, L., 1994, BAAS 184, meeting abstracts, 64.03.

[74] Phinney, E.H., 1983 PhD thesis, Cambridge, UK.

[75] Pineault, S. and Landry, S., 1994, MNRAS, 267, 557.

[76] Pounds, K.A., Nandra, K., Stewart, G.C., George, I.M., and Fabian, A.C. 1990, Nature, 344, 132.

[77] Pounds, K.A., Turner, T.J. and Warwick, R.S. 1986, MNRAS, 221, 7p.

[78] Pounds, K.A. et al. 1993, preprint.

[79] Priest, E.R., Hood, A.W. and Anzer U., 1989, ApJ, 344, 1010.

[80] Rauch, K.P. & Blandford, R.D., 1993, preprint

[81] Rees, M.J. 1984, Annual Review of Astronomy and Astrophys., 22, 471.

[82] Rees, M.J. 1987, MNRAS, 228, 47P.

[83] Rees, M.J. 1990, Science.

[84] Rees, M.J., Begelman, M.C., Blandford, R.D. and Phinney, E.S., 1982, Nature, 295, 7.

[85] Rees, M.J., Netzer H. and Ferland, G.J., 1989, ApJ, 347, 460.

[86] Reichert, G.A., Mushotzky, R.F., Petre, R. and Holt S.S. 1985, ApJ296, 69.

[87] Reynolds, C.S. and Fabian A.C. 1995, MNRAS, in press.

[88] Robinson 1975, Phys Rev Lett, 34, 905.

[89] Savonije, G.J., Papaloizou, J.C.B. and Lin, D.N.C., 1994, MNRAS268,13.

[90] Salpeter E.E., 1964, ApJ140, 796.

[91] Shapiro, S.L., Lightman, A.P., & Eardley, D.M., 1976, ApJ,203,187 (SLE76).

[92] Sivron, R. and Tsuruta, S. 1993, ApJ,402, 420.

[93] Sivron, R. and Tsuruta, S. 1995, in preparation.

[94] Sivron, R., Kunieda, H., Tsusaka, Y. and Tsuruta, S. 1995, in preparation.

[95] Sivron,R., Tsuruta, S. and Caditz D., 1994, submitted.

[96] Svennson, 1987, MNRAS258, 321.

[97] Sunyaev and Titarchuk 1980, Astronomy and Astrophysics, 86, 121.

[98] Syer, D., Clarke, C.J. & Rees, M.J., 1990, MNRAS,250 ,505 (SCR90).

[99] Televich, R., Tenorio-Tagle, G., Franco, J. and Melnick, J., 1992, MNRAS255, 713.

[100] Thorne, K.S. and Price, R., 1975, ApJ195, L101.

[101] Tritz, B., & Tsuruta, S., 1989, ApJ, 340, 203.

[102] Trumper, J., 1990, Phys.Bull. 46, 137.

[103] Tsuruta, S. 1990, *Structure and Emission Properties of Accretion Disks*, ed. C. Bertout, S. Collin, and J.-P. Lasota (Les Editions Frontiers), 289.

[104] Tsuruta, S. 1992, *The Frontiers of X-ray Astronomy*, ed. K. Koyama and Y. Tanaka (The Univ. Acad. Press, Inc.).

[105] Vio, R., Cristiani, S., Lessi, O. and Salvadory, L., 1991, ApJ, 380, 351.

[106] Turner M. et al. 1989, Pub. Astro. Soc. Japan, 41, 345.

[107] Walter, R. and Fink 1993, Astron. and Astrophys., preprint.

[108] White, T. & Lightman, A., 1990, ApJ, (WL90).

[109] Wilson et al.

[110] Walter and Fink, 1993, Astronomy an Astrophysics.

[111] Zdziarski, A.A., Ghisellini, G., George, I.M., Svensson, R., Fabian, A.C., and Done, C. 1990, ApJ 363,L1.

APPENDICES

Appendix A

Reasons for Super Massive Black Holes

AGN are not only among the most luminous objects in nature, but also among the most efficient accelerators of matter and among the most dynamically stable astrophysical objects. For example, some AGN emit jets of matter that are so energetic and highly collimated that they extend to a distance eleven orders of magnitude larger than the central engine and keep their directionality throughout. Radio emitting lobes, that are almost certainly the result of the interaction of the jets with inter galactic material, are found either at one side, or the two opposite sides of the host galaxy. Theses lobes may be as far as 10 billion light years away from the nucleus of the host galaxy. The energy contained in those lobes exceeds the total output which can be produced by the central engine over a period of 10 billion years. The

existence of these features therefore implies that the jet emitting mechanism keeps its directionality for at least 10 billion years.

The release of gravitational energy may also be possible by the extraction of energy directly from the ergosphere of a rotating Kerr SMBH. In the ergosphere particles cannot remain at one point because of the gravitational pull of the rotating black hole. Particles which manage to escape this region gain energy, which reduces the rotational energy of the black hole This process is called the Penrose process. In a variation on this process an electromagnetical torque is applied on the rotating black holes ergosphere (Blandford 1990). The result of such processes may be the outstream of energy in jets and winds.

Appendix B

Radio Loud AGN

Thermal particles in the ambient gas can be accelerated to high velocities by shock-Fermi processes (Blandford and Eichler 1987) in the shock front. The distribution of Lorentz factors for these particles is of the form $f(\gamma_L) \propto \gamma_L^{-(2+r)/(r-1)}$ for non-relativistic shocks, where $r \sim V_u/V_d$, the shock compression, is of order 4, and V_u and V_d are the upstream and downstream (post-shock) velocities. (Relativistic shocks steepen the exponent even more.) Particles in the central engine are therefore efficiently accelerated across the shock (reference from 1995.....).

The bremsstrahlung timescale for cooling with no magnetic fields at all is therefore too large to account for post-shock matter cooling. But note that some magnetic fields must exist in the central engine, because the accretion disk is not dense enough to allow for the diffusion of the ambient stellar magnetic fields away from the accreting

matter.

Magnetic fields change the problem by modifying both the post-shock radiation and the thickness of shocks. Considering strong hydro-magnetic shocks The radiative cooling is always shorter for the compactness parameters obtained from table 1. The compactness in that region is increased by an order of magnitude, and the timescales for pair-creation are very short. Matter is probably cooled in the post-shock region down to LTE temperatures. In the rarefaction region behind the shock this 'cold' matter is probably sheared into clouds by strong turbulence, and may even be magnetically confined. We note that collisionless shocks are much narrower, and therefore the time which the post-shock matter spends in the compressed region is much shorter. The cooling timescale for synchrotron radiation, $t_{cool} \propto B^{-3/2}$, may be decreased by an order of magnitude because of an order of magnitude increase in the post-shock magnetic fields. (such increase is possible in strong shocks. See, for example, Eilek and Hughes 1992). The synchrotron radiation alone is probably not enough to account for the radiation. Compton cooling should be much faster than synchrotron. The mean free path for collisions is reduced because of the increased post shock densities and synchrotron radiation density U_s. Typical Compton-cooling timescales, $t_C \propto 1/(nU_s)$, are therefore reduced by up to two orders of magnitude.

The free-free cooling in the post-shock matter is also increased by up to two orders of magnitudes (see equation (2....)). The size of the post-shock matter should therefore be at least $10^{-2}R_X$ in order that the shock emission be similar to the total source emission. The timescale t_h for heating up the post-shock matter was derived in section 4.1.3. The size of the post-shock matter region

$$R_{ps} \sim v_* t_h \tag{B.1}$$

is therefore bounded by $t_s > t_h > t_C$. It is apparent that there is a still a discrepancy here. The shock itself is the source of the power-law high energy particles. This only reduces the timescale by one exponential power. We therefore invoke a scenario in which the increased radiation results in the collapse of the hot post-shock matter into cool LTE matter, as in chapter 2.

Appendix C

The Eddington Approximation for an Opaque Slab

We use the two stream Eddington approximation, as is hinted in LW88, and follow the method outlined in Rybiky and Lightman 1979.

Assume the picture presented in figure 2..... the radiative transfer equation in the case of an optically thick slab is solved in the two regions: $s < 0$ in which the source function and absorption are zero, and $s > 0$ in which the source function may be written as $S_\nu = B_\nu + \alpha_\nu I_\nu$. Changing variables $ds = d\tau/(\mu(a_\nu + \sigma_\nu))$, where $\mu = \cos\theta$ is cosine the angle between the incoming radiation and the plane at $s = 0$, and s_ν is the cross section, and integrating over $-1 < \mu < 1$ the radiative transfer equation becomes:

$$\frac{1}{\alpha_\nu + \sigma_\nu}\frac{dH_\nu}{dz} = J_\nu - S_\nu, \tag{C.1}$$

where $J_\nu = (1/2)\int I_\nu d\mu$, $H_\nu = (1/2)\int \mu I_\nu d\mu$ and the radiation pressure is $K_\nu = (1/3)J_\nu = (1/2)\int \mu^2 I_\nu d\mu$. Manipulating those equations one can easily get a second order equation for J_ν:

$$\frac{1}{3(\alpha_\nu + \sigma_\nu)}\frac{d^2 J_\nu}{dz^2} = J_\nu - S_\nu \tag{C.2}$$

In a random walk process an average single scattering albedo is $1 - \epsilon_\nu = \sigma_\nu/(\alpha_\nu + s_\nu)$, and we get:

$$\frac{d^2 J}{d\tau^2} = 3\epsilon(J - B). \tag{C.3}$$

The general solution of the above equation is $J = C_1 e^{\sqrt{3\epsilon}\tau} + C_2 e^{-\sqrt{3\epsilon}\tau} + B$. Boundary conditions must be provided now.

The Eddington two-stream approximation follows: the equation can now be solved by assuming that the entire radiation fields can be represented by radiation traveling in two angles, and may be written as $I_\nu = I_\nu^+ \delta(\mu - 1/\sqrt{3}) + I_\nu^- \delta(\mu + 1/\sqrt{3})$. The mean intensity, flux and radiation pressure are then $J = I^+ + I^-$, $H = 1/(2\sqrt{3})(I^+ + I^-)$ and $K = (1/6)(I^+ + I^-) = (1/3)J$. The Eddington two-stream assumption is justifyable if there is small dependence on the angle for small angles.

Using the relations between J, H and K we find

$$I^+ = J + \frac{1}{\sqrt{3}}\frac{\partial J}{\partial tau}, \tag{C.4}$$

and

$$I^- = J - \frac{1}{\sqrt{3}} \frac{\partial J}{\partial tau}. \tag{C.5}$$

The boundary conditions can now be used: $I^-(\tau = 0) = S_{in}$ and, with the fact that the mean intensity cannot explode at ∞ but $\tau >> 1$ for an optically thick slab, the first term in the general solution vanishes. We thus find $C_2 = e^{-\sqrt{3\epsilon}\tau}(S_{in} - B)/(1+\sqrt{\epsilon})$, and

$$J - B = \frac{S_{in} - B}{1 + \sqrt{\epsilon}} e^{-\sqrt{\epsilon}\tau}, \tag{C.6}$$

and plugging into equation (C.4) (for I^+) we get

$$I^+ = 2B \frac{2 + \sqrt{\epsilon}}{1 + \sqrt{\epsilon}} + S_{in} \frac{1 - \sqrt{\epsilon}}{1 + \sqrt{\epsilon}}. \tag{C.7}$$

The first term which includes the thermal emission can be treated separately, as in equation (3.11) in chapter 3, when the full geometry of the cloud is given, and we are thus left with the result given in the paragraph following equation (3.10).

Appendix D

The Case of Dense Clouds Inside a Disk

In figure 3-8 we see a configuration which includes both the disk structure, which may come about due to the the disruption of a thin disk due to thermal instabilities (see chapters §1 and §4). This exercise is done in order to see how the opening angle affects the outcoming spectrum.

The angle between the observer, the reflecting cloud and the point source is found from the product of the cloud location vector $(r\sin\theta\cos\phi, r\sin\theta\sin\phi, r\cos\theta)$ and the direction of the observer $(\sin\beta, 0, \cos\beta)$. This is one of the modifications needed in the code.

Appendix E

The Method of Moon Phases

The fraction of the incident luminosity which is reflected is assumed to be the fraction of the area which is observed in this case. In figure 2-..., using $l = \sqrt{x^2 + y^2 + z^2}$, and the $\tan\theta = z/y$ we find that the terminator's equation is $y = \sqrt{(l^2 - x^2)/(1 + \tan^2\theta)} = \cos\theta\sqrt{(l^2 - x^2)}$, and the total observed area in the x, y plane is thus

$$A = 1 + 2\int_{x=0}^{l}\int_{y=0}^{\cos\theta(l^2-x^2)} dy\, dx = \frac{1}{2}\pi l^2(1 + \cos\theta). \tag{E.1}$$

Another approximation of the reflection uses the total reflected area, rather than the cross section:

$$A = \int_{\phi=0}^{\pi}\int_{\theta'=0}^{\pi-\theta} l^2 \sin\theta' d\theta' d\phi = \pi l^2(\cos\theta + 1). \tag{E.2}$$

The fraction of the maximum observable area is the same, but this result can be easily generalized to the case of ellipsoids which can roughly represent any three dimensional

body by varying the three semiaxes.

Appendix F

The Treatment of a 'Warm Absorber'

By requiring that radiative equilibrium is reached in ionized matter we get from the rate equation:

$$N_{r+1} n_e(p) \left[A_{r+1,r} + u(\nu_{r,r+1}) B_{r+1,r}\right] = N_r u(\nu_{r,r+1}) B_{r,r+1} \tag{F.1}$$

the Saha equation for $N_{r+1} n_e(P)/N_r$.

In our work we consider a simplified situation, in which the only two states involved are the completely ionized atom, and an atom with one electron, which is in the ground state as is proven in common texts (see Rybiki and Lightman). In such a case the induced and absorption Einstein coefficients are related through $B_{r,r+1}/B_{r+1,r} = g_{r+1} g_e 4\pi p^2/g_r$. The induced and spontaneous coefficients are related through the quantum mechanical relation (?) $A_{r+1,r} = 2h\nu^3 B_{r+1,r}/c^2$.

We next consider the radiation energy density $u(\nu_{r,r+1}) = I_\nu/c$ where $I_\nu = L_\nu/(R^2)$ is the specific intensity of an isotropically emitting source at a distance R. Assuming the material is illuminated by a power-law source which dominates the thermal emission (at least as far as the ionized species are concerned) we get

$$L = \int_{\nu_{min}}^{\nu_{max}} A\nu^{-\gamma} d\nu \tag{F.2}$$

which makes it able to explicitly calculate $A = L/(\nu_{max}^{1-\gamma} - \nu_{min}^{1-\gamma})$. Since the distance from the central source is hard to determine it is appropriate to switch to another variable, the ionization parameter $\Xi = L/(4\pi R^2 n_e c h \nu_{r,r+1})$. The radiation energy density is thus, for example, $u = \Xi n_e h/Q = \Xi D$ for $\gamma = 1$, where $Q = \ln(\nu_{max}/\nu_{min})$.

Plugging into the saha equation one gets

$$\frac{N_{r+1} n_e}{N_r} = \frac{g_{r+1} g_e}{g_r} \frac{(2\pi m_e kT)^{3/2} e^{p^2/2mkT}}{1 + 2\nu^3 Q/(c^2 \Xi n_e)}. \tag{F.3}$$

In table .... we notice that the equivalent 'cold' hydrogen absorption column in the ~ 0.8keV range is $10 - 100$ times smaller than that in the $7 - 9$keV region. We use equation (6.7) above for both of these regions, and take the ratio:

$$\frac{N_{r+1}(O)/N_r(O)}{N_{r+1}(Fe)/N_r(Fe)} \sim \frac{1 + W\chi_I^3(Fe)/\Xi}{1 + W\chi_I^3(O)/\Xi}. \tag{F.4}$$

Note that the above example is a very special case, which should be recalculated when competing cooling processes are present.

Previous authors have used software such as 'CLOUDY' (Ferland and Rees 1988 and references therein) for the case of MCG -6-30-15, and found absorption column of order $\sim 10^{22}\mathrm{cm}^{-2}$ for the warm absorber and ionization parameter of order $\Xi \sim 40$ (see Nandra 1989, Fabian et.al. 1994). CLOUDY, which was extensively utilized for the BLR, may not be reliable for processes which occur very close to the central engine. In particular the above program definitely uses the density of the BLR implicitly when calculating the ionization parameter. Higher densities will result in different cooling and heating mechanisms. Overfitting of emission/absorption features which are not efficiently detected by Ginga may also be a problem with such programs, as they tend to distort the spectral features which are actually observed. Software under development for the region (Netzer 1993) may be utilized for our subsequent work.